

DIGITAL ELECTROMAGNETIC CALORIMETERS FOR FUTURE COLLIDER APPLICATIONS

R. R. Bosley

*Thesis submitted for the degree of
Doctor of Philosophy*



Particle Physics Group,
School of Physics and Astronomy,
University of Birmingham.

October 27, 2022

University of Birmingham Research Archive e-theses repository



This unpublished thesis/dissertation is under a Creative Commons Attribution 4.0 International (CC BY 4.0) licence.

You are free to:

Share — copy and redistribute the material in any medium or format

Adapt — remix, transform, and build upon the material for any purpose, even commercially.

The licensor cannot revoke these freedoms as long as you follow the license terms.

Under the following terms:



Attribution — You must give appropriate credit, provide a link to the license, and indicate if changes were made. You may do so in any reasonable manner, but not in any way that suggests the licensor endorses you or your use.

No additional restrictions — You may not apply legal terms or technological measures that legally restrict others from doing anything the license permits.

Notices:

You do not have to comply with the license for elements of the material in the public domain or where your use is permitted by an applicable exception or limitation.

No warranties are given. The license may not give you all of the permissions necessary for your intended use. For example, other rights such as publicity, privacy, or moral rights may limit how you use the material.

Unless otherwise stated, any material in this thesis/dissertation that is cited to a third-party source is not included in the terms of this licence. Please refer to the original source(s) for licencing conditions of any quotes, images or other material cited to a third party.

ABSTRACT

The LHC will run until ~ 2040 , after which time a new generation of particle colliders is anticipated. To measure the properties of known interactions at the LHC with greater precision, and to probe physics beyond the Standard Model, it is expected that a lepton collider will be constructed. This thesis focuses on the application of digital CMOS MAPS sensors to electromagnetic calorimetry at future colliders.

Simulations of various geometrical configurations of a digital ECAL in the FCC-hh environment, a proposed 100TeV circular proton-proton collider, are presented. The optimal configuration using 50 silicon layers sandwiched between $0.6X_0$ thick layers of lead is found to provide an energy resolution of $\frac{\sigma_E}{\mu_E} = \left(\frac{15.46 \pm 0.12\%}{\sqrt{E}}\right) \oplus (0.917 \pm 0.009\%)$. While this is a slightly poorer standalone resolution than the liquid argon baseline ECAL, this detector technology enables improved combination with information from the inner tracker due to its higher granularity, which may be required to mitigate the high pile-up regime in FCC-hh.

Beam tests of a digital ECAL prototype with 48 ALPIDE sensors (EPICAL-2) are analysed. An event selection algorithm for EPICAL-2 is presented and its merits and performance are evaluated. The response of EPICAL-2 is analysed, and the intrinsic resolution from electron beam tests in the range 1–5 GeV found to be $\frac{\sigma}{\mu} = \left(\frac{18.7\%}{\sqrt{E}}\right) \oplus (2.4\%)$ when a simple clustering algorithm is applied. The performance is also modelled in Allpix² simulations, and the resolution from simulations found to be $\frac{\sigma}{\mu} = \left(\frac{14.0\%}{\sqrt{E}}\right) \oplus (2.6\%)$. This is comparable to the CALICE analogue ECAL prototype and a significant improvement upon the resolution of the previous EPICAL-1 prototype. The lateral profiles of EPICAL-2 are presented and the maximum hit density for a 5 GeV electron beam is found to be ≈ 300 hits/mm². Lastly, the forward-backward asymmetry of EPICAL-2 is examined and its causes identified using simulations.

DECLARATION OF AUTHOR'S CONTRIBUTION

The work presented herein was carried out within several collaborations, including CALICE, FCC-hh and ALICE FoCal, however all the work presented herein is solely the author's work unless otherwise stated.

The simulation studies in Chapter 5 were performed using the FCCSW0.9 simulation framework. The geometry implementation therein was generated by the author, and was based on the design of the ECAL for ILD. Event generation was performed by the author. Results from these studies have been presented in the FCC Conceptual Design Report and at presentations for CALICE.

The author attended and was heavily involved in the November 2019 and February 2020 data-taking using the EPICAL-2 prototype discussed in Chapter 6. The analysis software for EPICAL-2 was developed by the EPICAL-2 working group, including large contributions by the author. The author developed of the event display in Section 6.4.1 utilising the CED software package developed for ILC. The Multi-Cut event selection was developed by the author using a framework developed by N. van der Kolk and A. van Bochove. The studies comparing the two EPICAL-2 event selection algorithms were performed by the author. The calibration studies in Section 6.5, including development of the pixel masking, chip corrections and alignment, were all undertaken by members of the EPICAL-2 working group. The linearity, resolution and longitudinal profile studies in Section 6.7.1, Section 6.7.2 and Section 6.7.3 were performed by several members of the EPICAL-2 collaboration including the author. The lateral profile and forward-backward asymmetry studies in Section 6.8 and Section 6.9 were performed exclusively by the author. The simulation studies of EPICAL-2 used the Allpix² package, with an EPICAL-2-specific software package which was developed largely by T. Rogoschinski with some small contributions by the author. Generation of 24-layer events was performed by T. Rogoschinski, and analysis of the results of these simulations herein was performed by the author unless otherwise stated. Generation of the single-layer events in Section 6.9 was performed by the author.

ACKNOWLEDGEMENTS

Doing a PhD was something of a personal aspiration for me, from quite a young age. From the early school kid's dreams I had about becoming a famous scientist, renowned throughout the world for centuries to come, through my career as an undergraduate, a single ambition materialised: If I can finish a PhD, then I'll have contributed, in however small a way, to the vast network of knowledge and experience which we call "science." Whatever journey I embark on afterwards, I will have left that mark on the world, that small gift to all those inquisitive minds that come after me. It will have been a life worth living, and a legacy worth leaving. I cannot understate how grateful I am to everybody around me for the support they have shown me, in whatever form it came and however small it was.

There is not enough paper in the world with which to praise my supervisor, Prof. Nigel Watson. His superhuman ability to burn the candle at more ends than it should rightly have, his apparently endless patience, his compassion and his incredible wisdom have been invaluable. I am incredibly grateful for his taking me on in a field with which I had little experience, and uncomplainingly seeing me through all the bumps along the road. Thanks also go to Dr. Tony Price, my secondary supervisor, for his kind words of advice during my first year, and for keeping his cool when we discovered a huge mistake we'd made 24 hours before a conference talk. Lastly, I should thank Dr. Alasdair Winter for his assistance in showing me the ropes when I first started, even though he was under absolutely no obligation to do so and had his own thesis to be worrying about.

I'd also like to thank all the members of CALICE and the EPICAL collaboration for all the time and energy they have put into my work, and the insightful feedback they have often given me. Particular thanks go to Tim Rogoschinski, Fabian Pliquett, Hiroki Yokoyama, Qasim Malik, Thomas Peitzmann and Naomi van der Kolk, who have been vital collaborators in the EPICAL test beam work.

Doing this PhD has at times been a significant challenge to my mental health, and I would have ground to a quivering halt without the amazing support network which I have found surrounding me. First and foremost I want to thank my incredible partner Amelia, who has always made time to listen to my complaining and who has stuck by me, with love and understanding, through some of the hardest times in both our lives. Huge thanks go to Mum and Dad, whose support, advice and love has helped me stay proud of my work, for which I will be eternally grateful. I'd also like to thank my brother Freddie, whose supernatural ability to drop me a call whenever it's most helpful has been a lift on particularly difficult days. Thanks also to Granny, Granddad, Uncle Ben, Auntie Claire and Cousin Zandra for all their support over the years.

A special mention goes to Jeff Wilday, who was my psychological practitioner for a few months in 2021 and who gave me the tools I needed to re-frame feelings of worthlessness and impostor syndrome at a time when I desperately needed them.

I'd like to thank Alasdair (again), Jamés, Andy, Tim, Dan B., James, Gov, Nandish, Dan L., Jon, John, Patrick K. and Patrick F. for welcoming a complete stranger into the PhD contingent of the department. Alongside them go non-department folks whose friendship has likewise been a great experience: Alison, Tammy, Manny, Rose, Ollie, Jacob and Dave. From Dilshad to dice games, it's been a heck of a time and I expect many more such adventures to come.

"I'll bet you a Ph.D. you won't make that shot"

A. Winter, shortly before I made the shot.

Contents

1	INTRODUCTION	1
1.1	The Standard Model	1
1.2	Beyond the LHC	7
1.2.1	Energy Frontier	8
1.2.2	Precision Frontier	9
1.2.3	Circular vs. Linear Colliders	10
1.2.4	Beamstrahlung	12
2	PHYSICS AT FUTURE COLLIDERS	14
2.1	The ILC and the CLIC	14
2.1.1	Introduction to the ILC	14
2.1.2	Introduction to the CLIC	16
2.1.3	Physics at ILC 250 GeV	17
2.1.4	Physics at ILC/CLIC 380–500 GeV	19
2.1.5	Physics at ILC 1 TeV	21
2.1.6	Physics at CLIC 1.5/3 TeV	22
2.2	FCC	23
2.2.1	Introduction to the FCC	23
2.2.2	Physics at FCC-ee and FCC-eh	24
2.2.3	Physics at FCC-hh	26
3	PARTICLE DETECTOR METHODS FOR FUTURE COLLIDERS	28
3.1	Particle Detectors	28
3.1.1	Inner Tracking Devices	30
3.1.2	Muon Trackers	31
3.1.3	HCALs	31
3.1.4	ECALs	31
3.2	Electromagnetic Calorimetry	32
3.2.1	Electromagnetic Interactions	32
3.2.2	Homogeneous Calorimeters	34
3.2.3	Sampling Calorimeters	35
3.2.4	Energy Resolution	36
3.3	Particle Flow Calorimetry	38
3.4	Analogue ECALs for Particle Flow	39
3.5	Digital Calorimetry Concept	39
3.6	The Case for Digital Calorimetry	40
3.7	Signal Generation in Silicon Sensors	41

3.8	CMOS MAPS Technology for DECAL Applications	43
4	PARTICLE DETECTORS FOR FUTURE COLLIDERS	45
4.1	SiD and ILD	45
4.1.1	SiD Overall Design	46
4.1.2	ILD Overall Design	47
4.1.3	SiD/ILD ECAL Design and Performance	48
4.2	CLICdet	50
4.2.1	CLICdet Overall Design	50
4.2.2	CLICdet ECAL Performance	52
4.3	FCC-hh Detection	52
4.3.1	The FCC-hh ECAL	53
5	SIMULATIONS OF FULL-SCALE DECALS IN FCC-HH	55
5.1	Introduction	55
5.2	Event Generation and Detector Simulation	56
5.3	Analogue and Digital Performance	60
5.3.1	Energy Reconstruction	60
5.3.2	Energy Resolution	61
5.4	Passive Layer Geometry Variation	63
5.5	Future Developments	66
5.6	Conclusions	67
6	EPICAL2 TEST BEAM STUDIES	70
6.1	Introduction	70
6.1.1	EPICAL1 MIMOSA Prototype	70
6.1.2	ALPIDE Digital Sensors	73
6.1.3	EPICAL2 ALPIDE Prototype	75
6.2	Simulations	78
6.2.1	Allpix Squared	78
6.2.2	Event Generation and Prototype Simulation	80
6.3	Data Samples	83
6.3.1	DESY Test Beam	84
6.3.2	November 2019 DESY Data-Taking	85
6.3.3	February 2020 DESY Data-Taking	87
6.4	Data Quality Assurance	94
6.4.1	C Event Display	95
6.4.2	Systematic Low-Event Region	96
6.5	Calibration	101
6.5.1	Pixel Masking	101
6.5.2	Chip Corrections	102
6.5.3	Alignment	103
6.6	Event Selection	105
6.6.1	Clustering Algorithm	105
6.6.2	Multi-Cut Event Selection	106
6.6.3	Jet-Based Event Selection	108

6.6.4	Performance of Event Selection Algorithms	110
6.7	EPICAL2 Overall Performance	113
6.7.1	Linearity	113
6.7.2	Resolution	116
6.7.3	Longitudinal Profile	120
6.8	Lateral Profile	122
6.8.1	Determination of Shower Axis	122
6.8.1.1	Perpendicular	122
6.8.1.2	Perpendicular With Search	123
6.8.1.3	2-D Fit of Means	124
6.8.1.4	3-D Fit of Means	124
6.8.1.5	3-D Fit of Pixels	125
6.8.1.6	Evaluation of Axis-Finding Methods	125
6.8.2	Determination of Annulus Area	128
6.8.3	Lateral Profile Results	131
6.9	Forward-Backward Asymmetry	133
6.9.1	Motivation	133
6.9.2	Asymmetry in Data and Simulations	133
6.9.3	Diagnosing Asymmetry using Simulations	136
6.10	Conclusions	140
7	CONCLUSION	143

List of Tables

1.1	Particles of the Standard Model	3
1.2	Symmetry-Conservation Examples	4
2.1	Physics Processes at ILC	16
2.2	Beam Parameters	17
4.1	CLICdet Photon Energy Resolution	52
5.1	FCC-hh DECAL Passive Layer Configurations	64
5.2	FCC ECAL Energy Resolution Fit Parameterisation	65
5.3	FCC DECAL Energy Resolution Values	68
6.1	Events using Typical Settings, November 2019	86
6.2	Events using Alternate Settings, November 2019	88
6.3	Events using Typical Settings, February 2020	91
6.4	Events Recorded: Varying Temperature, February 2020	91
6.5	Events recorded: Varying Position, February 2020	92
6.6	Events recorded: Varying Angles, February 2020	93
6.7	Events using Positron Beam, February 2020	93
6.8	Event Selection Efficiency, Full Range	112
6.9	Event Selection Efficiency, Restricted Range	112
6.10	Effective Momentum	116
6.11	Resolution Summary	118
6.12	Shower Maxima	121
6.13	Single-Layer NHits Means	138

List of Figures

2.1	International Linear Collider (ILC) Schematic	15
2.2	Compact Linear Collider (CLIC) accelerator Schematic	17
2.3	Higgs Feynman Diagrams	18
2.4	$t\bar{t}$ Production Mechanisms	19
2.5	Higgs Feynman Diagrams	20
2.6	Double Higgs Production Mechanisms	21
2.7	CLIC Terascale	22
2.8	FCC Accelerator Schematic	23
2.9	FCC location	25
3.1	Generic Detector Schematic	29
3.2	P-N Junction	42
3.3	CMOS schematic	44
4.1	SiD Diagram	46
4.2	ILD Diagram	48
4.3	ILD ECAL	49
4.4	CLICdet Diagram	51
4.5	FCC LAr ECAL Layout	53
5.1	FCC DECAL Hitmaps	57
5.2	FCC DECAL (3-D)	58
5.3	FCC NHits Distribution DECAL/AECAL	59
5.4	FCC Simulated Layer Structure	59
5.5	FCC DECAL/AECAL Linearity	60
5.6	FCC 50 Layer SiPb Resolution	62
5.7	FCC Resolution Curves, All Energies	64
6.1	MIMOSA23 Schematic	71
6.2	ALPIDE Charge Diffusion	73
6.3	ALPIDE Circuitry	74
6.4	ALPIDE Readout Schematic	74
6.5	EPICAL-2 Layer Schematic	76
6.6	CLAWS Module	77
6.7	EPICAL-2 Trigger System	77
6.8	Allpix2 Logic	79
6.9	Allpix2 Geometry Implementation	81
6.10	DESY II Test Beam Schematic	84
6.11	DESY II Primary Collimator Controls	85

6.12	DESY II Secondary collimator	86
6.13	November 2019 Test Beam Setup	87
6.14	February Test Beam Setup	89
6.15	Water-Cooling System	90
6.16	Inclining System	94
6.17	Epitaxial Calorimeter 2 (EPICAL-2) CED Example Events	96
6.18	Low-Event Region	97
6.19	Low-Event Region (Varying Position)	99
6.20	Low-Event Region (Varying Angle)	99
6.21	CLAWS Geometry	100
6.22	Comparison of Feature/Non-Feature Data	100
6.23	Alignment Coordinate System	103
6.24	Multi-Cut Candidate Example	107
6.25	Event Selection Comparison	110
6.26	Low-NHits Event	111
6.27	NHits/NClus Distributions	114
6.28	NHits/NClus Gaussian Fits	114
6.29	EPICAL-2 Linearity	115
6.30	EPICAL-2 Corrected Linearity	117
6.31	EPICAL-2 Resolution	118
6.32	EPICAL-2 Resolution with Beam Spread	119
6.33	Longitudinal Profile	120
6.34	Longitudinal Profile Fits	121
6.35	Shower Axis Determination Layers 0–4	126
6.36	Shower Axis Determination Layers 5–8	127
6.37	Shower Axis Determination Layers 9–12	128
6.38	Shower Axis Determination Layers 13–16	129
6.39	Annular Area Diagram	130
6.40	Lateral Profile	131
6.41	Longitudinal Hit Density Profile	132
6.42	Cluster Size Forward-Backward Asymmetry, Data	134
6.43	Cluster Size Forward-Backward Asymmetry, Simulations	135
6.44	Cluster Size Forward-Backward Asymmetry, Simulations (By Depth)	135
6.45	NHits Forward-Backward Asymmetry, Simulations	137
6.46	Single-layer Geometry Configurations	137

DEFINITIONS OF ACRONYMS

2DFM Two Dimensional Fit of Means

3DFM Three Dimensional Fit of Means

3DFP Three Dimensional Fit of Pixels

AECAL Analogue Electromagnetic Calorimeter

ALICE A Large Ion Collider Experiment
A heavy-ion collision detector at the LHC.

ALPIDE ALICE Pixel Detector
A CMOS MAPS sensor developed for ALICE ITS

APF Allpix Squared Field
A binary file format used for electric field simulation in Allpix².

BSM Beyond the Standard Model

CALICE Calorimeter for the Linear Collider with Electrons
Research and Development collaboration focusing on calorimeter detector development.

CDR Conceptual Design Report

CED C Event Display

CERN Conseil Européen pour la Recherche Nucléaire
European research organisation based near Geneva, Switzerland.

CLAWS sCintillating Light And Waveform Sensors

CLIC Compact Linear Collider

Linear electron-positron collider between 11km and 50km in length, proposed for construction at CERN.

CMOS Complementary Metal-Oxide Semiconductor

DBSCAN Density-Based Spatial Clustering of Applications with Noise

A point-clustering algorithm developed in 1996

DECAL Digital Electromagnetic Calorimeter

DESY Deutsches Elektronen-Synchrotron

National research centre in Hamburg, Germany.

DQM Data Quality Monitoring

ECAL Electromagnetic Calorimeter

EM Electromagnetic

EPICAL-1 Epitaxial Calorimeter 1

Digital calorimeter prototype utilising 96 MIMOSA sensors, developed for ALICE FOCAL.

EPICAL-2 Epitaxial Calorimeter 2

Digital calorimeter prototype utilising 24 ALPIDE sensors, developed for ALICE FOCAL.

FBA Forward-Backward Asymmetry

FCC Future Circular Collider

100km circular collider, designed for both electron-positron and hadronic staging, proposed for construction at CERN.

FCCSW FCC Software

Software package used for simulations of FCC-hh

FOCAL Forward Calorimeter

HCAL Hadronic Calorimeter

HEP High Energy Particle Physics

HL-LHC High Luminosity Large Hadron Collider

High-Luminosity upgrade of the Large Hadron Collider.

ILC International Linear Collider

31km-long linear collider proposed for construction in the Kitakami highlands in Japan.

ILD International Large Detector

One of the two detectors designs for ILC and CLIC

INMAPS Integrated N-well Monolithic Active Pixel Sensor

IPHC Institut Pluridisciplinaire Hubert Curien

ITS Inner Tracker System

LAr Liquid Argon

LCIO Linear Collider Input/Output

LEP Large Electron-Positron Collider

The circular electron-positron collider which operated between 1989 - 2000, and occupied the 27 km ring. Has since been dismantled and replaced by the Large Hadron Collider.

LHC Large Hadron Collider

Superconducting collider occupying the 27 km ring at CERN.

MAPS Monolithic Active Pixel Sensor

MIMOSA Minimum Ionising Metal-Oxide Semiconductor Active pixel sensor

Series of CMOS MAPS sensors developed for IPHC

MIP Minimum Ionising Particle

MPPC Multi-Pixel Photon Counter

NCNG No Cables No Gap

NCWG No Cables With Gap

PCB Printed Circuit Board

PFA Particle Flow Algorithm

PFC Particle Flow Calorimetry

PMOS Positive Metal-Oxide Semiconductor

PMT PhotoMultiplier Tube

PWS Perpendicular With Search

QCD Quantum Chromodynamics

QFT Quantum Field Theory

RAL Rutherford Appleton Laboratory

UK national research laboratory located in Chilcot, Oxfordshire.

RF Radio-frequency

SiD Silicon Detector

One of the two detectors designs for ILC and CLIC

SM Standard Model

SPS Super Proton Synchrotron
7 km circumference proton-antiproton synchrotron at CERN

SUSY Supersymmetry

TAB Tape-Automated Bonding

TCAD Technology Computer-Aided Design

TDR Technical Design Report

TPAC TeraPixel Active Calorimeter

TPC Time Projection Chamber

WCWG With Cables With Gap

WIMP Weakly Interacting Massive Particle

CHAPTER 1

INTRODUCTION

1.1 The Standard Model

The Standard Model (SM) of particle physics is a single Quantum Field Theory (QFT) that attempts to describe three of the four fundamental forces: the Strong [1], Weak [2] and Electromagnetic [3] forces. This theory represents the most complete experimentally verified description of fundamental particles and their interactions. The effects of gravity are vanishingly small in particle physics experiments and not yet integrated in a coherent theoretical framework with the other forces.

The SM comprises twelve fundamental, point-like spin-1/2 fermions, which can be split further into families of six quarks and six leptons. A lepton is defined as a fundamental fermion that is not subject to the strong interaction, and a quark is a fundamental fermion that is subject to the strong interaction. Every fermion has an associated antimatter particle. Additionally, there are four gauge bosons that

mediate the fundamental forces. The list of SM particles and their properties is given in Table 1.1.

Fermions with an electric charge may interact electromagnetically. This occurs via the exchange of the photon, the gauge boson which effectuates the Electromagnetic (EM) force. As the photon carries no charge of its own, it does not self-interact.

The helicity of a particle is defined as the projection of the particle’s spin onto its momentum vector, i.e. $h = \mathbf{S} \cdot \frac{\mathbf{p}}{|\mathbf{p}|}$. As spin is quantised, the helicity is also quantised. Helicity is not Lorentz-invariant for massive particles. A particle with $h > 0$ is said to be ‘right-handed’, while a particle with $h < 0$ is said to be ‘left-handed.’ Chirality is similar in concept to helicity—it is a purely quantum mechanical property, with two states of handed-ness which a particle can occupy: ‘left-chiral’ and ‘right-chiral.’ Chirality is defined using the chirality operator $P_c = \frac{1}{2}(\mathbb{1} \pm \gamma_5)$ and is Lorentz-invariant.

The weak interaction, which is mediated by the Z^0 and $W^{+/-}$ bosons, only couples to left-chiral fermions and right-chiral anti-fermions by coupling to the weak hypercharge—a quantum number relating the chirality and electric charge. As a consequence of this, only left-chiral fermions and right-chiral anti-fermions interact weakly.

While leptons are observed directly, quarks are only observed in bound states of quarks, called hadrons¹. A hadron comprised of three quarks (often denoted qqq) is called a baryon, or an antibaryon ($\bar{q}\bar{q}\bar{q}$) in the case of three anti-quarks. A hadron consisting of a quark-antiquark pair is called a meson ($q\bar{q}$). These are bound by interactions with the strong force.

The theory describing the strong interaction is called Quantum Chromodynamics (QCD) and the gauge bosons mediating this are gluons, which couple with particles based on their colour charge. All quarks and gluons have colour charge. There are three colour values, labelled red r , green g and blue b , each having an equivalent

¹This is not true in the case of the top quark, which decays before hadronisation can occur.

Table 1.1: Particles in the Standard Model [4]. Quark masses are quoted using the $\overline{\text{MS}}$ scheme.

Family	Name	Rest Energy	Symbol	EM Charge	Spin
Lepton	Electron	$510.9989461 \pm 0.0000031$ keV	e^-	-1	1/2
Lepton	Muon	$105.6583745 \pm 0.0000024$ MeV	μ^-	-1	1/2
Lepton	Tau	1776.86 ± 0.12 MeV	τ^-	-1	1/2
Lepton	Electron Neutrino	< 1.1 eV	ν_e	0	1/2
Lepton	Muon Neutrino	< 1.1 eV	ν_μ	0	1/2
Lepton	Tau Neutrino	< 1.1 eV	ν_τ	0	1/2
Quark	Up	$2.16_{-0.26}^{+0.49}$ MeV	u	+2/3	1/2
Quark	Down	$4.67_{-0.17}^{+0.48}$ MeV	d	-1/3	1/2
Quark	Charm	$1.27_{-0.02}^{+0.02}$ GeV	c	+2/3	1/2
Quark	Strange	93_{-5}^{+11} MeV	s	-1/3	1/2
Quark	Top	$172.76_{-0.30}^{+0.30}$ GeV	t	+2/3	1/2
Quark	Bottom	$4.18_{-0.02}^{+0.03}$ GeV	b	-1/3	1/2
Gauge Boson	Photon	0	γ	0	1
Gauge Boson	Gluon	0	g	0	1
Gauge Boson	W	80.379 ± 0.012 GeV	W^+	+1	1
Gauge Boson	Z	91.1876 ± 0.0021 GeV	Z^0	0	1
Scalar Boson	Higgs	125.10 ± 0.14 GeV	H	0	0

anticolour, $\bar{r}, \bar{g}, \bar{b}$, which obey the combination relations $\bar{r} \equiv gb$, $\bar{g} \equiv rb$ and $\bar{b} \equiv rg$. Each quark may have one of the three colour charges, and each anti-quark may have one of the three anti-colour charges. As a result of colour confinement in QCD [5], particles that have non-zero colour charge are postulated to be unobservable, motivated by experiments that have only observed colour-neutral hadrons rather than free quarks or gluons. Mesons comprise a colour-anticolour combination ($\bar{r}r$, $\bar{g}g$ or $\bar{b}b$) while baryons and anti-baryons maintain a combination of all three (rgb or $\bar{r}\bar{g}\bar{b}$), thereby preserving charge neutrality. An isolated quark produced in an interaction will undergo a process called hadronisation, in which it will generate quark-antiquark pairs from the vacuum resulting in a ‘jet’ of colour-neutral hadrons. Additionally, gluons themselves carry more than one colour charge, and these form a colour octet ($\bar{r}g, \bar{r}b, \bar{g}r, \bar{g}b, \bar{b}r, \bar{b}g, \frac{1}{\sqrt{2}}(r\bar{r} - g\bar{g}), \frac{1}{\sqrt{6}}(r\bar{r} + g\bar{g} - 2b\bar{b})$), following a similar formalism to that adopted in the quark model of hadrons [6]. In contrast to the quark model of hadrons, it is postulated that there is no colour neutral gluon state. Similarly, in stark contrast to the case of electromagnetism, gluons, having

Table 1.2: Examples of transformations and the corresponding conserved property if that transformation is symmetric.

Symmetric Transformation		Conserved Property
Spatial translation	→	Total momentum
Rotation	→	Total angular momentum
Time shift	→	Total energy

colour charge, will self-interact. Gluons generated in a vacuum are postulated to also spontaneously produce quark-antiquark pairs via colour confinement, which in turn will undergo hadronisation.

For any interaction involving the exchange of a photon (i.e. an EM interaction), it is also possible to exchange a Z^0 boson. If the momentum transfer is small compared to the Z^0 mass, then the EM interaction dominates and the weak contribution may be neglected. However, if the momentum transfer is sufficiently large, the Z^0 exchange contribution becomes comparable with the photon exchange. This is an example of the electroweak interaction—at sufficiently high energies, the EM and weak interactions behave in the same way. This behaviour is called ‘electroweak unification’.

It is salient at this point to introduce the concept of symmetry. A system is said to be symmetric if its properties do not fundamentally vary under a transformation. Noether’s theorem [7] states that for each transformation under which a system is invariant, there is a correspondent conservation law. Some examples of symmetries and their corresponding conservation laws are given in Table 1.2.

It is important here to distinguish between a global transformation, and a local transformation, and to introduce the idea of gauge theory. A global transformation such as those described in Table 1.2 is one with no space-time dependence i.e. $r \rightarrow r + \epsilon$. By contrast, a local transformation or ‘gauge transformation’ is one with space-time dependence, i.e. $\epsilon \equiv \epsilon(x)$. Properties which are invariant under a gauge transformation are called ‘gauge invariant’. Any field theory which exhibits gauge invariance is called a gauge theory.

The SM is itself a gauge theory, consisting of three separate quantum field theories, one for each of the strong, weak and electromagnetic forces. These symmetries may be represented by unitary matrices, denoted $U(n)$, which are $n \times n$ matrices which obey $\tilde{U}^* = U^{-1}$, and special unitary matrices $SU(n)$, which are unitary matrices which also obey $\det(SU) = 1$. The strong interaction, with its three colour states, is represented by the $SU(3)$ group, effectively describing the invariance between rotation transformations of colour states. We have already touched upon the combining of the EM and weak forces, described by electroweak theory. Left-chiral fermion components interact with both the weak and EM forces, and so are represented by $SU(2)$ symmetry, whereas right-chiral components only undergo EM interactions and so exhibit only $U(1)$ symmetry. The electroweak sector is therefore represented by the combined symmetry group $SU(2) \times U(1)$. Combining these symmetries with the QCD symmetry gives the complete symmetry group of the SM: $SU(3) \times SU(2) \times U(1)$.

A system's dynamics can be described using a Lagrangian, which typically takes the form

$$\mathcal{L} = T - U \tag{1.1}$$

Where T and U describe the kinetic and potential energies respectively. In QFT, a system of fermions is described by the Dirac field $\psi(x)$, and has Lagrangian

$$\mathcal{L}_{Dirac} = \bar{\psi}(x)(i\hbar c\gamma^\mu\partial_\mu - m)\psi(x). \tag{1.2}$$

Under a global phase transition with the form²

$$\psi(x) \rightarrow \psi'(x) = e^{i\alpha}\psi(x) \tag{1.3}$$

$$\bar{\psi}(x) \rightarrow \bar{\psi}'(x) = e^{-i\alpha}\bar{\psi}(x) \tag{1.4}$$

the Lagrangian is unchanged, since $e^{i\alpha}e^{-i\alpha} = 1$.

²The phase is changed by the same amount, independent of its space-time coordinate x .

If instead a local phase transition is considered³ then α now has spacetime-dependence: $\alpha \rightarrow \alpha(x)$ then

$$\partial_\mu \psi(x) \rightarrow e^{i\alpha(x)} \left[\partial_\mu + i\partial_\mu \alpha(x) \right] \psi(x) \quad (1.5)$$

and Eq. 1.2 becomes

$$\mathcal{L}'_{Dirac} = \bar{\psi}(x) i\hbar c \gamma^\mu \partial_\mu \psi(x) - \bar{\psi}(x) m c^2 \psi(x) - \bar{\psi}(x) \hbar c \gamma^\mu \psi(x) \partial_\mu \alpha(x). \quad (1.6)$$

and now gauge invariance is broken. To restore the invariance, the derivative ∂_μ is replaced with the covariant derivative D_μ which is of the form

$$D_\mu = \partial_\mu + ieA_\mu \quad (1.7)$$

where A_μ is a gauge field which transforms as

$$A_\mu \rightarrow A'_\mu = A_\mu - \frac{1}{e} \partial_\mu \alpha(x) \quad (1.8)$$

so that D_μ transforms like $\psi(x)$, leading to

$$D_\mu \psi(x) \rightarrow D'_\mu \psi'(x) = e^{i\alpha(x)} D_\mu \psi(x) \quad (1.9)$$

and now Eq. 1.6 becomes

$$\begin{aligned} \mathcal{L}'_{Dirac} &= e^{i\alpha(x)} e^{-i\alpha(x)} \bar{\psi}(x) (i\hbar c \gamma^\mu D_\mu - m c^2) \psi(x) \\ &= \bar{\psi}(x) (i\hbar c \gamma^\mu D_\mu - m c^2) \psi(x) \end{aligned} \quad (1.10)$$

and invariance is restored. However, we have now introduced a new massless vector field A_μ . This corresponds to one of the vector bosons, namely γ . A similar process may be used for the other vector bosons: g , $W^{+/-}$ and Z^0 . This works perfectly well for the massless photon and gluon. However, as we know from Table 1.1, the vector bosons for the weak interaction are massive. This creates problems, as the

³The phase is instead adjusted as a function of space-time.

Lagrangian for a spin-1 massive vector boson is given by the Proca Lagrangian [8]:

$$\mathcal{L} = -\frac{1}{2}F^{\mu\nu}F_{\mu\nu} + \left(\frac{m_A}{\hbar}\right)A^\nu A_\nu \quad (1.11)$$

Where $F^{\mu\nu} \equiv \partial^\mu A^\nu - \partial^\nu A^\mu$. While $F^{\mu\nu}$ is invariant under the local gauge transformation described in Eq. 1.5, $A^\nu A_\nu$ is not, and so the massive $W^{+/-}$ and Z^0 bosons break local gauge invariance.

In order to address this problem, a scalar field is introduced to cancel out the mass terms and restore local gauge invariance. This is the Higgs field, which takes the form of an $SU(2)$ scalar doublet with a potential:

$$V = \mu^2\phi^*\phi + \lambda(\phi^*\phi)^2. \quad (1.12)$$

where μ and λ are free parameters related to the Higgs mass and self-coupling respectively. This potential develops a non-zero vacuum expectation value in the case that $\mu^2 < 0$, which breaks the $SU(2) \times U(1)$ electroweak symmetry, leaving only a $U(1)$ symmetry group which corresponds to the massless photon. This spontaneous symmetry breaking mechanism gives the Z^0 and $W^{+/-}$ bosons their mass. In order to mediate this interaction, there is of course an additional boson - the Higgs boson [9]. The evidence for this critical part of the SM came in 2012, when a Higgs boson with mass ≈ 125 GeV was discovered [10, 11].

Likewise, the fermion masses originate from the Yukawa coupling between massless fermion fields and the Higgs field. The Higgs, being itself massive, is self-coupling (akin to the ‘coloured’ gluon self-coupling).

1.2 Beyond the LHC

The Large Hadron Collider (LHC) at CERN has taken data between 2010 and 2012 (collision energy of 7–8 TeV), and then from 2015 to 2018 (13 TeV). The third

running period began in 2022, there are at least two more are anticipated with higher luminosity (HL-LHC) and running may end in approximately 2040. Given the time required for the construction of new collider facilities is of the order of decades, it is imperative that the experiment(s) which will replace the LHC be considered imminently, and that the current status of the technology which underpins the physics potential of such experiments be analysed and optimised.

With the discovery of the Higgs boson at the LHC with properties in accordance with those predicted by the SM [12–14], the SM is effectively complete. With this discovery comes the question of which avenues of particle physics research should be pursued now that the SM has been experimentally verified in full.

The SM still leaves unanswered questions. Perhaps the most broadly well-known is the problem of dark matter. Dark matter is the unobserved matter which comprises $\gtrsim 80\%$ of the matter in the universe. The existence of such matter has been inferred from various observations such as galactic rotational curves [15], but there is as yet no observation in particle physics or astrophysics which provides an explanation of what constitutes dark matter. In addition, there still remains the unexplained matter-antimatter asymmetry that we observe in the universe, which is inconsistent with CP violation found in the SM [16, 17], as well as many other examples.

In order to investigate Beyond the Standard Model (BSM) physics it is necessary to consider two complementary approaches: probing the “energy” frontier, or the “precision” frontier. Both strategies have both benefits and drawbacks.

1.2.1 Energy Frontier

The energy frontier collides particles at increasingly high energies, in the hope of finding unexpected physics events which are not predicted by the SM, or setting limits on BSM models in the absence of a direct discovery. The natural choice in this case is to build a hadron collider, akin to the LHC. The choice of hadrons is due to the very large cross-sections that are an intrinsic feature of the dominant strong

interactions in these collisions, as well as the significantly larger centre-of-mass energies achievable. There are additional operational benefits in colliding particles that are stable and have relatively large existence. Many BSM models such as those based on Supersymmetry (SUSY) predict the emergence of new particles with >1 TeV rest masses, which furthers the appeal of the energy frontier.

As hadrons are composite particles (quarks and gluons, or generically ‘partons’), collisions between hadrons at high energies involve the hard scattering between individual partons rather than the hadrons as a whole. These collisions have event-by-event centre-of-mass energies that will differ considerably from the nominal collision energy of the two beams, which makes measuring the momentum at which the hard interactions take place, as well as the particles which underwent the collision, a significant challenge. As the initial state of the interaction is not completely defined, uncertainty is introduced to the predictions, including as a result of the assumed momentum scale of the participating partons. A further consequence of the composite nature of hadrons is the very large cross-section for inclusive QCD jet production, which may hinder the search for very rare physics processes.

The above complications of a hadronic energy frontier collider are well-known, and much work has already done in the context of the LHC to mitigate them. The significant risk with pushing forward into the energy frontier is that the range of the scale at which one might find new physics is currently fairly unconstrained, making choosing a collision energy challenging—too low an energy, and one may miss new phenomena.

1.2.2 Precision Frontier

The precision frontier attempts to determine precisely the properties of already established phenomena, as well as searching for as yet undiscovered ‘ultra-rare’ decay channels [18]. This frontier lends itself more naturally to lepton colliders, as annihilation of fundamental particles allows the initial state of a collision to be de-

terminated precisely, with the precision largely regulated by the quality of the beams. In addition, with the use of polarised electron beams one can preferentially enhance the cross-section for specific processes, e.g. Higgs boson production via WW fusion is increased by a factor of ~ 2 by using left-handed electrons and right-handed positrons [18]. Polarising the beams opens up a whole host of new potential measurements in which one can investigate interactions that have a polarisation asymmetry.

The intention for any proposed lepton collider is to concentrate on Higgs and top quark production and to measure the properties of less well-measured channels of their decays precisely in search of deviations from SM predictions. In the absence of direct discoveries, improved constraints on the parameter space of BSM theories is anticipated.

In addition to providing precision SM measurements, a secondary benefit of lepton colliders is the potential for new discoveries in channels which are difficult to detect in a hadron collider. Light dark matter candidates in particular are a good example of potential new physics which would be complicated by QCD backgrounds. In a lepton collider, backgrounds are relatively small, so detection of these particles can be made much more easily by precise determination of missing momentum in the initial state of interactions.

1.2.3 Circular vs. Linear Colliders

Using a circular collider permits the recycling of bunches of particles, allowing them to be repeatedly collided once they have reached the nominal energy. A circular collider also permits several interaction points, as is the case with the LHC or the Large Electron-Positron Collider (LEP), without reduction of the luminosity at each interaction point. The most significant factors affecting the upper limit of the collision energy for circular colliders are: the average field strength of the dipole magnets, which must be sufficient to maintain the nominal orbit for their momentum; the integrated accelerating gradient to reach the required collision energy; and the provision

of energy to replenish the losses arising from synchrotron radiation. For relativistic particles ($\beta \approx 1$), energy loss through synchrotron radiation is characterised by

$$\frac{\Delta E}{\text{turn}} \approx \frac{k}{\rho} \left(\frac{E}{m} \right)^4 \quad (1.13)$$

where $k = \frac{4\pi q^2}{3\epsilon_0}$ is a constant, ρ is the radius of curvature, E is the particle energy and m is the particle's rest energy.

For hadron colliders, radiative losses are rarely the limiting factor, as the proton is relatively massive. and so the energy loss through synchrotron is small; the dipole magnets constrain the maximum collision energy. In contrast, for lepton colliders the synchrotron losses are the main concern, with losses $\left(\frac{938.27 \text{ MeV}}{0.511 \text{ MeV}} \right)^4 \approx 10^{13}$ times larger relative to a proton collider. As such, future hadron collider designs are circular because the losses from synchrotron radiation are negligible.

Future lepton colliders often use linear accelerator designs. This has the obvious benefit that the path is no longer curved, so energy losses through synchrotron radiation are minimised. However, the linear design means that the collision energy is now severely limited by the length of the accelerator, as the beams only have one pass at the single interaction point before they are transported to beam dumps. The beam must also be constantly replenished, reducing the possible luminosity [19]. The luminosity in particle colliders is defined as [20]:

$$L = \frac{N_1 N_2 n_b f_{\text{rep}}}{4\pi \sigma_x \sigma_y}, \quad (1.14)$$

where N_1, N_2 are the number of particles in each of n_b bunches of particles in beam 1 and beam 2, f_{rep} is the collision frequency at which a given bunch collides at an interaction point, and σ_x, σ_y are the (assumed Gaussian) transverse dimensions of each bunch at the interaction point. To enhance the luminosity at a linear collider, which does not benefit from the very large f_{rep} inherent in a synchrotron, it is therefore essential to use very small transverse bunch sizes. However, there are

consequences of this design choice as discussed below.

1.2.4 Beamstrahlung

For future lepton colliders, one of the most significant benefits over hadron colliders is the precise determination of the initial state of a collision. This is highly dependent on the energies of the colliding beams being precisely determined. However, beam-induced backgrounds present a significant challenge to this approach, by either introducing additional beam-related background particles to the detectors or reducing the momentum of one or both beam particles in the hard collision.

Beamstrahlung is a type of synchrotron radiation which occurs when particles in a beam interact with the strong electromagnetic fields produced by particles in the opposite beam. The necessarily small transverse bunch dimensions in linear lepton colliders generate a high charge density in each bunch, which enhances beamstrahlung production.

The primary result of beamstrahlung is to reduce the momentum of particles in the beam from their nominal value, which in turn reduces the centre-of-mass energy of collision from the nominal. As a result the distribution of centre-of-mass energies from e^+e^- collisions at lepton colliders has a pronounced tail towards considerably lower values than the desired centre-of-mass energy [21].

An additional complication results from further interaction of the radiated photons(s) with the opposite beam. This causes lepton pair-production, further split into coherent and incoherent processes. Coherent pair-production results from interaction of beamstrahlung photons with the magnetic field of the opposite beam, and is the largest mechanism of pair-production in beam backgrounds. Leptons produced by coherent processes are generally high-energy, and are produced at small angles with respect to the beam axis. As such, they have a relatively small contribution to beam-based backgrounds. By contrast, incoherent pair-production is caused by direct interaction of photons with individual particles from the opposite beam. This

can be the interaction between two beamstrahlung photons, one real beamstrahlung photon and one virtual photon associated with a beam particle, or two virtual photons. The rate of incoherent pair-production is much lower than the coherent rate, but the angular distribution of produced particles is far wider. The generally larger transverse momentum of coherent pairs allows them to escape the beam pipe and enter the detector volume, creating a much more significant source of beam-induced background. The interaction of beamstrahlung photons with virtual photons from the opposing beams can lead to two-photon interactions producing hadronic final states. These hadrons can be produced at large angles to the beam axis, and are a significant contribution to the background for the tracker and calorimeter systems of detectors.

Beamstrahlung effects are characterised by the beamstrahlung parameter Υ , which can be approximated by:

$$\Upsilon \approx \frac{5}{6} \frac{r_e^2 \gamma N}{\alpha \sigma_z (\sigma_x + \sigma_y)} \quad (1.15)$$

where $r_e = 2.82$ fm is the classical radius of the electron, γ is the Lorentz factor, N is the number of particles per bunch and σ_z is the longitudinal size of the bunch. The average number of beamstrahlung photons emitted per electron is given by:

$$n_\gamma \approx 1.24 \left[\frac{\alpha^2 \sigma_z}{r_e \gamma} \Upsilon \right] U_0(\Upsilon) \quad (1.16)$$

$$U_0(\Upsilon) \approx \frac{1}{\left[1 + \Upsilon^{\frac{2}{3}} \right]^{\frac{1}{2}}}$$

which leads to the conclusion that n_γ has $\Upsilon^{\frac{2}{3}}$ dependence, and as such has $\sigma_z^{\frac{1}{3}}$ dependence and $(\sigma_x + \sigma_y)^{-\frac{2}{3}}$ dependence. In order to minimise n_γ while maximising the luminosity, linear colliders have flat, ribbon-shaped beams in the transverse plane, so as to maximise $(\sigma_x + \sigma_y)$ while minimising $\sigma_x \sigma_y$ [20].

PHYSICS AT FUTURE COLLIDERS

2.1 The ILC and the CLIC

2.1.1 Introduction to the ILC

The ILC is an electron-positron collider proposed for construction in the Kitakami highlands in Japan [22]. The ILC would take place in three stages: first, a possible first stage at 250 GeV, followed by a 500 GeV stage and finally a 1000 GeV stage. The physics programme of all of these is summarised in Table 2.1. The collider would be approximately 31km in length, including two 11km-long linear accelerators, as shown in Figure 2.1. The ILC would concentrate on constraining interaction parameters of the Higgs, W and Z bosons, and the top quark, as well as searching for new particles predicted by SUSY, or the extended Higgs sector.

The ILC uses two superconducting Radio-frequency (RF) accelerators. An RF accel-

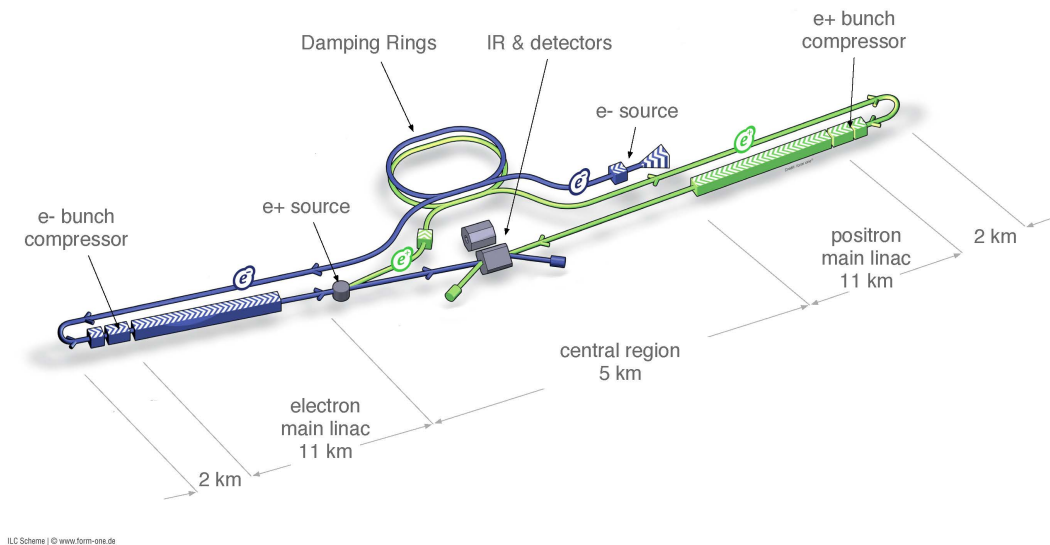


Figure 2.1: Schematic layout of the ILC, indicating all the main subsystems. (Not to scale) Taken from [22].

erator comprises a series of ‘RF cavities’, which are metal chambers. A radio wave or microwave is passed to the cavity which will resonate at a frequency determined by the size and shape of the cavity (1.3 GHz for the ILC). This creates a strong oscillating electric field, which is used to drive the accelerating gradient.

As a result of the oscillation of the E-field, accelerated particles must be separated into short bunches which always see the maximum electric field in each cavity. The ILC accelerators use 5 ‘trains’ of bunches per second, each consisting of 1312 300 μm -long bunches of 2×10^{10} particles separated by 554 ns [22].

The ILC is at the endpoint of its developmental stage and is essentially ready to be built. It is described in the form of a Conceptual Design Report (CDR) and a more comprehensive Technical Design Report (TDR), with a fully developed physics programme and estimates of its performance and requirements at almost all stages of that programme.

Energy	Interaction	Physics Goal
91 GeV	$e^+e^- \rightarrow Z$	ultra-precision electroweak
160 GeV	$e^+e^- \rightarrow WW$	ultra-precision W mass
250 GeV	$e^+e^- \rightarrow Zh$	precision Higgs couplings
350-400 GeV	$e^+e^- \rightarrow t\bar{t}$	top quark mass and couplings
	$e^+e^- \rightarrow WW$	precision W couplings
	$e^+e^- \rightarrow \nu\bar{\nu}h$	precision Higgs couplings
500 GeV	$e^+e^- \rightarrow f\bar{f}$	precision search for Z'
	$e^+e^- \rightarrow t\bar{t}h$	Higgs coupling to top
	$e^+e^- \rightarrow Zhh$	Higgs self-coupling
	$e^+e^- \rightarrow \tilde{\chi}\tilde{\chi}$	search for supersymmetry
	$e^+e^- \rightarrow AH, H^+H^-$	search for extended Higgs states
700-1000 GeV	$e^+e^- \rightarrow \nu\bar{\nu}hh$	Higgs self-coupling
	$e^+e^- \rightarrow \nu\bar{\nu}VV$	composite Higgs sector
	$e^+e^- \rightarrow \nu\bar{\nu}t\bar{t}$	composite Higgs and top
	$e^+e^- \rightarrow \tilde{t}\tilde{t}^*$	search for supersymmetry

Table 2.1: Major physics processes to be studied at the ILC [22]

2.1.2 Introduction to the CLIC

The CLIC is similar to the ILC—it is a linear e^+e^- collider with an extended energy range. The CLIC’s nominal stages are 380 GeV, 1.5 TeV and 3 TeV. Its physics programme is also similar to the ILC, with attention being paid to precision analysis of electroweak interactions, Higgs couplings and properties, top quark physics and BSM studies. The programme for the CLIC concentrates more heavily on Higgs and top physics than the ILC, with the updated baseline concentrating on operation above 1 TeV as early as achievable [23].

In order to achieve the centre-of-mass energies of the CLIC, a higher accelerating gradient than the ILC is required. The CLIC uses a two-beam accelerator to achieve this end shown in Figure 2.2, using a ‘drive beam’ to accelerate the main beam. The drive beam is a long, high-current beam, from which several short high-intensity pulses are extracted, and their energy converted into short RF pulses for use in the accelerator.

The very short RF pulses produced (12 GHz) mean that the bunches used for the CLIC must be necessarily shorter. The CLIC uses 50 bunch trains per second, each

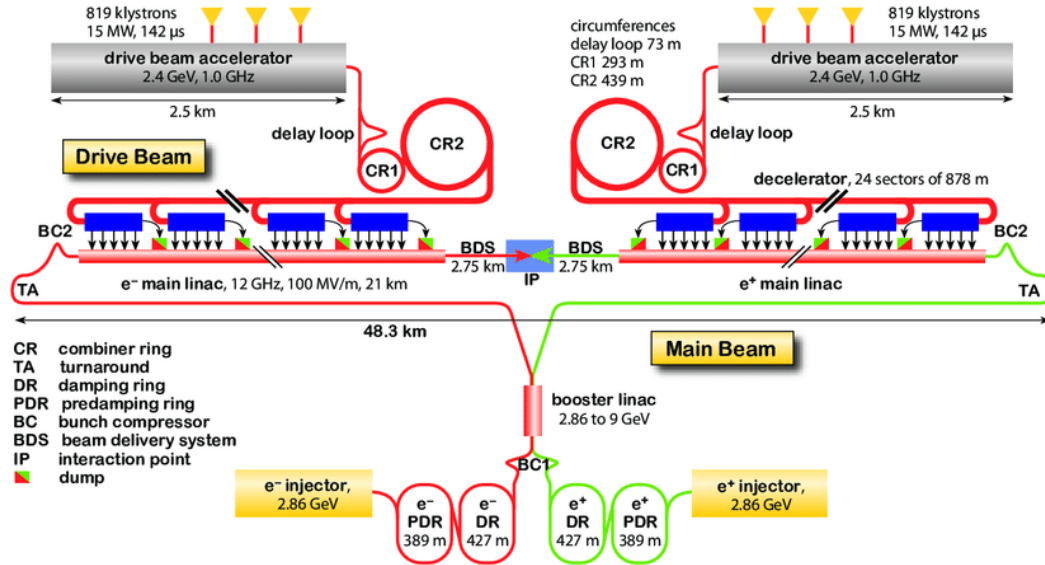


Figure 2.2: Schematic layout of the CLIC, indicating all the main subsystems. (Not to scale) Taken from [24].

Parameter	Symbol [Units]	ILC [27]		CLIC [24]		FCC-ee [28, 29]		FCC-hh [30]
Energy	E [TeV]	0.25	0.5	0.5	3	0.24	0.365	100
Bunch train								
frequency	f_{rep} [Hz]	5	5	50	50	200	200	3850
Bunches/train	n_b	1312	1312	354	312	328	48	10400
Bunch size	N [$\times 10^{10}$]	2	2	0.2	0.2	18	23	10
Bunch spacing	Δt_b [ns]	554	554	0.5	0.5	994	3396	25
Luminosity	\mathcal{L} [$\times 10^{34} \text{cm}^{-2} \text{s}^{-1}$]	0.75	1.8	2.3	5.9	8.5	1.55	25.2

Table 2.2: Major beam parameters for the ILC, the CLIC and the Future Circular Collider (FCC).

comprising 312 70 μm -long bunches of 3.7×10^9 particles, with each bunch separated by just 0.5 ns [25, 26].

2.1.3 Physics at ILC 250 GeV

At a centre-of-mass energy up to and including 250 GeV, the focus is upon precise measurements of the electroweak sector and Higgs couplings. There are three main energy channels in this early stage: Hyper- Z at 91 GeV, WW at 160 GeV and Zh at 250 GeV.

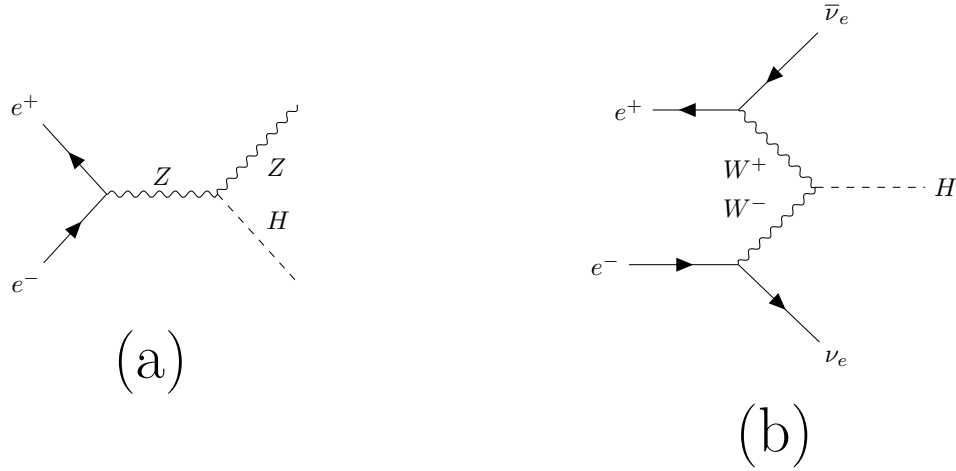


Figure 2.3: Feynman Diagrams of leading order single Higgs production processes at ILC: (a) Higgsstrahlung, left and (b) vector boson fusion, right.

The data recorded at 91 GeV can be used to improve upon the precision of the Z decay width Γ_Z and the mass of the Z , M_Z , although these improvements are relatively small (less than a factor of 3 in both cases [31]). However, it is also possible to use this channel to measure the left-right asymmetry $A_{LR} = \frac{1}{\mathcal{P}} \frac{\sigma_L - \sigma_R}{\sigma_L + \sigma_R}$, where \mathcal{P} is the longitudinal electron polarisation, and $\sigma_{L/R}$ are the cross-sections of left- and right-handed polarised electrons respectively. This in turn can be used to compute the value of the weak mixing angle θ_{eff}^l , with an improvement upon the uncertainty from 0.23146 ± 0.00017 down to $\leq \pm 0.00001$ [31].

In the 160 GeV running, the predominant interest is in measuring more precisely the W mass by performing a threshold scan of W pair production. Preparatory analysis shows that the error on M_W can be reduced to 6-7 MeV at the ILC [31].

The 250 GeV channel is perhaps the most critical in this early stage of the ILC, as this is where the largest improvements of the precision of Higgs couplings can be made, using Higgsstrahlung interactions, $e^+e^- \rightarrow Zh$ (Figure 2.3a). This can be used to measure the Higgs mass using $Z \rightarrow e^+e^-/\mu^+\mu^-$ decays, where the recoil of the Z is used to infer M_h . In the $Zh \rightarrow \mu^+\mu^-X$ decay channel, the ILC will measure M_h with a precision of 40 MeV [31].

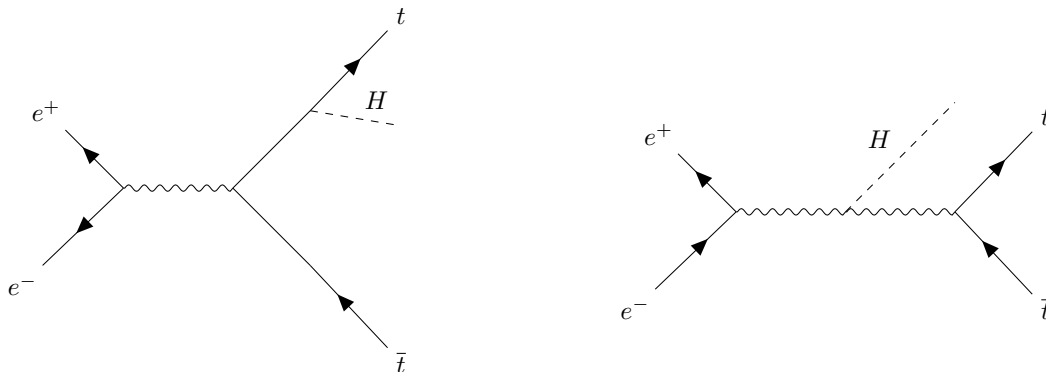


Figure 2.4: Feynman diagrams of $t\bar{t}h$ production at an e^+e^- collider, with the top Yukawa interaction on the left and a possible background event on the right.

2.1.4 Physics at ILC/CLIC 380–500 GeV

The 380–500 GeV run covers a wide variety of physics, including measurements of top quark properties and Higgs couplings, as well as a search for states in the extended Higgs sector and SUSY particles.

In the run-up to 500 GeV, dedicated measurements of top quark properties will take place, as the centre-of-mass energy exceeds the pair production threshold; the CLIC 380 GeV stage is configured precisely for this purpose. This will permit precise measurements of the top mass m_t , its decay width Γ_t and the QCD coupling α_s , in essentially the same way as was done for the WW channel at 250 GeV. A study of the potential of the ILC to constrain the above parameters showed that their uncertainties can be reduced to $\Delta m_t = 19$ MeV, $\Delta\alpha_s = 0.0012$ and $\Delta\Gamma_t = 32$ MeV [32]. Once the 500 GeV energy is reached, it will also be possible to measure the top Yukawa coupling from $e^+e^- \rightarrow t\bar{t}h$, which is shown in Figure 2.4 [31].

In addition, one should be able to measure Higgs couplings to the W via WW fusion, as in Figure 2.3b. While technically this process is possible at the 250 GeV stage, at $\sqrt{s} = 450$ GeV the cross-section of Higgs production overtakes that of Higgsstrahlung, as can be seen in Figure 2.5. With this increased cross-section

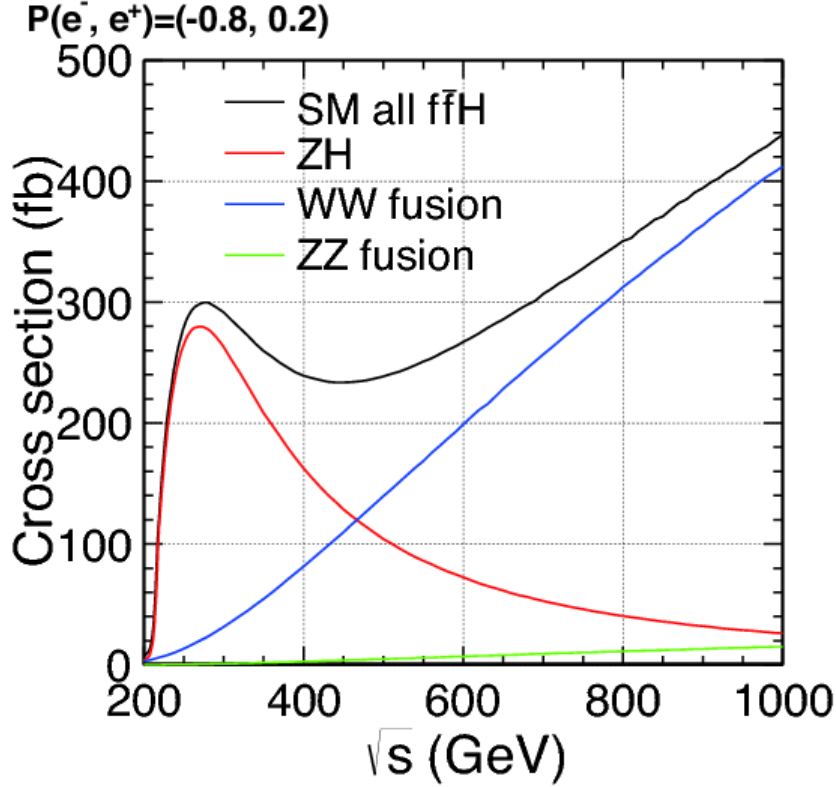


Figure 2.5: Leading order Higgs production cross sections at ILC. Taken from [33].

and increased luminosity at 500 GeV, the ILC should determine the hWW coupling to a precision of $\Delta g_{hWW}/g_{hWW} = 1.4\%$, as well as improving the precision of the $h \rightarrow WW^*$ branching ratio. This in turn can be used to compute the Higgs total width to within an accuracy of $\Delta\Gamma_{tot}/\Gamma_{tot} \simeq 6\%$, using Eq. 2.1 [31].

$$\Gamma_{tot} = \frac{\Gamma(h \rightarrow WW)}{BR(h \rightarrow WW)}. \quad (2.1)$$

At a centre-of-mass energy of 500 GeV, the first observations of Higgs self-coupling can be made from the $e^+e^- \rightarrow Zh\bar{h}$ channel, shown in Figure 2.6a. However, in this case the self-coupling encounters a significant background from di-Higgs production with no triple Higgs vertex, e.g. a Z undergoing two separate instances of Higgsstrahlung.

In terms of BSM physics, two main observations may be made at 500 GeV. Firstly,

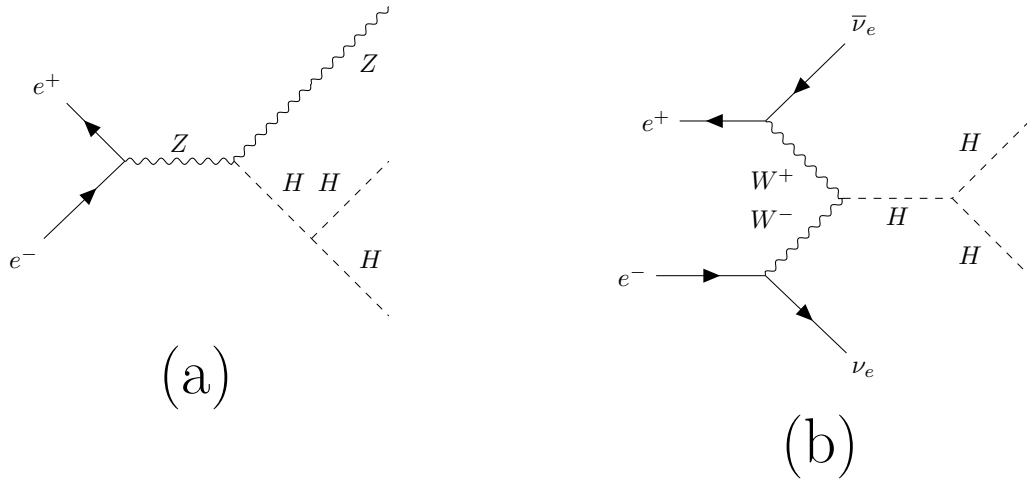


Figure 2.6: Feynman diagrams of double Higgs production with a three-Higgs vertex at an e^+e^- collider.

the search for charginos $\tilde{\chi}_n^\pm$ and neutralinos $\tilde{\chi}_n^0$ (new fermions predicted by SUSY models), which would arise from Z decays at high energy. Secondly, the extended Higgs states will also be examined, as will the analogous charged Higgs case.

2.1.5 Physics at ILC 1 TeV

As \sqrt{s} approaches 1000 GeV, vector boson fusion will begin to dominate Higgs self-interaction production, as described in Figure 2.6b. While the cross-section for this process is lower than that of di-Higgs production from Higgsstrahlung, it benefits from having a much smaller contribution from background di-Higgs processes. Combining this process with Higgs self-interaction from Higgsstrahlung at both 500 GeV and 1 TeV, the ILC would be able to achieve $\Delta\lambda/\lambda \simeq 20\%$ (where $\lambda \equiv g_{hhh}$) [34].

Other physics at the ILC's highest energy stage includes the search for the stop quark in the SUSY model, where a stop decaying to a charm and neutralino can resolve the mass resolution to 0.42 GeV, though the strong SUSY sector is a niche search for lepton colliders. In addition, the composite Higgs model may be investigated by determining the self-coupling strength of the Higgs, which is inflated in composite

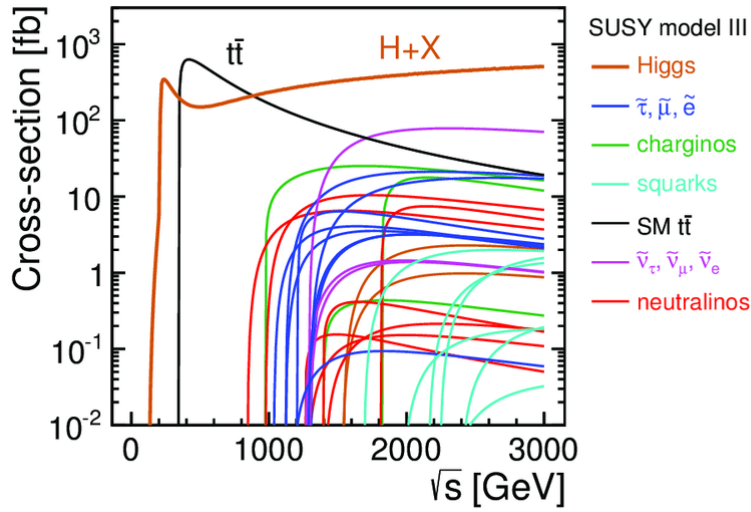


Figure 2.7: Cross-sections of SUSY model III particle production, as an example of the increased scope at the CLIC 1.5 TeV and 3 TeV stages. Taken from [24].

models, by studying Higgs decays to vector bosons ($e^+e^- \rightarrow \nu\bar{\nu}VV$) and top quark pairs ($e^+e^- \rightarrow \nu\bar{\nu}t\bar{t}$) [31].

2.1.6 Physics at CLIC 1.5/3 TeV

One of the advantages of the higher energy stages at the CLIC is that one can further refine the precision on properties studied at the ILC's 500 GeV and 1 TeV stages. As an example of this, with a combination of the CLIC's 380 GeV, 1.5 TeV and 3 TeV runs, using Higgsstrahlung and vector boson fusion in conjunction with Higgs decay into $b\bar{b}$ would provide an uncertainty on the Higgs mass of just 24 MeV utilising beam polarisation - almost half that achievable at the ILC alone [23].

Another advantage of the increased energy stages at the CLIC is the sheer number of SUSY models which can be analysed at these higher energy stages. As can be seen in an example plot in Figure 2.7, the transition from 1 TeV to 1.5 TeV gives the potential to discover many SUSY particles, as does the jump between 1.5 TeV and 3 TeV. This additional energy allows either the systematic elimination of SUSY models, or the detailed exploration of properties if some new physics is discovered.

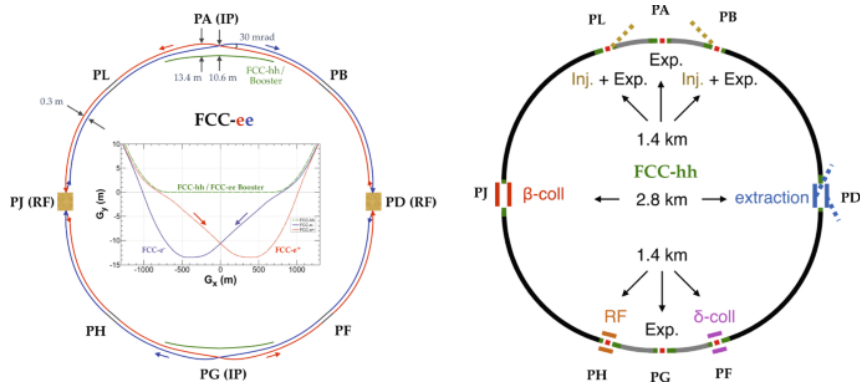


Figure 2.8: Schematic of the FCC-ee accelerator (left) and the FCC-hh accelerator (right). Taken from [28].

2.2 FCC

2.2.1 Introduction to the FCC

The FCC is a synchrotron collider with a circumference between 80 km and 100 km.

The FCC has three potential modes of operation:

- proton-proton collisions at centre-of-mass energies up to 100 TeV, under the heading “FCC-hh.”
- electron-proton collisions at centre-of-mass energies of approximately 3.5 TeV, under the heading “FCC-eh.”
- electron-positron collisions at centre-of-mass energies from 90 GeV up to 350 GeV, under the heading “FCC-ee.”

The FCC timeline involves the initial installation and running of FCC-ee, before replacing the FCC-ee accelerator with the FCC-hh system in the same tunnel.

The FCC-ee accelerator uses a two-aperture synchrotron design, as shown in Figure 2.8. It uses two straight 400/800 MHz (dependent on the desired beam energy) RF sections as the primary accelerators, with 2900 dipole magnets used to maintain a circular trajectory. The separation of the electron and positron beams helps

minimise beam-beam interactions. The bunch characteristics of FCC-ee are highly dependent upon the beam energy: the lowest proposed beam energy of 45.6 GeV uses bunch trains of 16640 bunches, each containing 1.7×10^{11} particles and separated by 19.6 ns, whereas the highest proposed beam energy of 182.5 GeV uses bunch trains of just 48 bunches, each containing 2.3×10^{11} particles and separated by 3396 ns [28].

The FCC-hh accelerator is similar in premise to that of FCC-ee, instead using a single beam aperture. It uses a single straight RF system, with strong (~ 16 T) dipole magnets used to bend the proton beam and collimating sections to ensure that the beam profile is sufficiently small, both laterally (β collimator) and longitudinally (δ collimator). The 50 TeV proton beams use bunch trains of 10400 bunches, each containing 1×10^{11} protons and spaced by 25 ns [30].

The FCC is less well developed than either the CLIC or the ILC, with a CDR agreed in late 2018 [36]. However, it has a well-developed physics case, and with a baseline detector and many studies contributing to its development across all elements of the design it is fast establishing itself as a significant competitor.

2.2.2 Physics at FCC-ee and FCC-eh

The physics at FCC-ee is similar to the ILC and the CLIC at energies up to 350 GeV, as its purpose is very similar—to provide precise measurements of top, vector boson and Higgs physics at their production thresholds rather than probing for new BSM physics. The precise parameterisation of these interactions can then be used to assist in understanding the physics output of FCC-hh, by reducing the uncertainty introduced with these parameters. It differs most significantly in that it offers substantially higher integrated luminosity while having an inherent upper limit in its centre-of-mass energy due to synchrotron radiation.

While FCC-eh does not maintain the precision measurements of FCC-ee, it does not suffer from the intrinsic complexity of proton interactions as much as FCC-hh while

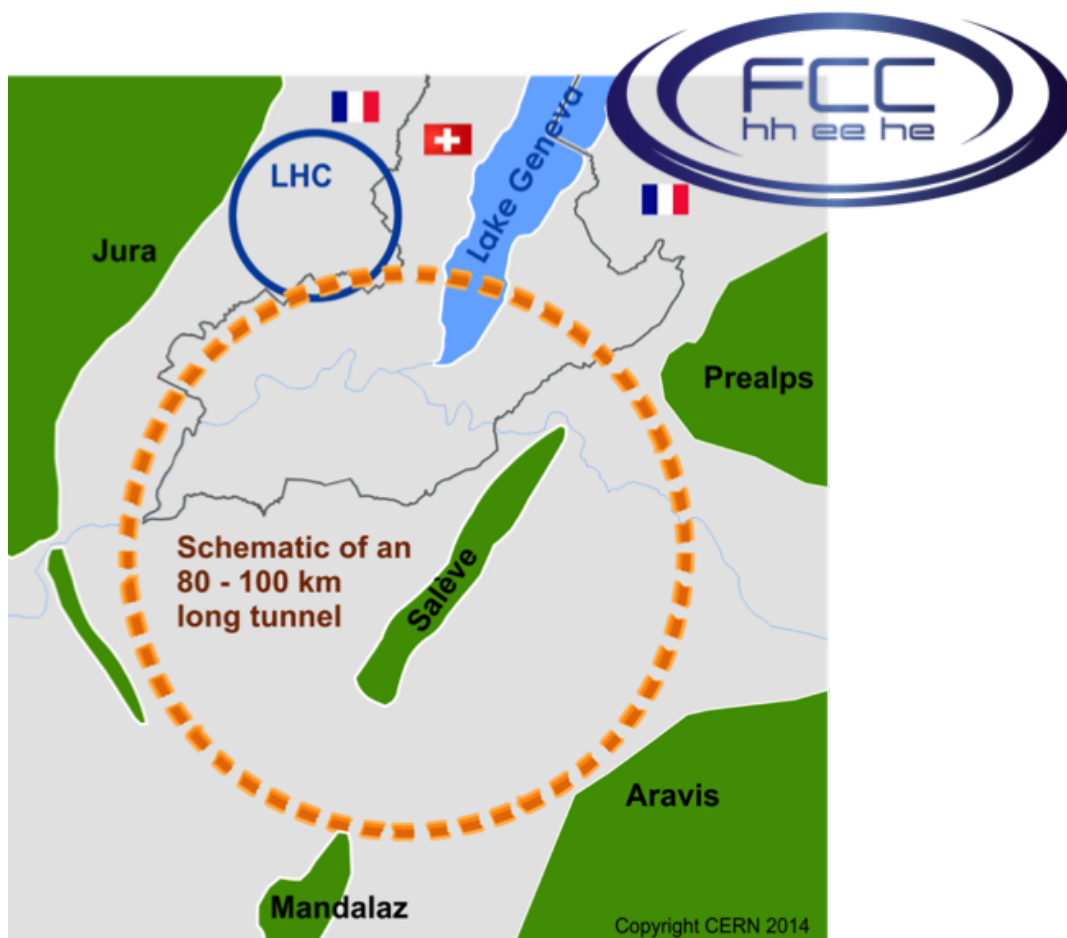


Figure 2.9: Map of the FCC's proposed location in comparison to the LHC. Taken from [35]

still being able to probe the several-TeV region. For this reason, it may be a suitable method of producing a high cross-section of Higgs production by vector boson fusion, as well as probing top physics and electroweak couplings at higher energies than is possible at FCC-ee.

2.2.3 Physics at FCC-hh

As the nominal figurehead of the FCC's programme, FCC-hh promises to use its 16 T magnets to increase the pp collision energies from those of the LHC up to 100 TeV. This significant increase in centre-of-mass energy would allow a wide variety of physics to be probed, including investigations of Higgs physics, electroweak symmetry breaking, and particularly BSM phenomena.

The high energy of FCC-hh allows for significant advances in the search for a high mass dark matter candidate, either by direct detection of a new particle or by indirect detection via 'missing energy' searches, where one finds a particle recoiling off an undetectable Weakly Interacting Massive Particle (WIMP) or other weakly interacting dark matter candidate [37].

Another sector open to investigation in 100 TeV hadron collisions is the prospect of finding new SUSY particles, at energies inaccessible to proposed lepton colliders. With FCC-hh one could search for many SUSY particles at multi-TeV energies far beyond the reach of the LHC e.g. the stop mass discovery reach of High Luminosity Large Hadron Collider (HL-LHC) is ~ 1.7 TeV [38], while the same discovery reach of FCC-hh is ~ 8 TeV [39]. The discovery potential of a lepton collider is constrained to $\frac{\sqrt{s}}{2}$, and so the maximum given by CLIC is 1.5 GeV [24]. In some models, this is easily sufficient to promote one or more discoveries. Of course, if these discoveries are not made, it is also useful to eliminate models which do not produce the expected results [37].

Top physics searches at FCC-hh are primarily focused around the top Yukawa coupling, as a consequence of the increased cross-section of $pp \rightarrow t\bar{t}h$ from 0.47 to

33.2 pb as the centre-of-mass energy goes from 13 to 100 TeV [40].

Multiple Higgs production is also enhanced compared to the LHC, which lends itself to probing Higgs trilinear self-coupling events. These can be used to search for corrective factors to SM predictions as a possible investigation of BSM physics [41].

PARTICLE DETECTOR METHODS FOR FUTURE COLLIDERS

3.1 Particle Detectors

A well-motivated physics case for building accelerators is futile if it is not supported by a detector of sufficient quality, which can be used to characterise events from their decay products. Detectors should ideally be able to determine the momenta of particle products and their energies, their charges and their path through the detector. Neutrinos, for example, only interact weakly, so in most particle collisions they do not appear directly and must be inferred from measuring other products. Most modern general purpose detectors comprise of four main subsystems, as shown by Figure 3.1.

The four main elements of a hermetic detector are:

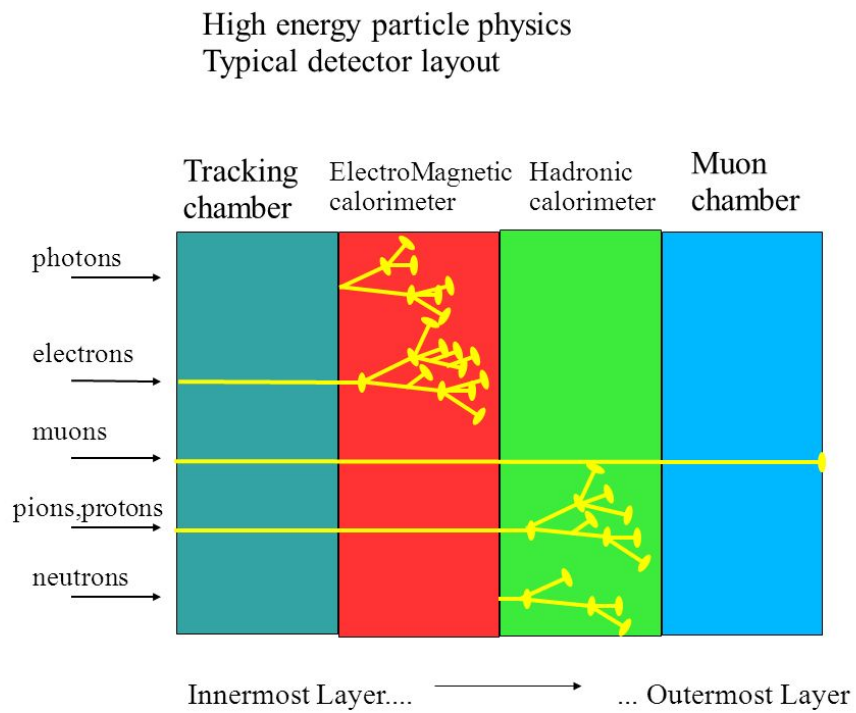


Figure 3.1: Schematic diagram of the main components of a hermetic detector and where various products interact. Taken from [42].

- an inner tracking device, used for position and momentum measurement, charge determination and also triggering for outer detector components.
- an Electromagnetic Calorimeter (ECAL), used to measure the energy of electrons and photons in the collision products.
- an Hadronic Calorimeter (HCAL), used to measure the energy of hadronic collision products.
- an outer muon tracker, used to identify muons that have escaped the other detector components.

Some detectors also include elements in the angular region close to the beamline (“forward calorimeters”) to provide sensitivity to particles that have a low transverse momentum. Information from the various elements is combined to reconstruct the kinematics of an event, and at proposed lepton colliders the use of a Particle Flow Algorithm (PFA) designed for this purpose is commonly used. Since the work of the author is primarily concerned with the ECAL, special focus will be given to the requirements and design of an ECAL for future colliders.

3.1.1 Inner Tracking Devices

Tracking devices measure both the position and the momentum of particles as close as possible to the interaction point. It is also desirable to have minimal material to avoid degrading the momentum measurement due to multiple Coulomb scattering and to avoid degrading the energies measured in the calorimeters. Trackers therefore need very fine granularity to distinguish separate tracks with precise positional measurements.

Trackers determine both the momentum and charge of an incoming particle by measurement of its trajectory in a region of known magnetic field, often parallel to the beam direction. Trackers can also be used as a trigger mechanism, particularly for

applying thresholds to the transverse momenta of charged particles, jet separation, and the number of particles in events.

3.1.2 Muon Trackers

The muon tracker in a detector is used to identify and track muons, which are the only detectable particles (neutrinos detection is next to impossible in detectors attached to particle colliders) to pass through the large amount of material present in calorimeters. The principle can be similar to the inner tracker: track the position of the muon as it propagates through the detector, and use an externally applied magnetic field to determine its momentum.

3.1.3 HCALs

The HCAL exists to measure the energy of hadronic components of collision products. The showers produced by hadronic interaction products are complex and highly topologically variable, as there are many processes which contribute to the shower development. Hadronic showers also extend over larger volumes than EM showers, as hadrons interact less readily with atomic nuclei than EM particles. These factors mean that the energy resolution of HCALs tends to be significantly poorer than that of ECALs. As a consequence of the greater depth of hadronic showers, HCALs are generally deeper than ECALs.

3.1.4 ECALs

An ECAL measures the energy of photons and electrons as well as providing positional information and the electromagnetic components of other particles such as charged hadrons or muons. This may either be done by measuring the total energy deposited by an EM shower within the ECAL volume, or else by reconstructing the shower

energy using the sampling fraction. The specifics of EM interactions, their impact on ECAL design and ECAL performance characterisation are discussed in detail in Section 3.2 below.

3.2 Electromagnetic Calorimetry

Calorimetry systems in High Energy Particle Physics (HEP) detectors are typically divided into the ECAL and HCAL, which reflects the differing interactions of particles that interact primarily through EM processes (electrons¹ and photons) and hadronic processes. This thesis pertains specifically to ECAL performance, and so it is important to discuss in detail the processes by which EM particles interact with detector materials.

3.2.1 Electromagnetic Interactions

At high energies, when an electron interacts with atomic nuclei in a material, it may radiate a photon through bremsstrahlung. Photons with sufficiently high energy will similarly interact with the electric field of a nucleus to produce an electron-positron pair. These processes continue, creating an EM shower until the energy of electrons reduces to E_c , when ionisation is the dominant energy loss process rather than bremsstrahlung, after which the multiplication of particles within the shower diminishes.

The development of an EM shower is characterised by the radiation length χ_0 and critical energy E_C . The radiation length is defined as the distance travelled by an electron after which its energy is reduced by a factor of $1/e$ by bremsstrahlung. It is also equivalent to $7/9$ of the mean free path for pair production of electrons. The energy loss by radiative effects for electrons with $E \gg \frac{mc^2}{\alpha Z^3}$ is therefore approximately

¹Unless stated otherwise, charge conjugation is implicit throughout

$$-\frac{dE}{dx} = \frac{E_0}{\chi_0} \quad (3.1)$$

and likewise the mean free path λ for photons in the same energy region is dominated by pair production:

$$\lambda \approx (n_a \sigma_{pair})^{-1} = \frac{9}{7} \chi_0 \quad (3.2)$$

where σ_{pair} is the cross-section for pair production and n_a is the number density of atoms in the medium.

The radiation length of a material can be approximated for atoms with $Z < 93$ using the following parameterisation [4]:

$$\chi_0 \approx \frac{716.4(\text{ gcm}^{-2})A}{Z(Z+1) \ln\left(\frac{287}{\sqrt{Z}}\right)} \quad (3.3)$$

where Z is the atomic number and A is the atomic mass. The critical energy of a material is the energy at which the rate of energy loss by electrons via radiative processes and energy loss via ionisation are equal.

The mean longitudinal profile of energy deposition in a medium can be described by the parameterisation [4]

$$\frac{dE}{dx} = E_0 b \frac{(bx)^{a-1} e^{-bx}}{\Gamma(a)}, \quad (3.4)$$

where E_0 is the initial energy of the particle, a and b are material-specific properties, and $\Gamma(a) = \int_0^\infty t^{a-1} e^{-t} dt$ is the gamma function. As a result of the exponential term, complete shower containment is hard to ensure so the depth of the detector must be established appropriately according to the acceptable level of leakage.

The transverse profile of the EM shower is described by the Molière radius R_M , defined as the radius within which 90% of a particle's energy will be deposited. This

is related to the radiation length of the detector by

$$R_M = \frac{21\text{MeV}}{E_c} \chi_0. \quad (3.5)$$

It is desirable to design the detector to have a small Moliere radius, to control the overlap between nearby showers. This requires both careful choice of the passive radiator and design of the overall system including the active layers, readout and services.

3.2.2 Homogeneous Calorimeters

Homogeneous calorimeters are those comprised of a single medium, which acts as both the sensitive region and as the absorber material in which the shower develops. Such calorimeters typically consist of a crystal material which produces Cherenkov light or light from scintillation in the presence of a high-energy electron. The generated photons are converted to a digitised signal using a PhotoMultiplier Tube (PMT). The choice of material must have a small radiation length to ensure that the shower is sufficiently contained, and also be optically transparent to allow photons to reach the PMTs.

Homogeneous calorimeters generally have excellent energy resolution [43, 44], as the energy of the entire shower (presuming complete containment) is deposited in the active medium. However, the depth of material required to contain showers is generally large, and the crystals used must be very pure to ensure uniform efficiency across the whole detector. The production of appropriate materials is therefore both difficult and expensive. There are implications for the position resolution of showers due to the required segmentation.

3.2.3 Sampling Calorimeters

In contrast to homogeneous calorimeters, sampling calorimeters use differing materials for the sensitive region and the absorber region of the detector, segmented into several layers. The absorber region induces the EM shower, producing many low-energy particles which the sensitive region samples to produce a signal.

The absorber material must have a small radiation length to ensure shower containment, and so generally consists of high- Z materials such as tungsten, lead or steel (see Equation Eq. 3.3). The sensitive material is generally a low- Z easily ionising material, such as silicon or a plastic scintillator [44].

Since the sensitive region measures only a fraction of the total material in the full detector, this is corrected to infer the full energy of the incident particle using the ‘sampling fraction’ \mathcal{F}_i . This is defined as the ratio of the energy a Minimum Ionising Particle (MIP) deposits in the sensitive region of layer i , E_i , and the energy deposited by a MIP in both the passive material $E_i^{passive}$ and sensitive material of the same layer:

$$\mathcal{F}_i = \frac{E_i}{E_i + E_i^{passive}} \quad (3.6)$$

The total energy of an incident particle E_0 is then given by:

$$E_0 = \sum_{i=0}^N E_i / \mathcal{F}_i, \quad (3.7)$$

assuming that the full shower energy is contained within the calorimeter.

As a result of fluctuations in the deposition of energy in each sampling layer, the smaller the sampling fraction the poorer the energy resolution becomes. Therefore, an ideal sampling calorimeters will have as large a sampling fraction as possible. This must be balanced with the required depth of absorber material required to contain the shower, as well as the cost (more readout channels or more expensive sensitive material).

While the energy resolution of a sampling calorimeter is generally worse than that of a homogeneous calorimeter, it is generally cheaper and easier to produce the required components. Sampling calorimeters also tend to have better position resolutions than homogeneous calorimeters, as the difficulties in segmenting high-purity crystals are not present.

3.2.4 Energy Resolution

The energy resolution, $\frac{\sigma}{E}$, is the main figure-of-merit quantifying the performance of an ECAL, and is driven by several factors, each of which has its own energy dependence:

- The particle-by-particle interactions are governed by quantum mechanics and so are statistical in nature. The number of particles N in a shower follows a Poisson distribution, which for high multiplicity processes will have an uncertainty $\propto \frac{1}{\sqrt{N}}$. Since N is proportional to the energy of the incident particle E , the uncertainty in the energy depends on $1/\sqrt{E}$.
- As EM particles lose energy, their range in the absorbing material is diminished significantly. If the absorbing layer is thick enough, the fraction of low-energy particles reaching the following sensitive layer is reduced. Fluctuations in the number of particles reaching the sensitive material causes an uncertainty of $\frac{\sigma_{samp}}{\sqrt{E}}$, where $\sigma_{samp} = \sqrt{E_c t_{abs}}$ and t_{abs} is the thickness of the absorbing material in radiation lengths.
- Particles will traverse the ECAL at many different angles, and as such will pass through different depths of absorbing material between sampling layers. This creates a per-particle variation of t_{abs} which must be accounted for. As energy deposition for thin layers of material follows a Landau distribution (unlike the Gaussian distribution for thick materials), the scaling of energy deposition for small variations in t_{abs} introduces an additional uncertainty of $\frac{\sigma_{landau}}{\sqrt{E}}$.

- Within the sampling layers, there are intrinsic fluctuations in the conversion of ionising EM particles to photoelectrons or electron-hole pairs. These fluctuations affect the size of the induced signal, and thus the energy resolution. As the number of photoelectrons N_{pe} is proportional to the energy of the ionising particle, and fluctuations in this number follow a $\frac{1}{\sqrt{N_{pe}}}$ relationship, the energy resolution has a further uncertainty of $\frac{\sigma_{pe}}{\sqrt{E}}$.
- Electronic noise from the readout systems in the sampling layers introduces another uncertainty term. This noise is presumed to be constant and signal-independent, and so the uncertainty term is described by $\frac{\sigma_{noise}}{E}$.
- Any miscalibration of the ECAL will introduce an additional uncertainty, similar to the noise term, which is also characterised by a $\frac{\sigma_{calib}}{E}$ term.
- Finally, as discussed in Section 3.2.1, it is not possible to guarantee that the shower is completely contained within the ECAL. As such, an additional uncertainty caused by leakage is added. Longitudinal leakage, caused by the calorimeter being too thin to contain the entire shower, is less significant than lateral leakage, which is the result of the Molière radius of the shower exceeding the lateral limits of the ECAL volume [45]. The leakage is described by a constant term in the energy resolution σ_{leak} , which becomes more significant for larger energies. This can be seen in Eq. 3.4, where the longitudinal profile of energy deposition is dependent on the initial energy of the particle.

The above contributions to the energy resolution are summed in quadrature ($a \oplus b = \sqrt{a^2 + b^2}$) to give the overall energy resolution:

$$\frac{\sigma}{E} = \frac{\sigma_{shower}}{\sqrt{E}} \oplus \frac{\sigma_{samp}}{\sqrt{E}} \oplus \frac{\sigma_{landau}}{\sqrt{E}} \oplus \frac{\sigma_{pe}}{\sqrt{E}} \oplus \frac{\sigma_{noise}}{E} \oplus \frac{\sigma_{calib}}{E} \oplus \sigma_{leak} \quad (3.8)$$

Terms with the same energy dependence are commonly grouped together, to produce the general equation for the energy resolution:

$$\frac{\sigma}{E} = \frac{a}{\sqrt{E}} \oplus \frac{b}{E} \oplus c, \quad (3.9)$$

where a , b and c are called the stochastic, noise and leakage terms, respectively.

3.3 Particle Flow Calorimetry

In conventional calorimeter systems, the energy of e.g. a hadronic jet was found by summing the energy contributions from the ECAL and HCAL, modified by the sampling fraction in each case. A single hadronic jet typically comprises roughly 30% photons, 10% long-lived neutral hadrons and 60% charged particles, of which most are hadrons. The intrinsically poor resolution of HCALs means that this method produces an overall resolution of $> \frac{60\%}{\sqrt{E[\text{GeV}]}}$, which is much worse than the requirements for future colliders at around $\frac{30\%}{\sqrt{E[\text{GeV}]}}$.

Particle Flow Calorimetry (PFC) is an approach which attempts to address the problem above. Rather than relying entirely on calorimetric measurement of jet energies, particle flow calorimetry attempts to reconstruct the four-vectors of every visible particle in each event. The momenta of charged particles are determined by measuring their radius of curvature in the tracking detectors. The photon momenta are determined by the ECAL and the neutral hadron momenta determined by the HCAL. This reduces the reliance on the HCAL performance so that it used to measure just 10% of the energy in a jet, rather than the 70% using conventional calorimetry.

The limiting factor in PFC is the ability to associate energy deposits in the detector with the correct particles. For this reason, the calorimeter systems of detectors designed for PFC must be highly granular to distinguish energy deposits from different but colinear jet components. Pattern recognition using a PFA is used to optimise the association of energy deposits with reconstructed particles.

To satisfy the requirement to identify charged particles using the inner tracker systems and calorimeters to measure the curvature of these particles, a magnetic field

must be applied across the trackers and calorimeters (generally this is approx. 4 T.) This requires that the inner trackers, ECAL and HCAL are within the detector magnetic field. The cost of this large magnet is highly dependent upon the volume over which it is required. It is therefore important that the inner components be as compact as possible, since an increase in the radius of inner components has a knock-on effect upon the volume and cost of detector components further out. This is exemplified by the difference in projected cost between the International Large Detector (ILD) and Silicon Detector (SiD) detectors for the CLIC. The increased size of the vertex detector and inner tracker in the CLIC_ILD (1.8 m, compared to the 1.3 m of the CLIC_SiD) has a knock-on effect upon the size of the ECAL, HCAL and solenoid, which brings the cost up to 560 MCHF, compared to 360 MCHF for the CLIC_SiD [24].

3.4 Analogue ECALs for Particle Flow

Due to the requirement for high granularity, ECALs for PFC in future colliders are generally sampling calorimeters, using either silicon pads to achieve fine segmentation, or scintillator strips arranged orthogonally to one another. These are sandwiched with tungsten passive layers in order to minimise the depth of the ECAL in radiation lengths while keeping the detector compact. Studies for the CLIC have shown that a cell size smaller than $5 \times 5\text{mm}^2$ is sufficient for these applications, and that the resolution improves for all jet energies as the cell size decreases [21].

3.5 Digital Calorimetry Concept

While conventional ‘analogue’ calorimetry aims to measure either the entire energy of particles and their resultant showers entering the calorimeter (see Section 3.2.2) or a fraction of the shower with the aim of reconstructing the total energy (see Section 3.2.3), digital calorimetry instead attempts to count the number of particles

in a shower. Since the number of particles in an electromagnetic shower is proportional to the total energy of the incident particle producing the shower, if the number of particles can be precisely and accurately obtained, the total energy can be reconstructed by a simple linear relationship.

Rather than measuring the energy deposited in each pixel, each cell in a Digital Electromagnetic Calorimeter (DECAL) has a single charge threshold. If the charge collected in that pixel exceeds the threshold, a digital ‘hit’ is returned. To ensure a linear response, this method requires that each pixel is dominated by the energy deposit of a single shower particle. Non-linearity implies non-uniformity of response, which introduces a potential topological dependence to the energy determined, based on how the hits are attributed to incident particles [46].

3.6 The Case for Digital Calorimetry

The main drawback to the use of digital calorimetry is the effect of saturation. If multiple shower particles traverse the same pixel in an Analogue Electromagnetic Calorimeter (AECAL), the result is merely an increase in the output signal, which can be accounted for using a reconstruction algorithm. By contrast, in a digital calorimeter there is no change in the output signal compared to that of a single through going particle. Each instance of multiple pixel occupancy results in an underestimation of the number of shower particles, and by extension the energy of the incident particle.

The peak density of an electromagnetic shower increases with the incident particle energy, so the higher the energy of incident particles the larger the effect of saturation is, causing a non-linearity effect at higher energies. As an example, the peak density of electromagnetic showers at the ILC is estimated to be $\mathcal{O}(100 \text{ particles/mm}^2)$, and so a digital calorimeter designed for this collider requires pixels no larger than $50 \times 50 \mu\text{m}^2$ [47].

By counting particles, the effect of Landau fluctuations in the amount of energy deposited by each particle can be mitigated by careful selection of the pixel threshold, which should result in an improvement in the energy resolution compared to that of an analogue ECAL by removing one source of fluctuation. However, the potential improvement in resolution from Landau fluctuations is balanced against the degradation in resolution for higher energies; for energies ($> \mathcal{O}(200 \text{ GeV})$) the single-particle resolution is generally poorer for a DECAL than in the analogue case.

The ultra-high granularity of a DECAL lends itself to use in a PFA, where the excellent position resolution provides additional discriminating power between nearby particles. This means that while individually DECALs tend to provide poorer energy resolutions at high energies than analogue ECALs, when coupled with a tracking system which is used to measure the momentum of charged particles the hadronic jet energy resolution is significantly improved. Simulation studies of a DECAL applied to the ILC ILD have shown that the energy resolution of reconstructed $Z \rightarrow u\bar{u}$, $Z \rightarrow d\bar{d}$ and $Z \rightarrow s\bar{s}$ events is comparable to that found with the nominal ILD analogue ECAL [48].

Lastly, the prevailing choice of sensors for DECAL applications is Complementary Metal-Oxide Semiconductor (CMOS) Monolithic Active Pixel Sensor (MAPS), as will be discussed below. Production of CMOS MAPS is already well-established for commercial use, for example in digital cameras. The mainstream application of these sensors has the potential to make it a cheaper alternative to analogue calorimeters. This is aided by the fact that CMOS MAPS is already the proposed technology for inner tracker systems; using the same technology would potentially reduce costs further, as well as allowing uniformity across several detector systems.

3.7 Signal Generation in Silicon Sensors

As will be detailed in Section 3.8 below, the prevailing sensor technology for DECAL applications is silicon-based. This section introduces the mechanisms by which an

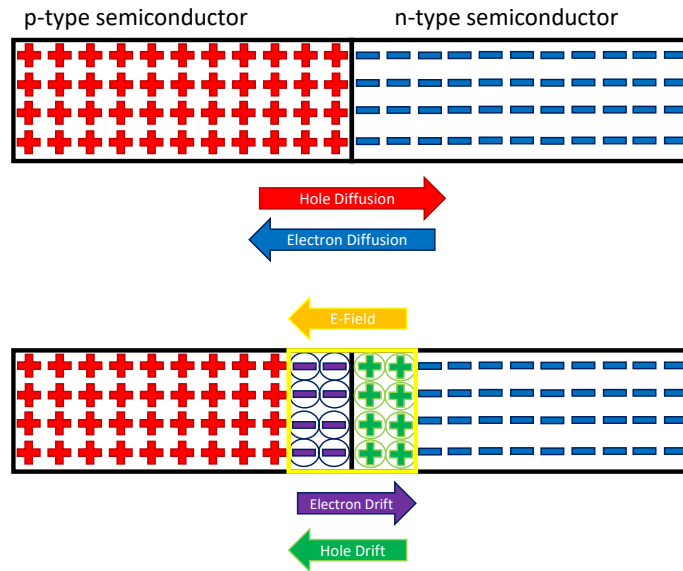


Figure 3.2: Illustration of the process creating the depletion region in a p-n junction..

incident MIP triggers a signal in a silicon sensor.

A MIP traversing a volume of silicon gives electrons in the valence band sufficient energy to escape the atom. The absence of the freed electron leaves behind a ‘hole’ in the valence band, which acts as if it were a positively charged particle. The generation of electron-hole pairs in silicon requires 3.63 eV of energy, and a MIP traversing silicon will generate ~ 80 e/h pairs per μm [49].

In the absence of an electric field, the electron and hole would rapidly recombine (i.e. the electron would drop back into the valence band, releasing a photon in the process.)

Non-uniform doping of the silicon volume creates a concentration gradient of charge carriers. Electrons and holes will diffuse across the silicon volume following the concentration gradient, with no requirement for an external electric field. The current generated by this movement is denoted the diffusion current.

If an external electric field is applied to the silicon volume, freed e/h pairs will drift

in the opposite/same direction as the field respectively. The induced current from charge carrier drift is called the drift current.

Doping one silicon region with an n-type agent, and p-doping an adjacent region creates a p-n junction. This results in a gradient across the junction between the conduction and valence bands. Electrons from the conduction band of the n-doped region diffuse towards the p-doped region, and holes from the valence band of the p-doped region diffuse towards the n-doped region, creating a fixed charge in its place and in so doing inducing an electric field, which in turn produces charge carrier drift. Once the carrier diffusion and carrier drift reaches equilibrium, a depletion region remains, in which there are no charge carriers and an electric field. This process is depicted in Figure 3.2. Electron-hole pairs generated by a through going particle in the depletion region will drift as a result of the E-field.

The size of the depletion region can be further increased by the application of a reverse bias voltage. Holes are pulled toward the cathode in the p-doped region and electrons toward the anode in the n-doped region.

3.8 CMOS MAPS Technology for DECAL Applications

As a result of the required ultra-high granularity in a DECAL, approximately $\sim 10^{12}$ cells would be used in a detector such as the ILD. Having separate readout electronics for each pixel, as well as individual cooling and power supplies becomes impractical for such a large number of pixels and would create large dead areas for each pixel. By using MAPS, the electronics can instead be integrated into the pixels themselves, making the structure of each cell more compact and minimising the dead area for each pixel.

The schematic of a representative CMOS MAPS pixel is shown in Figure 3.3. It uses a p-type epitaxial layer, with an embedded n-type collection diode, which creates a depletion region around the n-well causing particle-induced electrons to drift toward

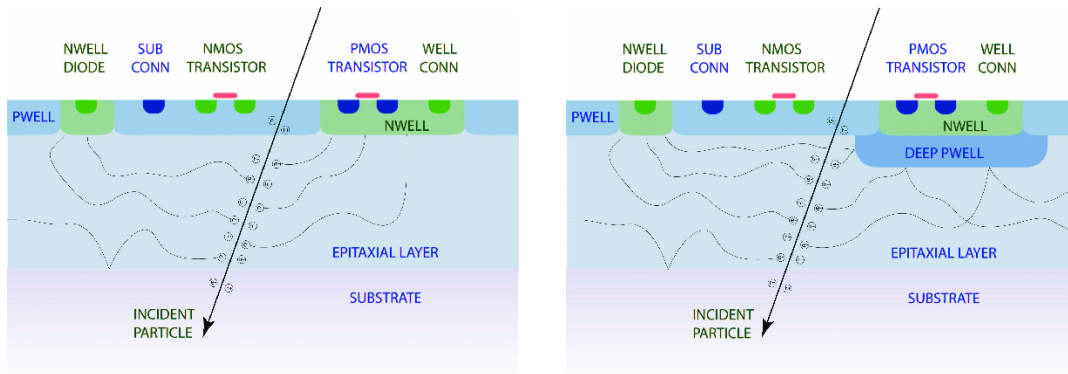


Figure 3.3: Schematic of an archetypal CMOS sensor showing the charge diffusion to the n-type diodes (left) and a likewise schematic of a CMOS sensor using the Integrated N-well Monolithic Active Pixel Sensor (INMAPS) process, with a deep p-well which repels charges. Taken from [50]

the collection diode. Electron-hole pairs generated outside the depletion region will diffuse through the epitaxial layer, until they stray sufficiently close to the depletion region of a collection diode. This can cause the sharing of charge carriers generated by one particle between several pixels.

The pixel layout in Figure 3.3 is not in fact practical, as the use of the embedded n-well required for the Positive Metal-Oxide Semiconductor (PMOS) transistor causes parasitic losses of the charges collected there. In order to combat this problem, the INMAPS process was developed by Rutherford Appleton Laboratory (RAL), in which the PMOS transistor is shielded by the addition of an embedded deep p-well, which repels signal charges, thereby mitigating signal loss [51]. A deep p-well is also used in the ALICE Pixel Detector (ALPIDE) sensor, a CMOS MAPS sensor used for the A Large Ion Collider Experiment (ALICE) Inner Tracker System (ITS) upgrade (See Section 6.1.2.)

PARTICLE DETECTORS FOR FUTURE COLLIDERS

4.1 SiD and ILD

The SiD is a general-purpose, compact, low-cost detector design utilising silicon-based tracking and calorimetry to provide high-precision measurements of physics processes at lepton colliders spanning a wide range of energies up to the TeV range, and is shown in Figure 4.1. The SiD was originally conceived as a detector for the ILC, and has since been adapted for use at the CLIC as well.

The ILD is the slightly larger alternative detector to the SiD, which is optimised for better energy and momentum resolution than the SiD so that it is more suited to operation at energies close to the TeV range. A cutaway view of the ILD detector is shown in Figure 4.2. It implements a highly granular calorimeter, with as little material between the interaction point and the calorimeter as possible. Like the SiD, the ILD was originally conceived as a detector for the ILC, and later adapted for

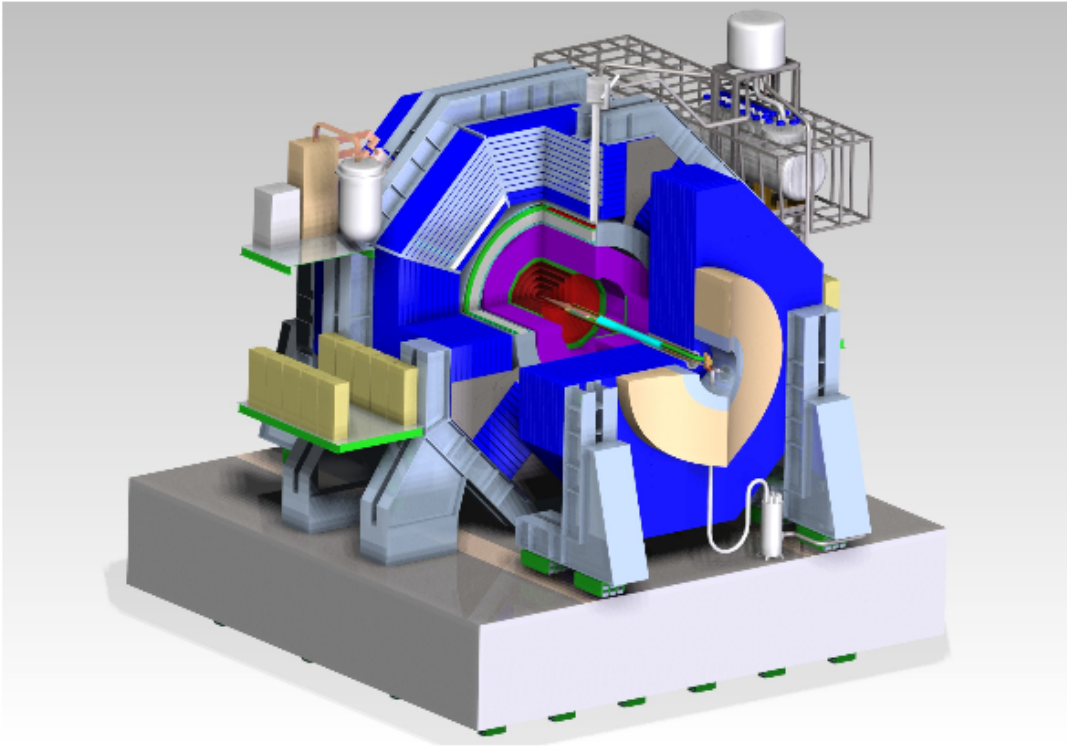


Figure 4.1: Cutaway view of the SiD detector, with the vertex and tracking in red, the ECAL in green and the HCAL in violet, with muon tracking embedded in the return yoke in blue. Taken from [52].

implementation at the CLIC [21, 52].

For the ILC, the SiD and ILD were designed to operate in a push-pull system, so that either detector could be rapidly moved into the beam line.

4.1.1 SiD Overall Design

The inner tracking systems of the SiD are split into two parts: First, the vertex detector utilises ultra-fine ($20 \times 20 \mu\text{m}^2$) silicon pixels in five layers. Second, the main tracker is a silicon strip detector, with $10 \times 10 \text{ cm}^2$ sensors able to read out a $50 \times 50 \mu\text{m}^2$ pitch, which are arranged into strip-shaped active areas.

The SiD ECAL utilises an analogue sampling calorimeter comprising of silicon active layers arranged into 13 mm^2 pixels, sandwiched between tungsten absorber layers. The ECAL uses 30 layers in total, with a combined depth of 26 radiation lengths and

one nuclear interaction length.

The HCAL for the SiD is composed of 40 layers of alternating layers of steel plate absorber layers at the ILC and tungsten at the CLIC, and glass resistive plate chambers as the active layers. It has a total depth of 4.5 nuclear interaction lengths.

The SiD also comprises two calorimeters in the forward region: the LumiCal and the BeamCal, which are ECALs designed for precise measurement and fast estimation (respectively) of the luminosity. Both are based on silicon-tungsten technology, and will require very radiation-hard sensors in order to maintain a high performance.

Lastly, the SiD detector comprises a large superconducting solenoid capable of producing a 5 T field in the inner region of the detector for use by the trackers, as well as a muon tracking system [21, 52].

4.1.2 ILD Overall Design

The ILD vertex detector is very similar to that at the SiD, comprising a system of either three pairs of silicon layers or five equidistant layers. They use highly granular pixel detectors, with pitches of $\leq 20 \times 20 \mu\text{m}^2$. The sensor technology is as yet undecided between several proposals.

A significant difference between the ILD and the SiD is the inclusion of a Time Projection Chamber (TPC) sandwiched between two small silicon trackers in contrast to the SiD main tracker. The TPC would use readout pads with a $1 \times 6 \text{ mm}^2$ pitch. The concept is that particles would pass through a sensitive gaseous volume, inducing ionisation along its track. An applied electric or magnetic field would then cause the ions and electrons to drift towards the readout pads. The 2-D position can then be read directly, and the third dimensional component inferred from the timing of the ion and electron impact. Various methods of signal amplification have been discussed for ILD [52].

A similar ECAL design to that used by the SiD is implemented in the ILD, comprising a

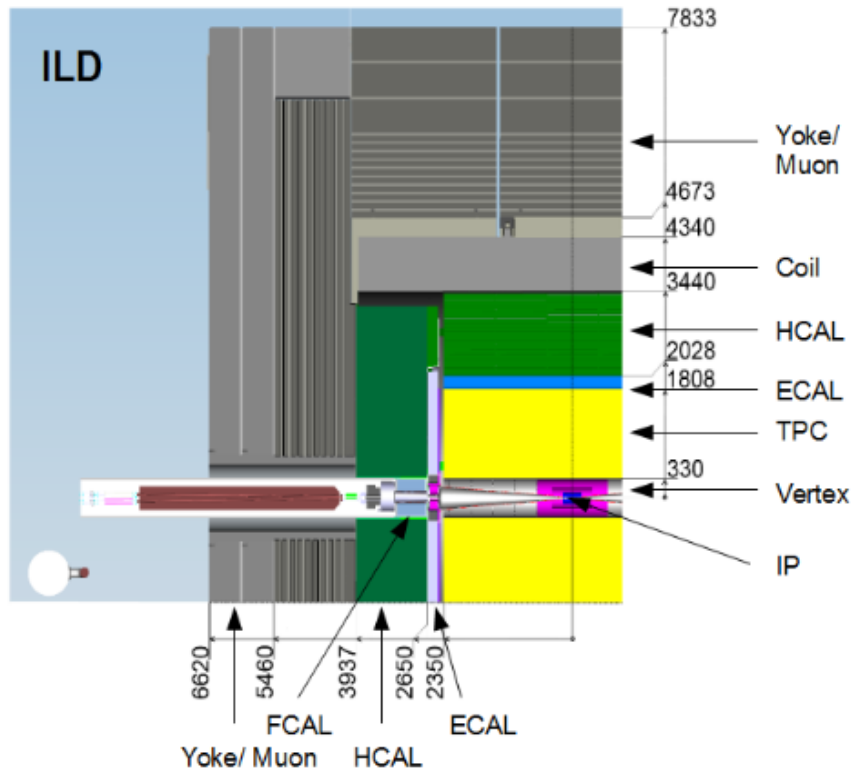


Figure 4.2: Cutaway quadrant view of the ILD detector. Taken from [52].

30 layer sampling calorimeter with tungsten as an absorber. The active layers would either be made using $5 \times 5 \text{ mm}^2$ silicon diodes or $5 \times 45 \text{ mm}^2$ scintillator strips. The ILD HCAL is also similar to its SiD counterpart, comprising 48 sampling layers with steel as the absorber material, and either scintillating layers with $3 \times 3 \text{ cm}^2$ cells or gas resistive plate chambers with $1 \times 1 \text{ cm}^2$ cells as the active layers. The ILD also includes a LumiCal and BeamCal in the forward region.

The calorimeters are followed by a large superconducting solenoid capable of producing a 3.5 T magnetic field in the trackers. Outside this, 14 layers of scintillators or resistive plate chambers are implemented as muon trackers [52].

4.1.3 SiD/ILD ECAL Design and Performance

The SiD ECAL designs for both the ILC and the CLIC are identical [21]. It comprises of silicon sensors approximately $320 \mu\text{m}$ thick, with a hexagonal pixel of size 13 mm^2 ,

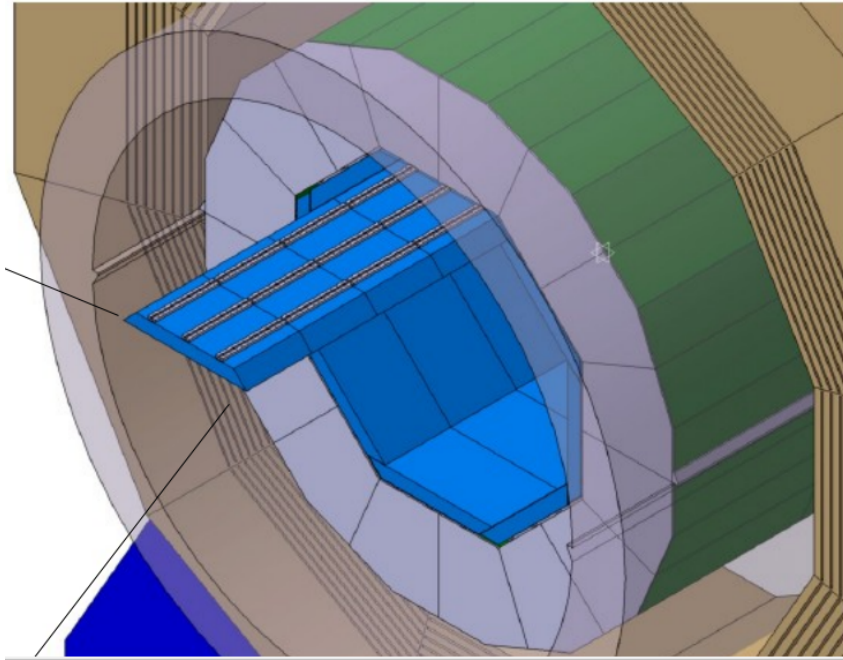


Figure 4.3: Location of the ECAL (blue) within ILD. Taken from [53].

with the option to switch to a DECAL configuration using CMOS MAPS sensors with $50 \times 50 \mu\text{m}^2$ pixels. These are embedded in 1.25 mm thick readout gaps, which are sandwiched between the absorber layers. The absorber layers are made of a 93% tungsten alloy which has a 3.9 mm radiation length. There are 30 total layers in the SiD ECAL. The first 20 layers utilise 2.50 mm thick absorber layers, while the remaining 10 outer layers utilise a 5.0 mm thick absorber, for a total of 26 radiation lengths across the entire ECAL. The depth of the ECAL in radiation lengths must remain constant in order to contain particle showers. By splitting the ECAL into an inner region with a larger sampling fraction and an outer region with a smaller sampling fraction, the core of the shower development can be determined more precisely by the inner region while outer region ‘catches’ the tail of the shower. The SiD ECAL is anticipated to achieve an energy resolution of $\sim \frac{0.17}{\sqrt{E}} \oplus 1\%$ for electrons.

The ILD’s ECAL, shown in Figure 4.3, is almost identical to that of the SiD, with the most significant difference being that the ILD uses $5 \times 5 \text{ mm}^2$ square silicon pads in the active layers rather than the hexagonal pixels of the SiD. An alternative to the purely silicon-based design would be to either partially or fully replace the silicon layers with scintillator strips with dimensions $5 \times 45 \text{ mm}^2$. By arranging scintillator

layers in alternating directions, one can achieve an effective granularity approaching that of the silicon pads. The ILD ECAL utilises only 24 radiation lengths of material, with the aim being to make the ECAL more compact. The ILD consistently achieves a jet energy resolution of less than 3% at energies greater than 100 GeV, with the performance degrading at lower energies ($\sim 3.66\%$ at 45 GeV), which roughly satisfies the nominal goal of achieving a resolution of 3.5%. Note that the jet energy resolution reflects the combined performance of the entire detector using a particle flow algorithm, rather than the ECAL alone.

4.2 CLICdet

Further design optimisation of ILD and SiD specific for CLIC has led to the CLICdet model [54, 55], which is depicted in full in Figure 4.4a. The significant changes from CLIC_ILD and CLIC_SiD include the moving of the focusing quadrupole magnets further upstream of the interaction point, leaving room for expansion of the HCAL endcaps.

4.2.1 CLICdet Overall Design

The inner tracking region mirrors the design used for SiD, but is considerably larger, particularly in the forward direction. It consists of a vertex detector made of three double-layers of silicon, consisting of $25 \times 25 \mu\text{m}^2$ pixels, with three additional ‘disks’ split into eight wedges with pixels of the same size, which are arranged in a spiral to enclose the forward regions. This is surrounded by the inner and outer tracking detectors, which are comprised largely of $50 \mu\text{m}$ wide silicon strips, which vary between 1 mm long in the innermost layer and 10 mm long in the outermost. The inner tracker comprises three double-layers in the barrel and seven endcap disks, while the outer tracker comprises three longer double-layers and four disks. The full system of vertex and tracking detectors has a half-length of 2.2 m, and an outer

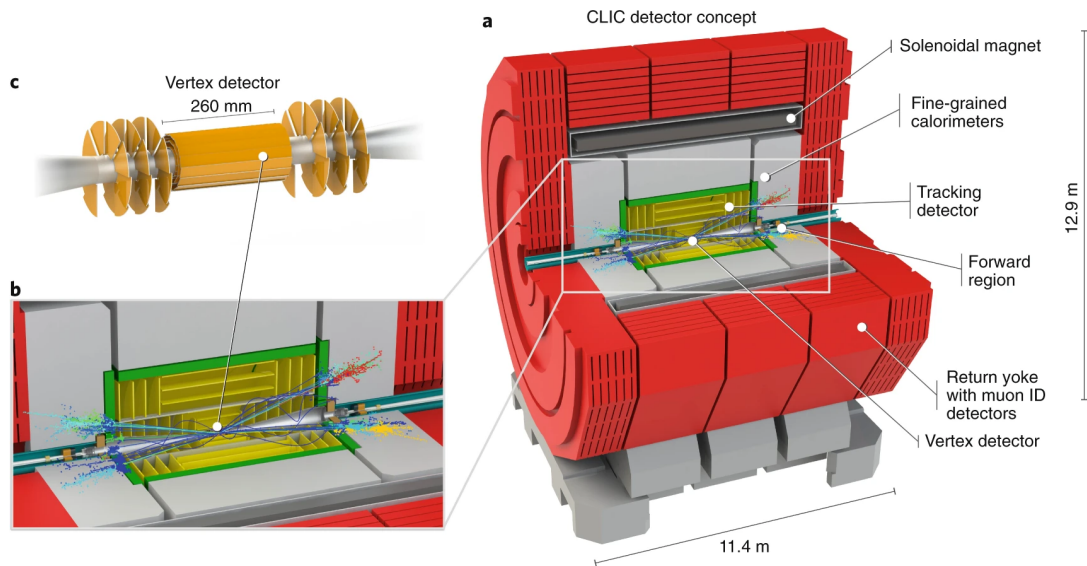


Figure 4.4: Cutaway view of CLICdet, with the vertex and tracking in yellow, the ECAL in green and the HCAL in grey, with muon tracking embedded in the return yoke in red. Taken from [56].

radius of 1.5 m.

The CLICdet ECAL is slightly more compact than that of SiD or ILD, with 40 sampling layers of silicon, 300 μm deep and segmented into $5 \times 5 \text{ mm}^2$ pads. These are sandwiched between 1.9 mm thick layers of tungsten, for a total ECAL depth of 22 radiation lengths. The additional silicon layers compared to SiD/ILD are designed to better resolve high-energy photons from the high-energy stages of the CLIC [54].

The smaller tracker radius of CLICdet compared to ILD allows additional depth between the outer bounds of the ECAL and the maximum permitted inner bounds of the solenoid, so an HCAL utilising steel as the exclusive absorber material is permitted while still maintaining the depth in interaction lengths. The CLICdet HCAL uses 60 $3 \times 3 \text{ cm}^2$ scintillator tiles, each 3 mm thick, interleaved with 20 mm thick steel plates.

The ECAL and HCAL endcaps utilise the same technology as their respective barrels. The CLICdet ECAL covers a larger forward region, with $\Delta z = 202 \text{ mm}$ compared to $\Delta z = 172 \text{ mm}/139 \text{ mm}$ for ILD/SiD respectively. The HCAL endcap has a reduced inner radius of 250 mm, improving the acceptance of the detector.

Table 4.1: Energy resolution of single photons (%) at CLICdet using the 40-layer ECAL configuration. Taken from [54]

Energy (GeV)	50	500	1500
Entire barrel	2.28 ± 0.02	0.955 ± 0.007	0.775 ± 0.006
$\theta = 90^\circ, \phi = 0^\circ$	2.11 ± 0.02	0.707 ± 0.007	0.438 ± 0.003

The magnet return yoke and embedded muon tracker system is significantly reduced in size compared to SiD/ILD, both radially and in Δz —this is an advantage made possible by the consolidation around one detector design, rather than the push-pull capability of SiD/ILD. In order to close the magnetic flux, a series of four concentric copper coils are added to the endcap region.

4.2.2 CLICdet ECAL Performance

The larger number of layers in the CLICdet ECAL compared to that of SiD/ILD increases the sampling fraction, which should produce an improvement in the energy resolution. The 40-layer ECAL was heavily optimised for high-energy single-photon energy resolution, with the final CLICdet design producing sub-3% energy resolution for photon energies > 50 GeV, as shown in Table 4.1.

The jet energy resolution of CLICdet has been demonstrated to be similar to that of SiD/ILD, with all but the smallest angles to the beam producing quark energy resolutions between 4% and 5% [25].

4.3 FCC-hh Detection

While FCC-ee could employ similar detector technologies to the SiD, ILD or CLICdet, the challenges facing detectors for a hadron collider are quite different. Significant challenges include the need to resolve particles with much higher energies and momenta, as well as coping with a much more significant background from beam interactions, while still maintaining the performance achieved for less energetic prod-

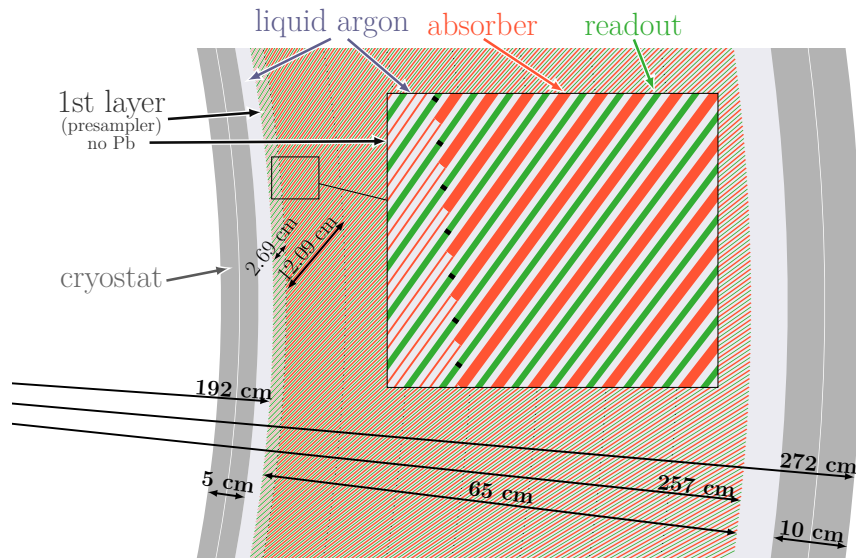


Figure 4.5: Diagram of the FCC liquid argon ECAL design. Taken from [57].

ucts. The time structure of the beams also presents a challenge, with reduced time interval between bunch crossings making cooling of the detectors more challenging.

The FCC detector technology is still at a relatively early stage in its development, and the software used to simulate its performance does not include PFA capabilities. Indeed, “full detector studies” to describe the performance of the tracker were performed in the CLIC software environment, using CLIC_SiD with the tracker replaced. As the design details and capabilities of each detector element has limited impact on the currently understood performance of the ECAL, only the ECAL is described herein.

4.3.1 The FCC-hh ECAL

The baseline FCC-hh ECAL utilises liquid argon technology rather than silicon. The principle is similar to a drift chamber, where ionisation of the argon along a particle’s path is detected by nearby plates. The design is loosely based on the ATLAS ‘accordion’ liquid argon ECAL, with layers of absorber, readout and sensitive liquid argon inclined by 50° to the radial direction (see Figure 4.5). The absorber material is a combination of lead, steel and glue, split into 2 mm thick plates.

This calorimeter has offered excellent resolution in single-electron simulations. A fit to simulations of electron energies ranging between 10 GeV and 1000 GeV (nominal FCC single particle energy range) produced an energy resolution formula of $\frac{\sigma_E}{E} = 0.15\% \oplus \frac{8.0\%}{\sqrt{E}}$. However, this performance significantly degrades with the introduction of beam-induced backgrounds particularly in the lower energy sector, and studies attempting to mitigate this are ongoing [57].

SIMULATIONS OF FULL-SCALE DECALS IN FCC-HH

5.1 Introduction

The FCC-hh project [36] is a proposed 100 km circumference synchrotron collider that aims to extend the highest energies artificially achieved in any collisions to 100 TeV, in contrast to complementary proposals to carry out experiments that are characterised by exceptionally high precision using e^+e^- collisions at any of several proposed colliders, such as the ILC, the CLIC or the FCC-ee. As a result of the complexity of hadron-hadron interactions, the FCC-hh would produce a far higher density of particles than is the case at the LHC. To meet the physics requirements, any FCC-hh detector must be able to resolve multi-TeV hadronic jets and leptons. The number of interactions per bunch crossing, or ‘pile-up,’ is expected to be $\mathcal{O}(1000)$, compared to $\mathcal{O}(200)$ for HL-LHC. Detectors for FCC-hh also require good radiation hardness and high granularity to cope with these demands.

In order to meet the detector requirements, including an ECAL energy resolution of $\frac{10\%}{\sqrt{E}} \oplus 0.7\% \oplus \frac{0.3\text{GeV}}{E}$ in the barrel region ($|\eta| < 4$), the FCC-hh reference detector was designed using a Liquid Argon (LAr) ECAL barrel (see Figure 4.5) [57], due to its intrinsic radiation hardness. It uses eight layers of sandwiched steel-plated lead absorber with liquid argon, which is read out using PCBs inclined at 50° to the radial direction, all of which is encased within an aluminium cryostat. Such an ECAL has been shown to provide a resolution of $\frac{8.2\%}{\sqrt{E}} \oplus 0.15\% \oplus \frac{0.31\text{GeV}}{E}$ for single-particle electron events, degrading to $\frac{10.0\%}{\sqrt{E}} \oplus 0.52\% \oplus \frac{1.31\text{GeV}}{E}$ for pile-up of 1000 [36, 57].

Two variants on a high-granularity ECAL are introduced as alternatives to the baseline LAr concept due to their potential to improve pile-up rejection and their application to PFAs. Here a GEANT4-based ILD-like model of both an analogue silicon ECAL and a DECAL are presented for use in FCC-hh applications, with the performance of both of these detector configurations examined using single-particle simulation studies at FCC-like energies. Using silicon as the active material and keeping the total detector depth fixed in terms of radiation lengths, the design was optimised by varying the detector geometry, absorber material and number of sampling layers, then evaluating the expected performance. The configurations using silicon as the active layer with either lead or tungsten as the absorber are referred to as SiW or SiPb, respectively.

5.2 Event Generation and Detector Simulation

The simulation model of the proposed FCC-hh DECAL was implemented in the framework of FCC Software (FCCSW) v0.9 [58], using DD4hep [59] to define the detector configuration and then converting the DD4hep geometry for use in GEANT4 v10-03-patch-01 [60]. A right-handed Cartesian coordinate system is used, with origin at the nominal beam-crossing point, \mathbf{x} horizontal and outwards of the collider ring, \mathbf{y} vertical and upwards.

The geometry of the silicon-based model in FCCSW was updated for this study.

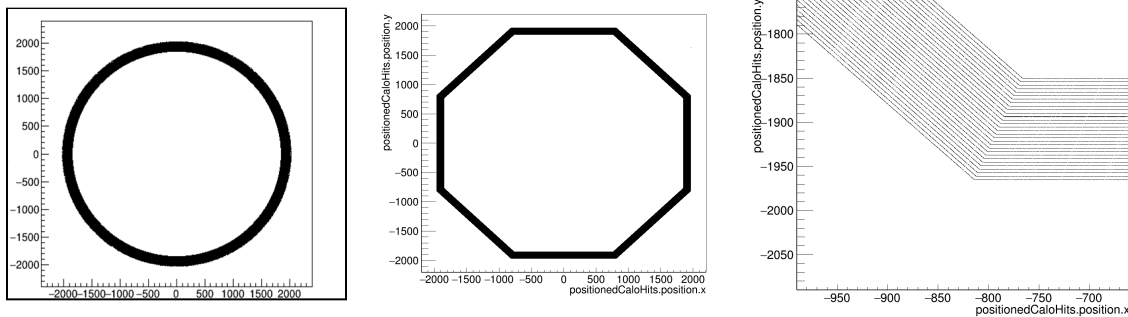


Figure 5.1: Transverse hitmaps showing the geometry configurations of the old (left) and new (centre) models of the silicon-based FCC-hh ECAL. Hitmaps were generated by simulating muons, evenly distributed across $0 \leq \phi \leq 2\pi$ using $\eta = 0$. A close-up of the boundary between two trapezoid ‘staves’ is shown (right).

Previously a simple cylindrical model of circular cross-section in the $x - z$ plane had been used. The updated model used for the geometry was an ILD-like structure, i.e. a hollow octagonal prism co-axial with the beam axis and constructed by aligning eight trapezoidal prisms. These prisms are then divided into layers, each comprising a $468 \mu\text{m}$ deep layer of silicon, and a passive absorber of varying material type and thickness. The original and revised geometries are illustrated using hitmaps in Figure 5.1 and in an isometric view in Figure 5.2.

The silicon in each layer was further divided into two layers, to allow analysis of both digital and analogue calorimeter variants from a single sample of simulated events, thus reducing the event-by-event dispersion in comparisons of analogue and digital devices. The silicon layers were split into an $18 \mu\text{m}$ thick epitaxial layer, while the remaining $450 \mu\text{m}$ of silicon would comprise the substrate layer. Here, the thin epitaxial layer represented the typical thickness that would be used in a CMOS MAPS sensor, and read out as a digital response, while the substrate layer read out an analogue response. Both layers were active and giving a readout during the simulations, such that the same set of events could be used for both analogue and digital simulations. The substrate layers were divided into $5 \times 5 \text{ mm}^2$ pads, while the pixel pitch for the epitaxial layer was set at $50 \times 50 \mu\text{m}^2$ which were grouped into $5 \times 5 \text{ mm}^2$ (100×100 pixel) pads. The passive material and thickness is varied for dedicated studies described later. Initial studies use 50 layers of alternating

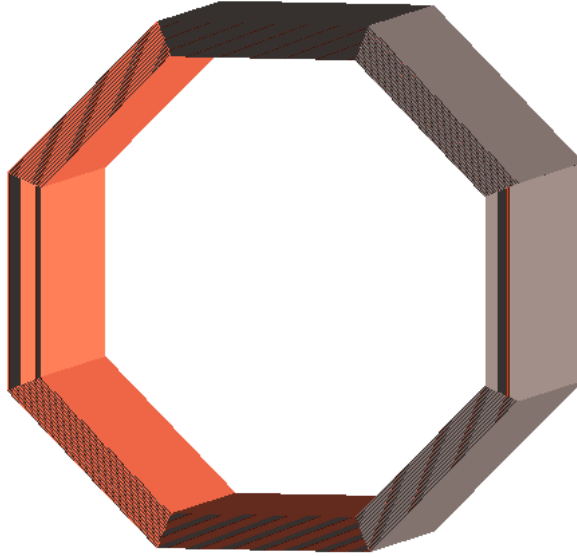


Figure 5.2: Isometric 3-D view of the FCC-hh DECAL geometry. Taken from [57].

3.4 mm-thick lead (Pb) with the silicon, such that each layer contains $0.6\chi_0$ depth of passive material, for a total ECAL depth of $30\chi_0$ (See Figure 5.4.)

With the geometry implemented in DD4hep, the GEANT4 particle gun was used to fire electrons into the calorimeter. The electrons were generated at the origin, uniformly in azimuthal angle ϕ , and with pseudorapidity restricted to $|\eta| \leq 0.001$, where the pseudorapidity is defined using the angle between a particle's trajectory and the beam pipe θ by $\eta \equiv \ln[\tan(0.5\theta)]$. The electrons were produced at a range of energies between 10 GeV and 1000 GeV, which is a typical energy range of electrons expected in FCC-hh. Samples of 5,000 events were produced at each energy. A 4 T magnetic field was introduced to the simulations, consistent with that expected for the solenoid in FCC-hh [61]. Statistically independent samples of events were produced for each of the four detector configurations considered. In total, 160,000 events were generated.

After generating the events, the hits were separated into two sets: a digital group, measuring energy deposits as digital hits in the $18 \mu\text{m}$ epitaxial layer, and an analogue group measuring analogue energy deposits in the $450 \mu\text{m}$ substrate layer.

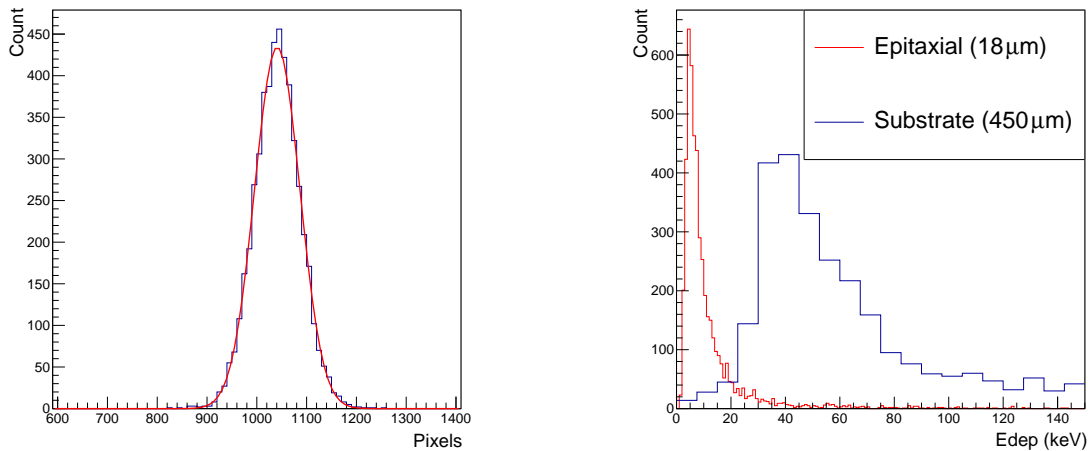


Figure 5.3: Distribution of total number of pixels above threshold in the epitaxial layer (left) and energy deposited in each pixel in the first epitaxial and substrate layer (right) for 10 GeV electrons incident on a 50-layer SiPb calorimeter.

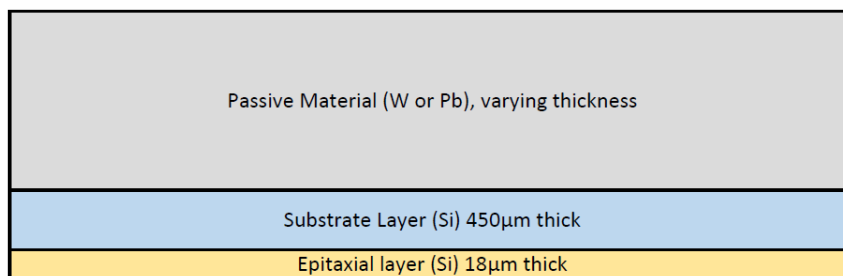


Figure 5.4: The repeating layer structure as used in the FCC-hh DECAL simulation (not to scale).

A threshold in the deposited energy equivalent to 480 electrons¹ was applied to the digital pixels before they would register a hit, while for these studies no threshold was applied to the analogue case. The analogue deposits and digital pixels were then grouped into 5×5 mm² pads.

¹This corresponds to 1/3 of the number expected for a MIP at normal incidence.

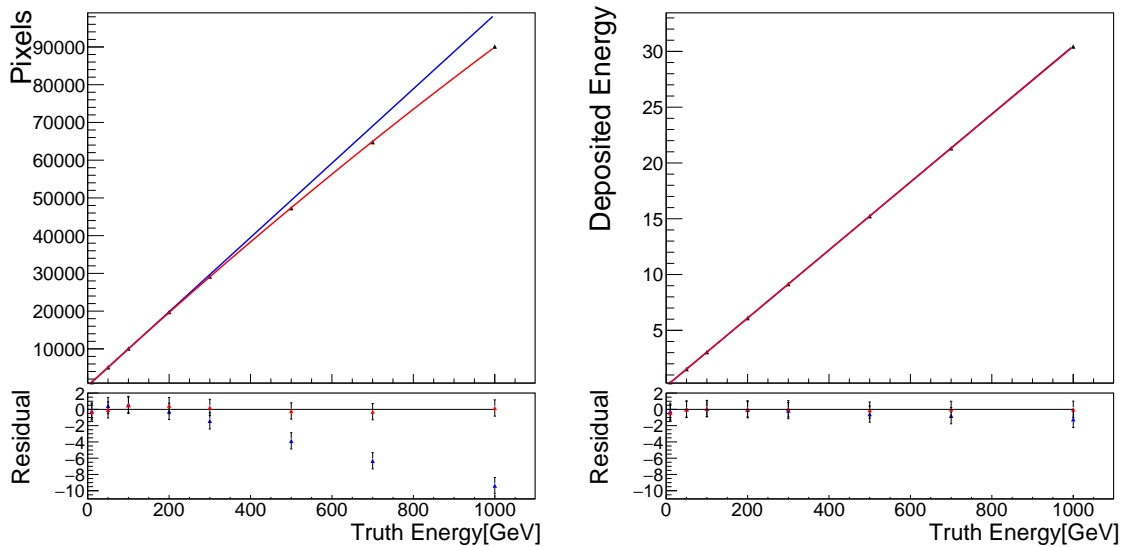


Figure 5.5: Calibration curves showing the relationship between the energy of the primary incident particle and number of pixel hits observed in the DECAL (left), and energy deposited in active layers of the analogue calorimeter (right). The results of a linear (blue) and second order polynomial (red) fit over the range 10–200 GeV are shown in both cases. Linearity of response is illustrated by normalised residuals relative to fits performed over the range 10–200 GeV.

5.3 Analogue and Digital Performance

5.3.1 Energy Reconstruction

The energy of an incident high-energy particle E is determined from the energy deposited in the active medium and the known sampling fraction. The energy deposited in a layer of the DECAL is deduced from the number of individual pixels that register a hit above the set charge threshold. It is necessary, therefore, to establish the relationship that allows E to be determined using the information provided by the detector. In simulation, E is known without uncertainty and is used for these studies. For later stages in development of detectors, the response of a physical prototype is validated using data from a so-called test beam, e.g. as described in detail in Section 6.1, where one of the challenges is establishing the actual energy of incident particles.

In the digital calorimeter, the number of pixels over threshold (digital hits) N in

an event is measured for each value of E . The distribution of the number of hits is then fitted with a Gaussian function, as shown in Figure 5.3, from which the mean number of hits μ_N and its standard deviation σ_N are extracted.

The Gaussian fits to the distributions of the number of pixel hits can be used in conjunction with the known energy E to calibrate the relationship between the ‘truth’ energy and the number of pixels over threshold, as in Figure 5.5. The form of the fitted calibration was a second order polynomial², as in Eq. 5.1,

$$N = aE^2 + bE + c \quad (5.1)$$

where E is the truth energy of the incident electron and a , b and c are simple coefficients to be determined. In an ideal DECAL the number of hits will increase linearly with E . However, at the high energies considered here, a significant contribution from saturation is expected, as discussed in Section 3.6, hence the need to allow a non-zero coefficient for the term in E^2 .

The initial particle energy E can be determined in a similar manner for the corresponding analogue silicon ECAL after calibration using the energy deposited in the active layers of the calorimeter E_{Dep} ,

$$E_{Dep} = bE + c, \quad (5.2)$$

as shown in Figure 5.5.

5.3.2 Energy Resolution

As the performance of a calorimeter is typically characterised by its resolution expressed as the ratio of the intrinsic energy resolution to the mean reconstructed energy, $\frac{\sigma_E}{\mu_E}$, this value was calculated for each calorimeter variant considered at each energy, and a function describing its behaviour constructed for each calorimeter

²This is the minimal variant from linear and a purely empirical form.

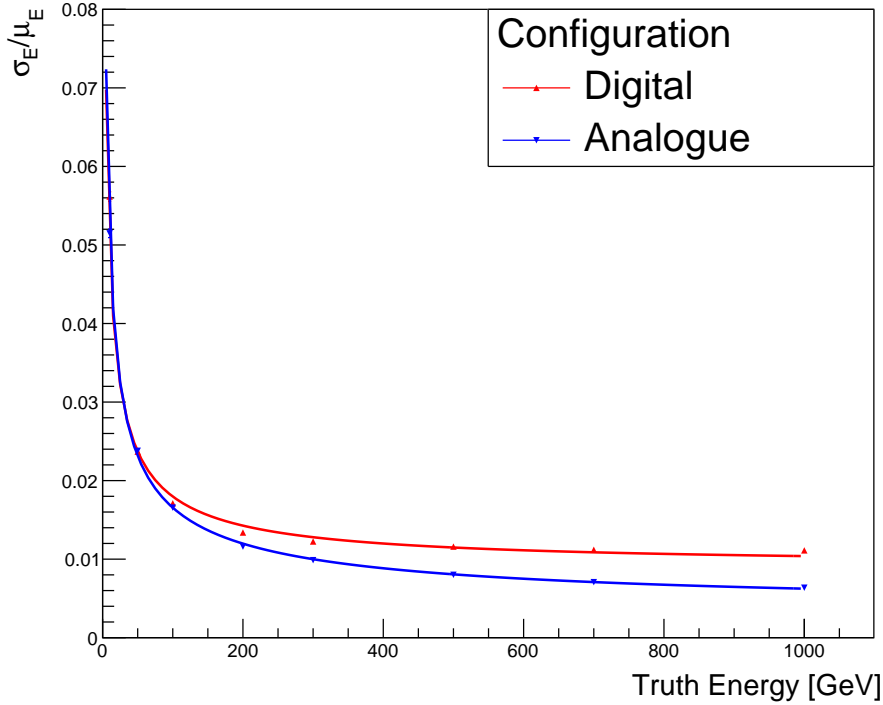


Figure 5.6: Energy resolution curve describing the variation of the energy resolution with the energy scale for the 50 Layers SiPb geometry.

layout.

After the calibration relations had been established, these were applied to the digital pixel data and the analogue energy deposition data. The mean energy μ_{EReco} and standard deviation σ_{EReco} were extracted from the reconstructed energies and used to determine $\frac{\sigma_E}{\mu_E}$. This in turn was parameterised according to Eq. 3.9 to describe the relationship between $\frac{\sigma_{EReco}}{\mu_{EReco}}$ and E_{Truth} .

When fitting the results of the simulations, the coefficient for the noise term b in Eq. 3.9 is found to be small, as expected since no additional noise was included in the simulations. In a typical analogue case one expects the stochastic term a to dominate, with a small contribution from the constant term c that becomes relatively more important with increasing energy. In the absence of noise, the resolution is expressed as:

$$\frac{\sigma_E}{E} = \frac{a}{\sqrt{E}} \oplus c. \quad (5.3)$$

This parameterisation does not fully account for the DECAL case, where one of the significant limiting factors is pixel saturation. As such, this fit is not expected to behave as well as for the analogue case in the very high energy regime where saturation may no longer be negligible.

Figure 5.6 shows the results of fitting the energy resolution in the DECAL and AECAL to Eq. 5.3. The AECAL shows an energy resolution given by:

$$\left(\frac{\sigma_E}{E}\right)_{AECAL} = \frac{16.16 \pm 0.10\%}{\sqrt{E}} \oplus (0.358 \pm 0.011\%), \quad (5.4)$$

whereas the DECAL resolution is parameterised by:

$$\left(\frac{\sigma_E}{E}\right)_{DECAL} = \frac{15.46 \pm 0.12\%}{\sqrt{E}} \oplus (0.917 \pm 0.009\%). \quad (5.5)$$

The slightly smaller value of the stochastic term in Eq. 5.5 compared to Eq. 5.4 reflects the expected improvement in resolution which is anticipated due to mitigation of Landau fluctuations in the energy deposited in each layer, as illustrated in Figure 5.3. Note that this is only the case for low energies. At energies above ≈ 300 GeV, the effect of saturation becomes more significant for the DECAL, which is reflected in a notably larger value of the constant term compared to that for the AECAL, for which saturation due to multiple particles contributing to a given read out channel is not relevant.

5.4 Passive Layer Geometry Variation

The 50 layer SiPb with $0.6\chi_0$ per layer represents close to the ideal configuration of a silicon-based ECAL within the volume limits of the FCC-hh baseline detector [57].

In the studies presented here, a comparison is made between four different detector configurations, varying the number of layers and the depth of the passive material in radiation lengths as shown in Table 5.1.

Table 5.1: Passive layer configurations used in DECAL simulations for FCC-hh

Number of Layers	Material	Thickness of Passive Layer	
		Radiation Lengths	mm
30	W	1.0 X_0	3.5
30	Pb	1.0 X_0	5.6
50	W	0.6 X_0	2.1
50	Pb	0.6 X_0	3.4

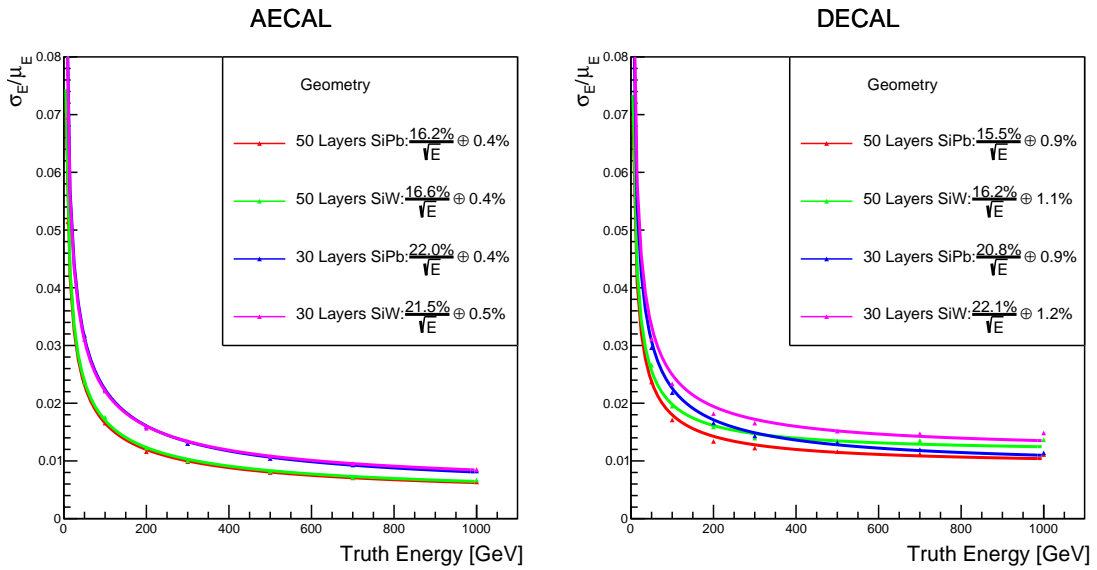


Figure 5.7: Digital and analogue energy resolution for all detector geometries, with raw data from fitted Gaussian functions as well as curves describing fits to Eq. 5.3.

The results of fitting Eq. 5.3 to analogue and digital energy resolutions are shown in the curves in Figure 5.7, as well as the values of the fits in Table 5.2.

It is clear from Figure 5.7 that the dominating geometric factor impacting the energy resolution in analogue calorimeters of this type is the number of layers. The impact of changing from a passive material with a smaller radiation length to a larger one, while keeping the total depth in terms of radiation lengths unchanged, is predominantly to increase the shower dispersion. However, in an analogue calorimeter this has little effect, as a dense shower still deposits the same amount of energy as a shower that has the same total energy but is more widely dispersed. Increasing the number of silicon layers, on the other hand, increases the number of energy depositions with which to construct an average, reducing the effect of small fluctuations affecting the average. This causes the E_{Dep} Gaussian produced to be thinner, so the

Layers, Material and Type of Calorimeter	Stochastic Term a	Constant Term c
30 SiW Analogue	$21.54 \pm 0.13\%$	$0.497 \pm 0.014\%$
30 SiW Digital	$22.09 \pm 0.16\%$	$1.156 \pm 0.013\%$
30 SiPb Analogue	$21.98 \pm 0.15\%$	$0.410 \pm 0.018\%$
30 SiPb Digital	$20.79 \pm 0.14\%$	$0.879 \pm 0.014\%$
50 SiW Analogue	$16.61 \pm 0.12\%$	$0.374 \pm 0.013\%$
50 SiW Digital	$16.22 \pm 0.17\%$	$1.135 \pm 0.011\%$
50 SiPb Analogue	$16.16 \pm 0.10\%$	$0.358 \pm 0.011\%$
50 SiPb Digital	$15.46 \pm 0.12\%$	$0.917 \pm 0.009\%$

Table 5.2: Energy resolution fit parameters for all calorimeter configurations.

energy resolution is improved.

At low energies, the DECAL fit results in Figure 5.7 appear similar to those in the analogue case; increasing the number of layers increases the ratio of pixel hits to truth energy, increasing the effective sampling fraction, while changing the passive material has little effect. However, at higher energies the digital fits deviate from this pattern, with the material used in the calorimeter having a significant effect on the resolution. The dominant effect that separates digital and analogue calorimeter performances is the saturation of DECALS at high energies. The effect of using a passive absorber with a longer radiation length would be to increase the distance between each layer of active silicon, assuming a constant separation in terms of radiation lengths. This would decrease the density of the produced shower. More dense showers cause a greater level of saturation in a digital calorimeter, and as such at higher energies those geometries with lead as the passive material experience lower levels of saturation and as such a better performance than those with tungsten as the passive material. However, saturation is not so dominant an effect that it eliminates the impact of the number of layers on the resolution, which is shown by the improved performance of the 50 layer geometries when compared with its 30 layer material counterpart across the full range of energies.

5.5 Future Developments

The resolution of a DECAL for FCC-hh is profoundly affected by the effect of saturation, so it is necessary to consider how this effect may be diminished. A possible solution presents itself as a compromise between the advantages of a digital and analogue calorimeter in the semi-digital calorimeter, with several thresholds for counting more than one particle per pixel. This would allow more power for distinguishing pixels through which several particles have passed. The more thresholds, the more power for reducing saturation. However, this would require increasingly more complicated pixel design and also a greater data volume. One could also mitigate the effects of saturation by decreasing the size of the pixels themselves, though this solution also results in an increased data volume. Decreased pixel size also exacerbates ambiguity due to particles crossing over the boundaries between pixels, as well as increasing the relative effect of electronic noise in the pixels [62].

It is necessary to consider that the studies presented here represent a study of the ECAL alone, in an optimal scenario. These studies have considered only particles with an initial direction of travel at 90° to the ECAL surface. Entering the detector at other angles will increase the distance of material the particle traverses through both active and passive absorber layers, effectively increasing the depth in radiation lengths the particle travels through in each layer and leading to miscounting of the number of particles passing through the ECAL. This effect is less significant for analogue detectors, since they measure the energy deposited in each hit and scale it with a sampling fraction which is largely unaffected by the angle of entry. Other effects that can affect performance within a magnetic field at an angle include the potential for very low-momentum particles to become trapped within a passive layer, and not deposit enough hits, or from particles being curved back into layers they have already crossed, thereby causing an over-recording of hits. Particles produced in collisions may be produced in a wide variety of directions, so further study is necessary to consider the angular dependence of the detector performance, particularly since high momentum particles in this study will not have deviated significantly

from their initial trajectory perpendicular to the surface.

Any ECAL design for future colliders will be required to detect more than single particles—particle collisions at FCC-hh energies will produce a multitude of showers, as well as resolution losses from effects such as bremsstrahlung. The longer term aim should be to examine the capabilities of the ECAL when combined with other detector elements, such as a tracker or HCAL, in a full PFA in order to assist in identifying individual collision products.

5.6 Conclusions

The potential for implementing a silicon-based DECAL with ILD-like geometry in the FCC-hh software framework has been examined by studying the single particle energy resolution for various materials and configurations. Studies were performed by measuring energy deposits within the calorimeter as determined by GEANT4 software. This allowed the main factors affecting the energy resolution of each geometry to be identified.

In the analogue ECAL, the number of layers is the strongest factor affecting performance, with more layers giving an improved resolution. As one would expect, the passive material used appears to have little effect on the resolution, and so tungsten is the better choice having a shorter radiation length than lead and thereby requiring a shorter distance to achieve an almost identical performance. It also has a smaller Molière radius and can be mechanically self-supporting.

In the DECAL, the material choice plays a more vital role. At lower energies, where there is little saturation, the number of layers is the most significant factor affecting resolution. However at higher energies, using lead instead of tungsten becomes the more important factor. As lead has a larger Molière radius than tungsten, thicker passive layers are required to fully contain the electromagnetic shower. This allows a greater spread of the shower and so reduces saturation, although it also results in

a deeper ECAL. The number of layers still plays a small role at higher energies, and using 50 layers with $0.6X_0$ of passive lead in each layer yields consistently better resolution than the other configurations.

Using the 50 layers SiPb configuration, which gave the best performance in both the digital and analogue case, the energy resolution for the analogue ECAL is found to be:

$$\frac{\sigma_E}{E} = \frac{16.2\%}{\sqrt{E}} \oplus 0.4\%. \quad (5.6)$$

The energy resolution for the DECAL using the same configuration is found to be:

$$\frac{\sigma_E}{E} = \frac{15.5\%}{\sqrt{E}} \oplus 0.9\%. \quad (5.7)$$

While the stochastic term is generally considered the figure of merit in an analogue sampling ECAL, since the parameterisation described by Eq. 5.3 does not physically represent the DECAL as can be seen in Figure 5.7, it is necessary to consider the raw resolution as the true figure of merit for these calorimeters. We compare the energy resolution at a representative range of the truth energies investigated above in Table 5.3, and find that at lower energies the DECAL performs comparably with the analogue ECAL, but at the higher energies expected at the FCC, saturation in the DECAL degrades its performance and the analogue ECAL has an improved resolution.

It should be remembered when comparing these resolutions that while the digital

Calorimeter	50 GeV	300 GeV	500 GeV	1000 GeV
50 SiPb Analogue	2.379±0.023%	0.987±0.010%	0.801±0.009%	0.636±0.007%
50 SiPb Digital	2.368±0.024%	1.225±0.013%	1.160±0.013%	1.111±0.013%
50 SiW Analogue	2.363±0.024%	1.003±0.011%	0.821±0.010%	0.669±0.007%
50 SiW Digital	2.659±0.028%	1.396±0.014%	1.345±0.015%	1.367±0.017%
30 SiPb Analogue	3.178±0.033%	1.300±0.013%	1.042±0.012%	0.826±0.009%
30 SiPb Digital	2.962±0.030%	1.434±0.015%	1.316±0.014%	1.141±0.013%
30 SiW Analogue	3.106±0.030%	1.339±0.015%	1.079±0.012%	0.853±0.010%
30 SiW Digital	3.112±0.032%	1.656±0.018%	1.516±0.016%	1.485±0.017%

Table 5.3: Raw energy resolution values for all ECAL configurations.

simulations include a threshold of 480 electrons for each pixel, no such threshold is applied in the analogue case. These results should therefore be viewed as a best-case scenario for the analogue ECAL. The application of a threshold in the analogue case is likely to degrade the resolution by removing lower-energy hits. For any application of these studies it should also be considered that the cost of an analogue calorimeter using hybrid sensors is likely to be greater than that of a CMOS MAPS based DECAL, and so a cost-benefit analysis is required to optimise the choice of detector.

EPICAL2 TEST BEAM STUDIES

6.1 Introduction

This chapter summarises state-of-the-art DECAL developments using EPICAL-2, a compact 24-layer sampling calorimeter prototype instrumented using ALPIDE sensors [63–65], as part of R&D for an upgrade of the ALICE Forward Calorimeter (FOCAL).

6.1.1 EPICAL1 MIMOSA Prototype

Prior to the beginning of R&D toward a DECAL in the context of ALICE, test-beam studies using the DECAL concept had been performed using stacks of up to six TeraPixel Active Calorimeter (TPAC) sensors [66]. The first of the ALICE FOCAL prototypes built on this work with a full MAPS-based prototype was called Epitaxial Calorimeter 1 (EPICAL-1) and used MIMOSA23 [67] sensors.

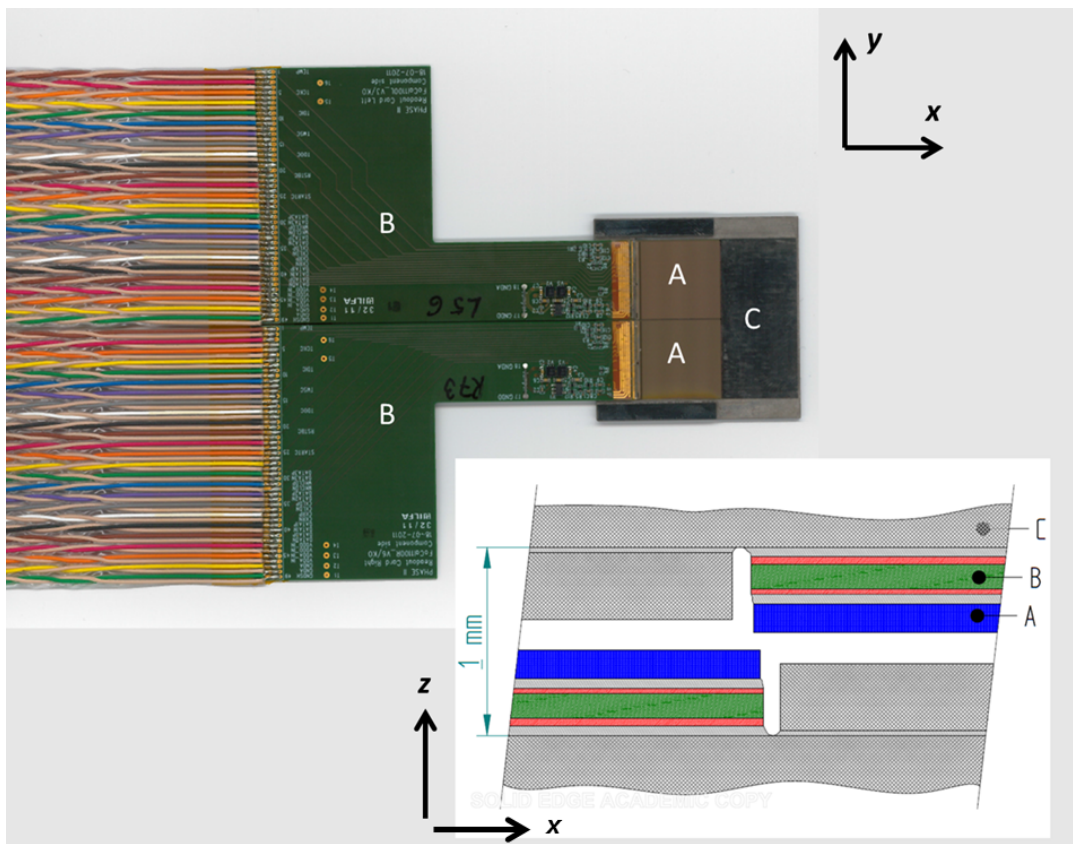


Figure 6.1: *Upper left*: Plan view of an individual EPICAL-1 module, showing: the two sensors *A*; readout Printed Circuit Board (PCB)s *B*; and tungsten *C*. *Lower right*: Schematic cross-section of a single EPICAL-1 layer showing the overlap between the two modules and the additional tungsten added next to each module (bottom right). Taken from [67].

The EPICAL-1 consisted of 24 layers, each comprising two modules with two sensors (total of 4 sensors per layer), as well as 3 mm thickness of tungsten. The two modules in a given layer were arranged with one inverted relative to the other with a small overlap, such that the only insensitive area was the gap between sensors in the same module, as shown in Figure 6.1. This also meant that the cables for modules in the same layer extend in different directions, allowing a compact prototype. To maximise the amount of passive material while minimising total depth per layer, an additional 0.3 mm of tungsten plate was glued next to each module. The total active area in each layer was $4 \times 4 \text{ mm}^2$, while the total area of tungsten was $5 \times 5 \text{ mm}^2$ [67].

The EPICAL-1 prototype was tested at DESY and CERN SPS using electron/positron beams of energies between 2 GeV and 244 GeV. Although the 640 μs integration time of MIMOSA23 limited the event rate and precluded its use in the ALICE FOCAL, it was a very important step in demonstrating the feasibility of the DECAL concept. Using 2–5 GeV e^+/e^- data, the resolution of EPICAL-1 was found to be:

$$\frac{\sigma}{E} = \frac{30 \pm 4\%}{\sqrt{E}} \oplus \frac{6.3\%}{E} \oplus (2.8 \pm 1.7\%). \quad (6.1)$$

Simulations of the prototype using GEANT4 (v10-00-patch-01), including modelling of dead pixels and inoperative sensors, showed a better resolution of

$$\frac{\sigma}{E} = \frac{28 \pm 4\%}{\sqrt{E}} \oplus (2.5 \pm 1.7\%). \quad (6.2)$$

This small discrepancy in resolution curves was compounded by apparent differences in the size of clusters of pixel hits and in the position resolution.

One additional challenge in interpreting the EPICAL-1 was that the number of sensors and thickness of tungsten a shower particle would pass through in a single layer varied with the position in the $x - y$ plane. From Figure 6.1 it can be seen that a particle travelling in the z direction might pass through either a single sensor and 3 mm tungsten, a single sensor and 2.7 mm tungsten, or two sensors and 2.7 mm of tungsten. While overall this effect can be accounted for by calibrating the linearity

curve of the prototype, it has the effect of smearing the response, thereby degrading the resolution.

The next phase of DECAL development is based on the more recently developed ALPIDE sensor, as discussed below.

6.1.2 ALPIDE Digital Sensors

The ALPIDE chip is a CMOS MAPS sensor developed for use in the ALICE ITS upgrade. It comprises a 512×1024 matrix of $29.24 \times 26.88 \mu\text{m}^2$ digital pixels, forming a sensitive area of $\sim 15 \times 30 \text{ mm}^2$.

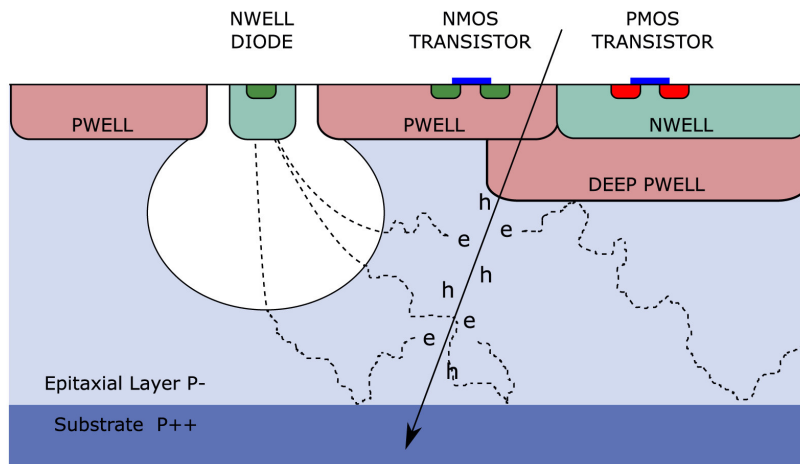


Figure 6.2: An ALPIDE sensor showing the charge diffusion to the n-type diode, as well as the deep p-well and embedded n-well with PMOS transistor. Taken from [65].

Figure 6.2 illustrates the layout of a single ALPIDE pixel, which is qualitatively very similar to that developed for INMAPS discussed in Section 3.8. Alternative configurations of the sensor exist, with the epitaxial layer between $18 \mu\text{m}$ and $30 \mu\text{m}$ thick and the substrate either $50 \mu\text{m}$ or $100 \mu\text{m}$ thick.

Figure 6.3 shows the in-pixel circuitry, including the input stage, analogue front-end, and digital section. Within the input stage is the collection diode (the n-well diode in Figure 6.2), a continuous reset as well as a pulse injector, which is used for the injection of test charges. The potential drop from the input stage is then amplified

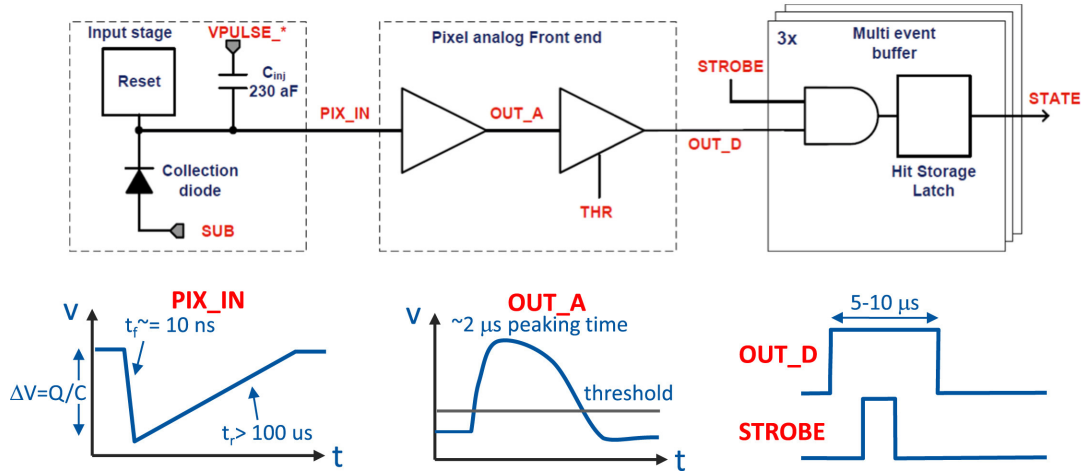


Figure 6.3: In-pixel circuitry in the ALPIDE sensor (top), as well as representative signal shapes at various stages in the circuitry (right). Taken from [63].

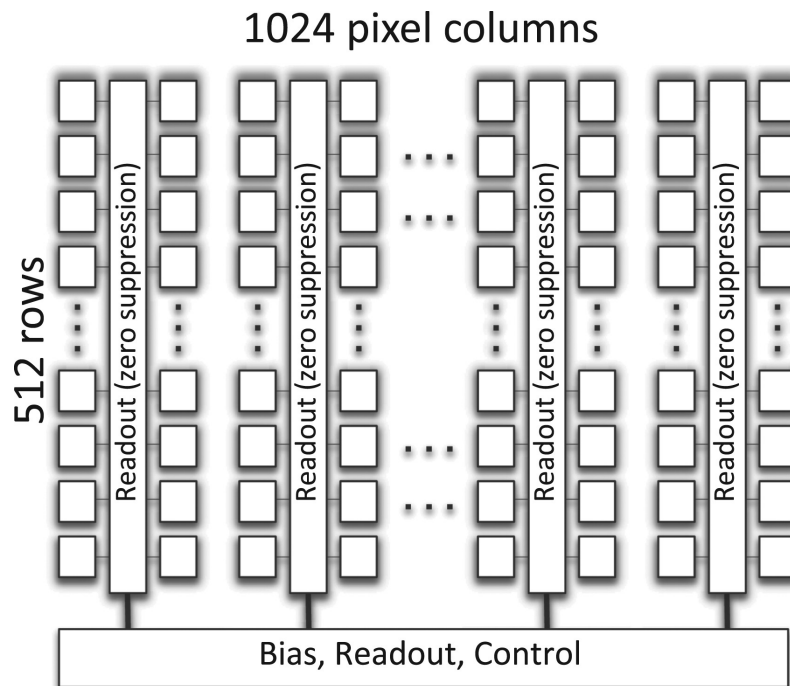


Figure 6.4: The double-column readout of an ALPIDE sensor. Taken from [63].

and shaped into a signal, with a $\approx 2\mu\text{s}$ peak time, and $\approx 10\mu\text{s}$ time to return to the baseline. This signal shaping is controlled by a variety of in-chip parameters. While the signal exceeds the threshold, the discriminator output is maintained. If this output overlaps with the strobe signal, a digital hit is registered in the state register. Each pixel contains three state registers, which act as a multi-event buffer. The hit storage latch allows for the masking of noisy pixels.

Pixels are read out in double-columns, as shown in Figure 6.4. A single common threshold is applied across all pixels in a single sensor. A reverse bias can be applied to the substrate to increase the depletion volume, at the expense of the diode capacitance.

The ALPIDE sensor has the significant advantage of a much faster readout rate (~ 100 kHz for Pb-Pb collisions [64]) than MIMOSA23 and so it is a capable successor to the MIMOSA23 for FOCAL prototyping. As it was designed with the ALICE ITS in mind, ALPIDE is also an ideal candidate for ALICE FOCAL as it is sufficiently granular for application in a DECAL while also providing the benefit of increased technological uniformity across the ALICE detector.

6.1.3 EPICAL2 ALPIDE Prototype

The EPICAL-2 prototype was developed as the successor to EPICAL-1, using the newly developed ALPIDE chip. Its primary purpose was to evaluate the ALPIDE for use in the DECAL proposition for ALICE FOCAL. However, it is also an important step for consideration of DECALs at any future collider, since it is the first proof-of-principle prototype of its type using what is effectively a fully functional sensor developed for a different purpose (in this case, tracking). It is indicative of the future feasibility of digital calorimetry.

Each layer in EPICAL-2 contains two adjacent ALPIDE chips with rotational symmetry, glued to a 3 mm thick tungsten absorber plate, of area 40×40 mm². The ALPIDEs used had a ≈ 30 μm thick epitaxial layer, with a substrate of ≈ 50 μm

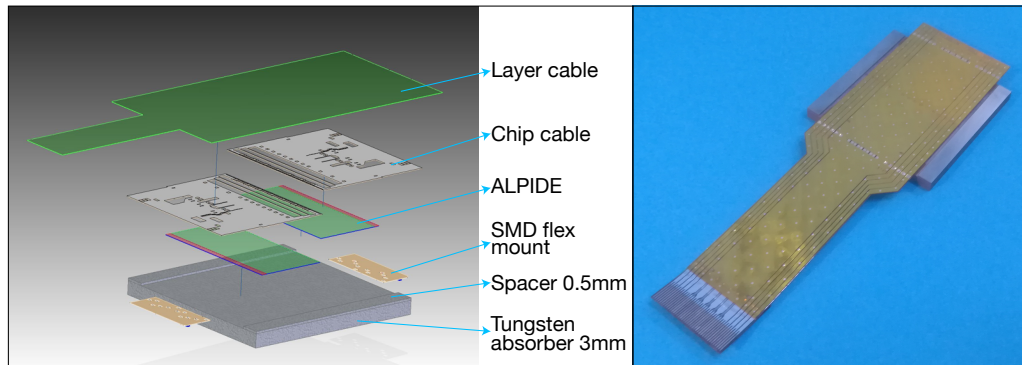


Figure 6.5: Exploded schematic of a single EPICAL-2 layer (left), and picture of a single constructed EPICAL-2 layer (right.)

thick. There is minimal separation between the two long edges of the chips, so there is a $\approx 100 \mu\text{m}$ gap between the two sensors. Each chip is Tape-Automated Bonding (TAB) bonded onto separate chip cabling, before both are bonded to flex cables, which protrude out one side of the layer. Two additional tungsten plates were placed either side of the layer to provide structural support and assist in shower containment. A schematic of a single EPICAL-2 layer is shown in Figure 6.5. Each layer was a total of 3.5 mm thick.

EPICAL-2 underwent two developmental stages. The first ‘half-prototype’ comprised 12 layers ($\approx 10.3 \chi_0$), while the full EPICAL-2 prototype consisted of 24 layers ($\approx 20.6 \chi_0$.) The prototype was housed within an aluminium frame. The half-prototype utilised air-cooling only, whereas the full prototype introduced a water-cooling system to control and maintain a stable temperature during running.

The trigger system for EPICAL-2 uses the CLAWS scintillator module, developed for SuperKEKB/Belle II, which is shown in Figure 6.6 [68]. Each module consists of a $3 \text{ cm} \times 3 \text{ cm} \times 3 \text{ mm}$ BC240 plastic scintillator tile, which is read out by a Multi-Pixel Photon Counter (MPPC) placed in a dimple in the plastic. The MPPC is surface-mounted to a PCB which provides mechanical support to the tile. The tile is covered in reflective foil to improve light yield, and the whole module is covered by opaque black tape.

During data-taking, up to three CLAWS modules were used to trigger the readout in

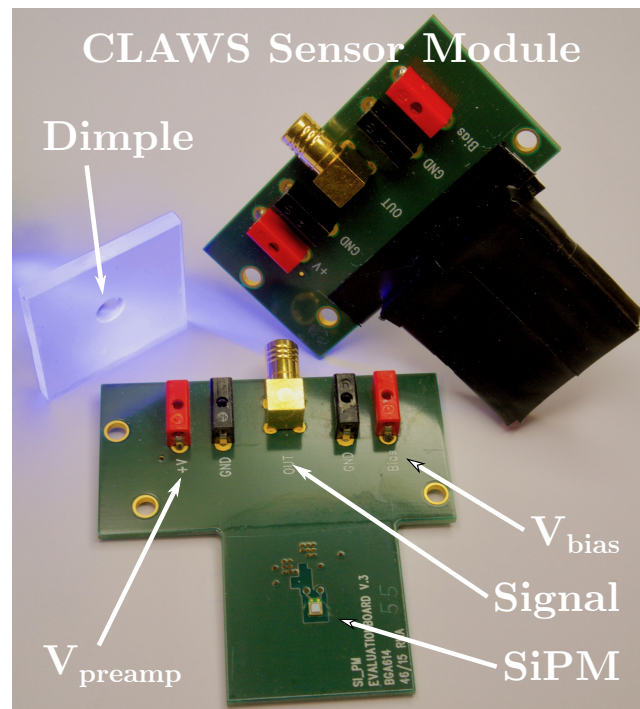


Figure 6.6: Photograph of the CLAWS scintillator module, with the components labelled. Taken from [68]

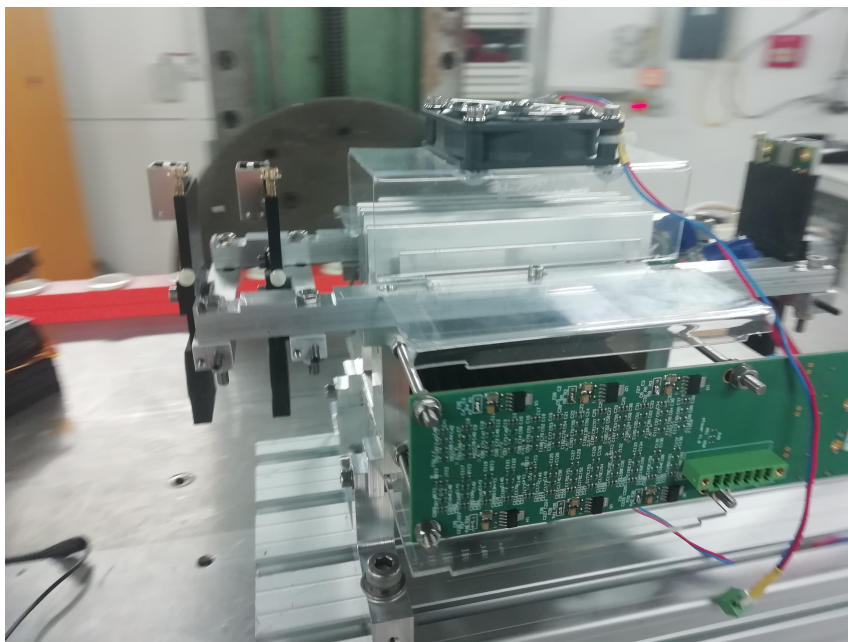


Figure 6.7: View of the EPICAL-2 prototype, set up for data-taking during February 2020 at DESY II test beam TB22, with the sCintillating Light And Waveform Sensors (CLAWS) scintillator triggers in black on the left and right.

the ALPIDEs in the EPICAL-2 prototype, as seen in Figure 6.7: two at 35 mm and 70 mm upstream of Layer 0, with the third downstream of the prototype and used during data taking of cosmic muons.

6.2 Simulations

One of the major reasons for the construction of EPICAL-2 was to examine any discrepancies between Monte Carlo simulations of events in DECAL prototypes and the data received from test beams of the same prototypes, as was done for EPICAL-1. Small discrepancies in the resolution had been found for the EPICAL-1 prototype, but well within estimated uncertainties (see Section 6.1.1.) Simulations of EPICAL-2 took place in the Allpix² framework [69], and were used to evaluate the efficacy of Allpix² at recreating low-energy leptonic events in a DECAL. Once a good understanding of the consistency between experimental data and simulations was established, Allpix² simulations were further investigated to provide additional insight into detailed features of EPICAL-2 such as the forward-backward asymmetry (see Section 6.9.) The validated simulation model can then be used with confidence to predict the behaviour in other scenarios considered.

6.2.1 Allpix Squared

Allpix² is a lightweight software framework written in C++ and designed for Monte Carlo simulation of silicon-based detectors. It contains a modular framework, where the core framework is independent of any physics implementation, so that different physics models can be imported and implemented in individual modules.

The structure of Allpix² is depicted in Figure 6.8. The central framework uses four core elements that are common to all modules: the module instantiation logic, the detector geometries, the messaging system, and the user interface.

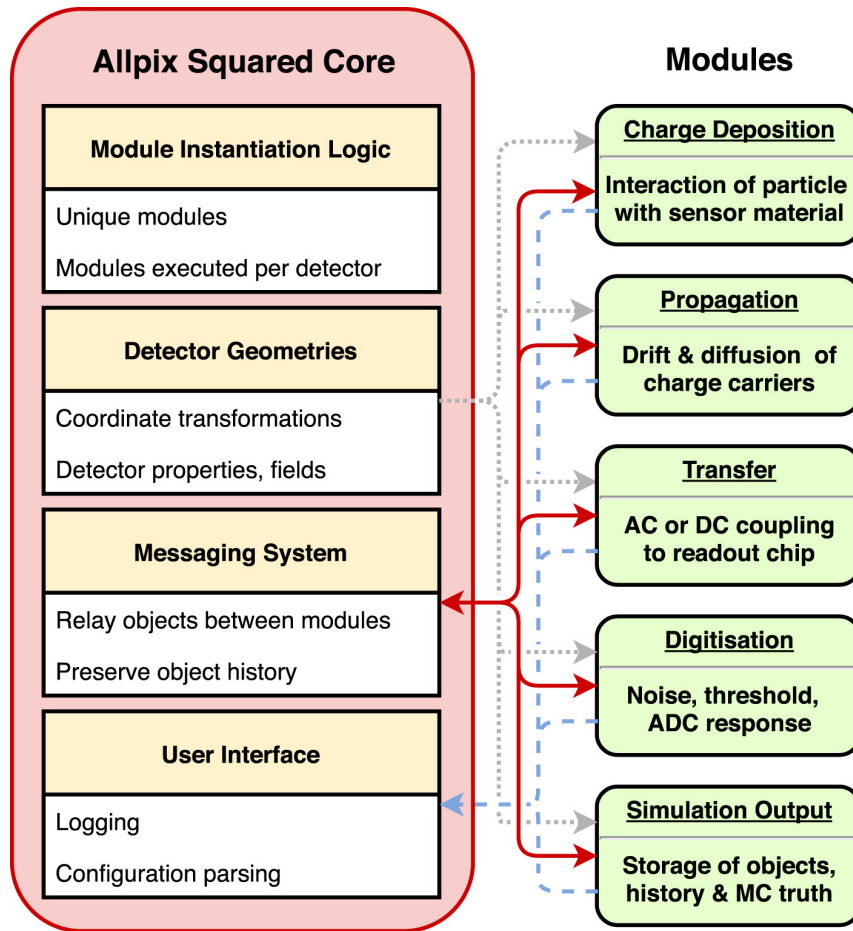


Figure 6.8: Structure of the Allpix² framework. The primary structure (left) contains the central structure as well as general utilities, while the operations (and their order) is implemented in modules (right.) Taken from [69].

The module instantiation provides a framework for two variations of module: unique modules, which are processes performed once across the entire detector geometry such as propagation of shower particles through the detector, and detector modules which perform processes on a per-sensor basis such as propagation of charge carriers within a sensor. The module instantiation logic is governed directly by a standalone configuration file provided by the user, which controls the instantiation of each module and directs each instance of a detector module to the relevant sensor.

The detector geometry framework provides flexible descriptions for hybrid and monolithic pixel detectors. The framework supports the addition of a flexible number of passive sections of geometry, which can represent absorber material, support structures, PCBs or cabling. In addition, the geometry framework supports the applica-

tion of electric fields to sensitive regions of the detector. Allpix² does not support geometries for non-semiconductor detectors, nor does it support simulation of entirely passive geometries. The geometry instantiation is driven by a configuration file provided by the user, which may be standalone or may import sub-files to configure individual sensors. Passive regions are defined by the material, which is commonly drawn from the GEANT4 material lists, as well as the size of the region and position of the centre of mass. Active regions (in the monolithic case) are defined using the number of pixels, pixel size, size of the collection diode, thickness of the active medium, thickness of the inactive silicon (the volume of silicon which contains the on-chip circuitry, which does not contribute to the signal), and the position and orientation of the sensor.

The messaging system provides the basis for exchange of information between modules. Each module accepts a particular set of messages at startup, and outputs a set of messages upon completion. Each set of messages holds a set of objects which represent the results of the module applied. Each object contains a record of the object history, e.g. an object representing a charge carrier deposited in a medium would hold a pointer to the energy deposition object which the charge carrier was derived from, and the shower particle object which deposited the energy. In this way, the messaging system allows the user to extract from a pixel hit object in the output module the Monte Carlo shower particles which resulted in that pixel hit.

The user interface provides ease of use, by converting common physical units in the configuration files for module and geometry instantiation into the units used internally by the software.

6.2.2 Event Generation and Prototype Simulation

For the simulation of the EPICAL-2 prototype, all simulation steps were performed in the Allpix² framework. The modules used in the simulation, their function and any parameters used, are listed below:

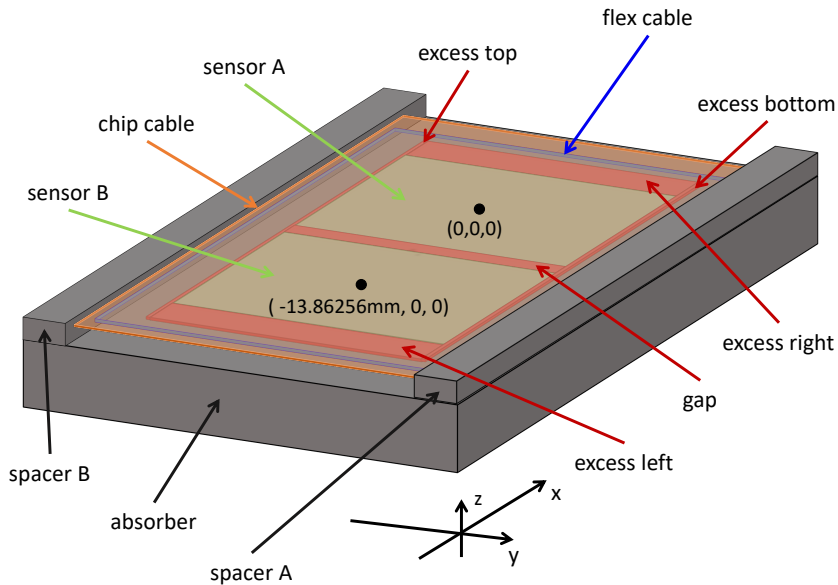


Figure 6.9: Schematic of a single layer of EPICAL-2 geometry as implemented in Allpix² in the ‘GeometryBuilderGeant4’ module. Taken from [70]

GeometryBuilderGeant4 Constructs the geometry of the EPICAL-2 prototype.

Figure 6.9 shows the construction of a single layer in Allpix². The two ALPIDE sensors have a $50 \mu\text{m}$ thick sensitive volume of silicon, each being a 512×1024 matrix of $29.24 \times 26.88 \mu\text{m}^2$ digital pixels. Each pixel has an embedded $3 \times 3 \mu\text{m}^2$ diode. Above each ALPIDE sensor there is an additional $5 \mu\text{m}$ thick passive volume of inactive silicon, which represents the in-pixel circuitry. The sensors are separated by a $100 \mu\text{m}$ wide gap of inactive silicon. Excess inactive silicon representing the peripheral cabling and guard ring is added: $1208 \mu\text{m}$ to the left and right, and $30 \mu\text{m}$ to the top and bottom, all $55 \mu\text{m}$ thick so as to achieve the same thickness as the ALPIDE sensors. The silicon is preceded by chip cables, represented by a sheet of Aluminium $30 \mu\text{m}$ thick and a sheet of kapton $30 \mu\text{m}$ thick, which are then preceded by flex cables, represented by a $145 \mu\text{m}$ thick sheet of kapton. Behind the sensors is a $35 \times 40 \times 3 \text{ mm}^3$ block of tungsten used as the absorber volume. The flex cable, chip cable, ALPIDEs and inactive silicon are housed between two tungsten spacers to the top and bottom, each of which is 0.5 mm thick and 4 mm wide, such that the total depth of one layer is 3.5 mm . There are small gaps between the flex cable,

chip cable, silicon and tungsten absorber, which are filled with air [70].

DepositionGeant4 Simulates the generation of initial particles, their development into electromagnetic showers, and the deposition of charge carriers in the active regions of the detector geometry. This module acts as a wrapper around GEANT4, which does the majority of the work in simulating the shower developed with a defined physics list. EPICAL-2 simulations use the FTFP_BERT_EMZ list (the most appropriate of the physics models recommended by GEANT4 developers for use in HEP to the electron energies simulated.)

ElectricFieldReader This module defines the electric field applied to the pixels in each sensor and is imported from an Allpix Squared Field (APF) file by the user. The electric field used in the simulations of EPICAL-2 was obtained from Technology Computer-Aided Design (TCAD) simulations of ALPIDE pixels with a total reverse bias voltage $V_{RB} = 1.4$ V, corresponding to the sum of the pixel reset voltage $V_{RST} = 1.4$ V and the reverse substrate bias voltage $V_{BB} = 0$ V, which is compatible with the bias voltage applied during data taking.

GenericPropagation Simulates the propagation of charge carriers objects created by DepositionGeant4 in the electric field applied by ElectricFieldReader. Liberated charges are grouped into batches of up to 50 in order to save processing time. It was shown that this grouping does not significantly impact the analysis results from simulations of EPICAL-2. Charge propagation is simulated over a $t_{int} = 25$ ns period before the processor terminates. This value was not known from the ALPIDEs themselves, but was instead form-fitted to the results obtained from 5 GeV data. The temperature used for the simulations was set to 293 K.

SimpleTransfer Performs the collection of charge carriers at collection diodes after propagation within the silicon. A simple direct-mapping is performed to the nearest pixel, provided that the charge carrier group is both within $5 \mu\text{m}$ of the sensor surface and within the size of the implant in the pixel. The implant

size is defined in the detector geometry, and was $3 \times 3 \mu\text{m}^2$.

DefaultDigitizer This is the only detector module used in the EPICAL-2 simulations. It performs the digitisation of collected charge from the SimpleTransfer module. A Gaussian noise contribution is added to the collected charge, with a standard deviation of $20e$. The charge in each pixel is then evaluated against the user-defined threshold value, which was set to $82e$. Threshold smearing was applied via a Gaussian with $20e$ standard deviation.

CaloOutputWriter This module is used as an interface with ROOT [71] to output the simulation results in a format readable without the use of Allpix². Pixel hits from the DefaultDigitizer module were stored in ROOT TTrees with the same formatting as test-beam data. This module was also used during the Forward-Backward Asymmetry studies to output relevant information about the MCParticle objects involved in simulations (see Section 6.9.)

For the majority of analyses performed for EPICAL-2, a direct comparison with Allpix² simulations at 1.0, 2.0, 3.0, 4.0, 5.0 and 5.8 GeV was performed, since the output from the CaloOutputWriter uses the same format as data. A total of 200,000 single-particle events were simulated at each of these beam energies.

6.3 Data Samples

Several sets of test-beam data were taken for EPICAL-2. The majority of the analysis in this chapter uses data recorded at the test beam facility at DESY [72], across two data-taking periods with e^+/e^- beams of between 1 GeV and 6 GeV. Additional e^+/e^- data was taken at CERN SPS between 20 GeV and 80 GeV.

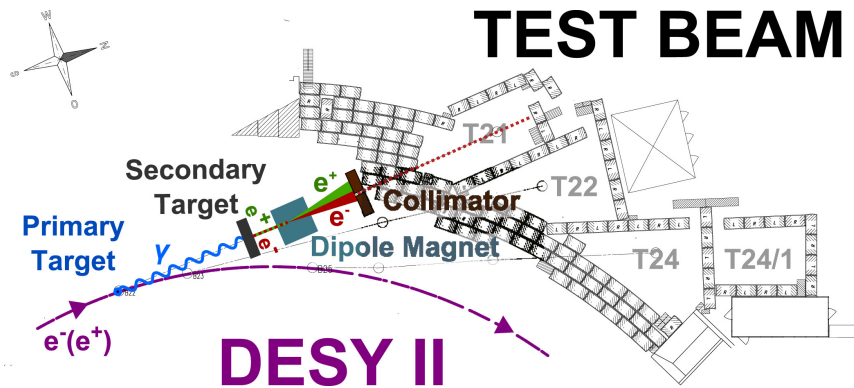


Figure 6.10: Production of the test beam for beam line TB21 at Deutsches Elektronen-Synchrotron (DESY). Taken from [72]

6.3.1 DESY Test Beam

The DESY II test beam facility is illustrated in Figure 6.10. Bremsstrahlung photons are produced by collision of an electron or positron beam with the primary target, which is made of carbon fibre several μm thick and located within the main orbit of the beam. These are then extracted tangentially to the beam direction and propagated to the secondary target, which is either copper or aluminium of varying thickness and is located up to 22 m behind the primary target, dependent on which test beam is being used. Collision of the bremsstrahlung photons with the secondary target induces pair production of electrons and positrons.

A dipole magnet with a maximum field of 1.38 T is located 60 cm downstream from the secondary target. This magnet is used to separate the electrons and positrons produced from the secondary target. The magnitude of the magnetic field is used to select the desired momentum, and the polarity of the magnet is used to select the desired particle type. An additional magnet is required downstream for the TB24 and TB24/1 areas in order to deflect the beam into the test beam area.

The beam is then passed through the primary collimator, which is two pairs of 10 cm thick tungsten ‘jaws’, one oriented vertically and the other horizontally, with the jaw position controlled remotely from the control huts using the controls shown in Figure 6.11. The beam passes from this collimator to the beam shutter, which is

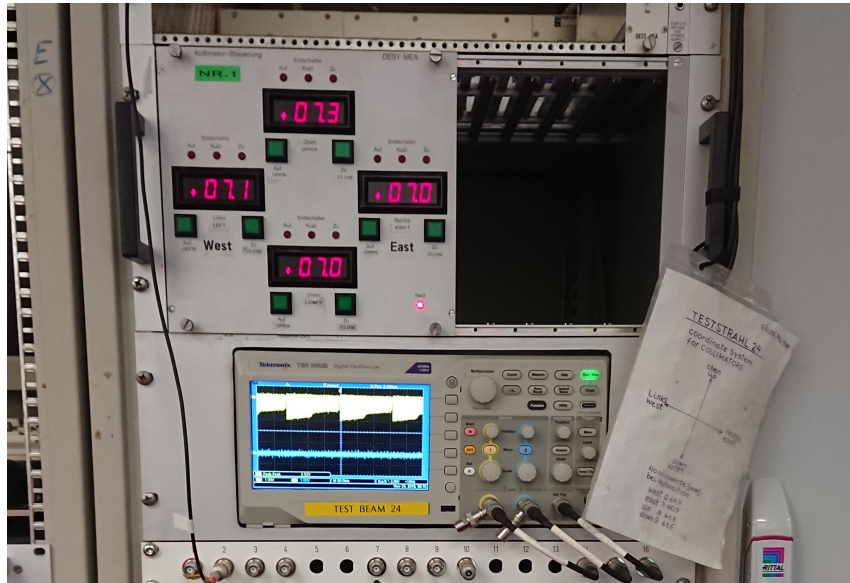


Figure 6.11: Control panel for the primary collimator used in the test beam area TB24/1 at DESY II.

located directly before the opening in the shielding wall and is used to shut off the beam when access to the test beam area is required. Lastly, a secondary collimator may be placed in a receptacle inside the beam area. This collimator is a cylindrical volume of lead with a square section of material removed from the centre, as depicted in Figure 6.12.

Devices to be tested using the beam are placed upon a movable platform with a mechanical lifting element, which is controllable from within the control huts. A laser alignment system is used to ensure that the target is aligned with the beam direction.

6.3.2 November 2019 DESY Data-Taking

During late November and early December 2019, two weeks of 1–5 GeV electron beam data were recorded using the initial 12-layer half-prototype of EPICAL-2 collected in the DESY test beam area TB24/1. The experimental layout of the half-prototype is shown in Figure 6.13.



Figure 6.12: Secondary collimator used in the test beam areas TB24/1 at DESY II.

Table 6.1: Data recorded at each energy during the November 2019 data-taking run at DESY II test beam area TB24/1, using nominal settings.

Energy (GeV)	Number of Events (no secondary collimator)	Number of Events ($6 \times 6 \text{ mm}^2$ secondary collimator)
1	6×10^5	3×10^5
2	6×10^5	6×10^5
3	12×10^5	12×10^5
4	6×10^5	6×10^5
5	12×10^5	12×10^5
5.6	6×10^5	3×10^5
5.8	3×10^5	3×10^5

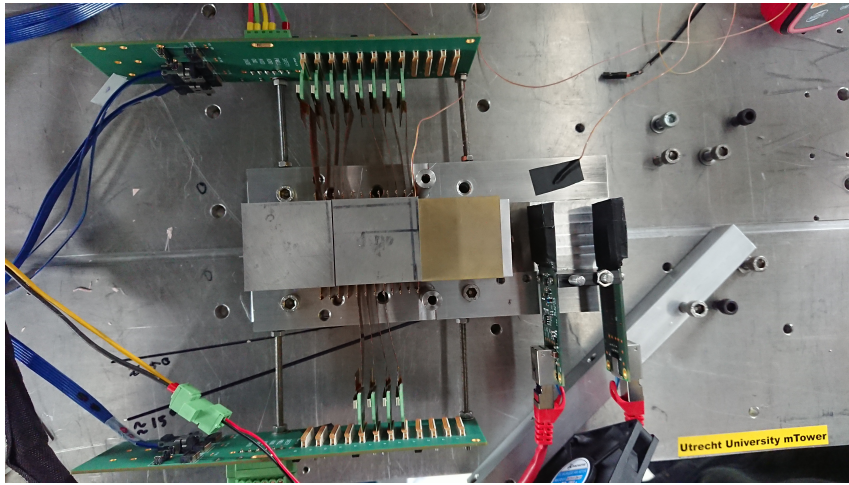


Figure 6.13: The half-prototype of EPICAL-2 as it was set up during the November 2019 data taking at DESY II area TB24/1.

The typical setup for data-taking used $\approx 14 \times 14 \text{ mm}^2$ primary collimator settings (see Figure 6.11.) The beam was incident on the geometric centre of the prototype, with the beam perpendicular to the detector face. Approximately 5.1×10^6 total events were recorded without a secondary collimator at a variety of energies between 1.0 GeV and 5.8 GeV, with a further 4.5×10^6 events recorded using a $6 \times 6 \text{ mm}^2$ secondary collimator, as summarised in Table 6.1.

In addition to the events taken using typical settings, events were also taken using a variety of alternative settings, which varied the angle between the prototype and the beam and the presence of additional blocks of tungsten in front of the detector face. Data taking using these alternative settings is summarised in Table 6.2.

The data taken during the November 2019 period were used primarily to develop software tools for data management and analysis, in preparation for the February 2020 data taking using the full EPICAL-2 prototype.

6.3.3 February 2020 DESY Data-Taking

During February 2020, two weeks of electron/positron data were recorded using the full EPICAL-2 prototype at the DESY test beam area TB22, again with nominal beam

Table 6.2: Data recorded at each energy during the November 2019 data-taking run at DESY II test beam area TB24/1, with alternative settings.

Energy	Number of Events
18 mm block of tungsten placed in front of the detector face (6 × 6 mm² secondary collimator)	
3 GeV	3×10^5
5 GeV	3×10^5
36 mm block of tungsten placed in front of the detector face (6 × 6 mm² secondary collimator)	
3 GeV	3×10^5
5 GeV	3×10^5
Prototype placed at 5.3° angle to the beam (6 × 6 mm² secondary collimator)	
1 GeV	3×10^5
2 GeV	6×10^5
3 GeV	6×10^5
4 GeV	6×10^5
5 GeV	6×10^5
5.6 GeV	3×10^5
Prototype placed at 15.7° angle to the beam (6 × 6 mm² secondary collimator)	
1 GeV	3×10^5
2 GeV	3×10^5
3 GeV	3×10^5
4 GeV	3×10^5
5 GeV	3×10^5
Prototype placed at 180° angle to the beam (6 × 6 mm² secondary collimator)	
3 GeV	3×10^5
5 GeV	3×10^5

energies of between 1.0 GeV and 5.8 GeV. The setup of EPICAL-2 used during data taking for this period is shown in Figure 6.14.

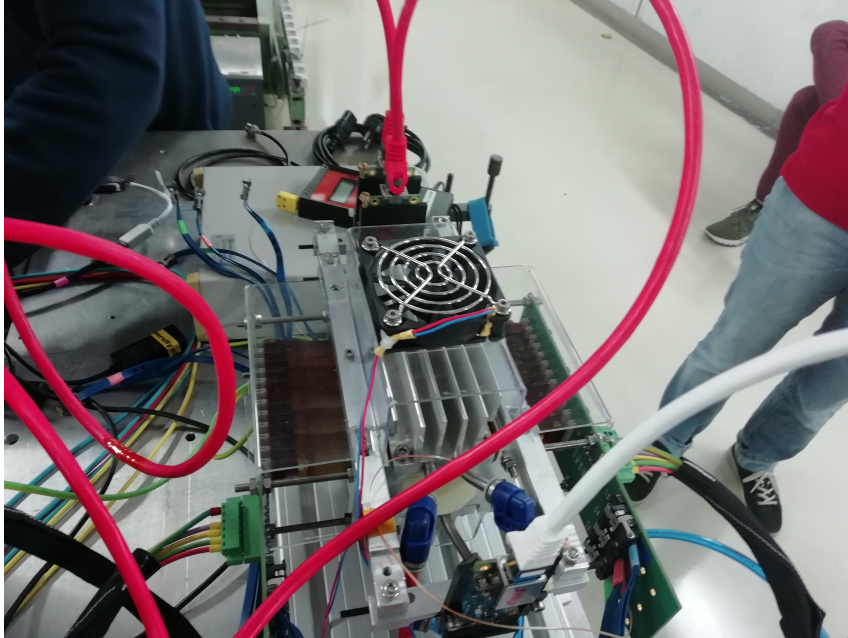


Figure 6.14: The EPICAL-2 prototype as it was set up during the November 2019 data-taking at DESY II area TB22.

The EPICAL-2 prototype was upgraded from the November 2019 run to include all 24 layers. A cooling system was implemented using a top-mounted fan to provide air cooling if required as well as a water-cooling system which can maintain a steady temperature, which can be seen in Figure 6.15.

Typical settings for data taking used a stable temperature of 20.1°C maintained by water cooling. The primary collimators were set to $14 \times 14 \text{ mm}^2$, and a $12 \times 12 \text{ mm}^2$ secondary collimator was used. The prototype was set up with the detector face perpendicular to the beam direction and a default beam position in the nominal geometric centre of the prototype. The strobe duration was set at $2\mu\text{s}$. Approximately 13.7×10^6 events were recorded across six different energies, with the summary by nominal energy given in Table 6.3.

In addition to events recorded using typical settings, events were also taken using a variety of alternative settings, which included varying the angle of the prototype to the beam, the temperature maintained by the cooling system, the position of



Figure 6.15: The water-cooling system used to maintain a steady temperature over the EPICAL-2 prototype during data-taking in February 2020.

the beam on the front surface of the detector, the strobe length, and the collimator settings.

The temperature was varied for a small number of data-taking runs, as summarised in Table 6.4. Similarly, Table 6.5 summarises the data recorded when varying the incident beam position on the front surface of the detector; this was controlled by adjusting the mechanical platform provided by DESY.

Table 6.6 shows the data that were taken at incident angles other than 0° . The

Table 6.3: Data recorded at each energy during the February 2020 data-taking run at DESY II test beam area TB22, with nominal settings.

Energy	Number of Events
1 GeV	2.382×10^6
2 GeV	2.373×10^6
3 GeV	1.811×10^6
4 GeV	2.168×10^6
5 GeV	3.484×10^6
5.8 GeV	1.519×10^6

Table 6.4: Data recorded at each energy during the February 2020 data-taking run at DESY II test beam area TB22, for varying temperature settings.

Energy	Number of Events
25°C	
1 GeV	1.593×10^6
3 GeV	0.807×10^6
5 GeV	0.818×10^6
30°C	
1 GeV	0.819×10^6
3 GeV	0.819×10^6
5 GeV	0.966×10^6

prototype rested on a steel platform and an adjustable arm, pictured in Figure 6.16, was used to elevate the rear of the detector. In order to accommodate the new angle of approach, the scintillator trigger pads were lowered or raised accordingly within their supports, but kept parallel to the detector surface. For the reversed runs ($\theta = 180^\circ$), only two of the scintillator pads were used—one either side of the prototype.

Lastly, data was taken using a positron beam rather than an electron beam, which is detailed in Table 6.7.

The data taken during the two-week February 2020 test beam period was used in the majority of EPICAL-2 analysis, and forms the data sets that are studied in the analyses of Sections 6.7, 6.8 and 6.9.

Table 6.5: Data recorded at each energy during the February 2020 data-taking run at DESY II test beam area TB22, for varying positions of the beam. The position of the beam on the detector face is given by the difference from the geometric centre of the EPICAL-2 prototype, (x_c, y_c)

Energy	Number of Events
Position 1 $x_1 = x_c + 8.0$ mm, $y_1 = y_c - 8.0$ mm.	
1 GeV	0.588×10^6
3 GeV	0.593×10^6
5 GeV	0.588×10^6
Position 2 $x_2 = x_c - 8.0$ mm, $y_2 = y_c$.	
1 GeV	0.297×10^6
3 GeV	0.297×10^6
5 GeV	0.295×10^6
Position 3 $x_3 = x_c + 8.9$ mm, $y_3 = y_c + 7.6$ mm.	
1 GeV	0.294×10^6
3 GeV	0.297×10^6
5 GeV	0.297×10^6
Position 4 $x_4 = x_c + 8.9$ mm, $y_4 = y_c$.	
1 GeV	0.594×10^6
3 GeV	0.297×10^6
5 GeV	0.296×10^6

Table 6.6: Number of events taken at each energy during the February 2020 data-taking run at DESY II test beam area TB22, for varying angles which EPICAL-2 was placed at with respect to the beam.

Energy	Number of Events
$\theta = 2^\circ$	
1 GeV	0.444×10^6
3 GeV	0.447×10^6
5 GeV	0.447×10^6
$\theta = 10^\circ$	
1 GeV	0.444×10^6
3 GeV	0.446×10^6
5 GeV	0.446×10^6
$\theta = 20^\circ$	
1 GeV	0.444×10^6
3 GeV	0.447×10^6
5 GeV	0.444×10^6
$\theta = 180^\circ$	
1 GeV	0.735×10^6
2 GeV	0.742×10^6
3 GeV	0.737×10^6
4 GeV	0.744×10^6
5 GeV	0.743×10^6

Table 6.7: Number of positron events taken at each energy during the February 2020 data-taking run at DESY II test beam area TB22, utilising typical settings.

Energy	Number of Events
1 GeV	0.423×10^6
2 GeV	0.892×10^6
3 GeV	0.435×10^6
4 GeV	0.444×10^6
5 GeV	0.294×10^6
5.8 GeV	0.305×10^6

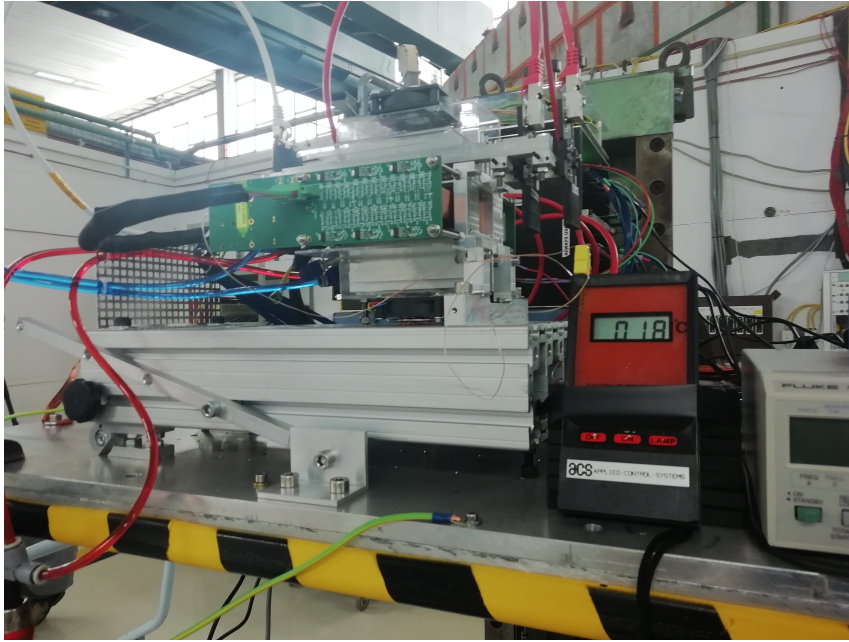


Figure 6.16: The horizontal view of the EPICAL-2 prototype used during data-taking in February, including the platform and inclining arm used to elevate the rear of the prototype during angled beam tests.

6.4 Data Quality Assurance

Between the two beam tests at DESY II in November 2019 and February 2020, the beginnings of a Data Quality Monitoring (DQM) system was developed for real time monitoring of the data quality during beam tests. However, the software was not completed in time for the two test beams, and so data quality had to be monitored manually during the course of the data taking, and evaluated retrospectively to ensure that only desirable events were retained for use in analysis.

Data was taken in several runs, each comprising several thousand events, and stored in a collection of ‘pickled’ data files¹. A script was used to convert a series of pickled files into a generic ROOT-readable format, which was applied post facto and manually operated by the user. Before the February 2020 beam test, a suite of software tools² was developed which checked which files had already been converted to ROOT format, and automatically began converting any data which had finished

¹A format used to convert Python objects and their dependencies into a stream of bytes.

²This consisted of Makefiles, cron jobs and utility scripts.

writing but had not yet been converted. This system dramatically reduced the time between the data taking in each run, and so allowed the faster diagnosis of any problems.

Between shifts of runs (at least as often as once every 8 hours) a pedestal run was performed. For these runs, the beam was shut off, and the strobe was triggered by a digital signal produced by the readout boards rather than a signal from the scintillator beam monitors introduced in Section 6.1.3. This allowed any changes in the behaviour of pixels, such as new dead or ‘hot’ pixels, to be logged, in case of any damage.

During the earliest data taking in February 2020 (approximately the first 2 hours), it was found that one of the chips in layer 21 was generating readout errors of unknown origin which were disruptive to data taking, and was completely prohibitive to the data conversion from pickled to ROOT format. As such, that single chip was completely removed from the readout for the remainder of the data taking. Removing one of the chips inevitably had the effect of smearing the resulting energy resolution, but since the chip was well beyond the expected shower maximum position in depth, its impact is expected to be small.

6.4.1 C Event Display

In order to visualise individual events post-conversion, an event display was developed by adapting the pre-existing C Event Display (CED) package [73] developed for ILC, implemented in the Marlin framework [74].

The EPICAL-2 prototype was implemented in a simple geometry arrangement, using only the 24 silicon layers with no segmentation for individual pixels. An option was added to remove the first 12 layers, the last 12 layers, or all layers from visualisation. In addition, a processor within Marlin was developed in order to select specific events from a combination of the run number and the event number. Conversion of the data from ROOT format to Linear Collider Input/Output (LCIO) format [75] is

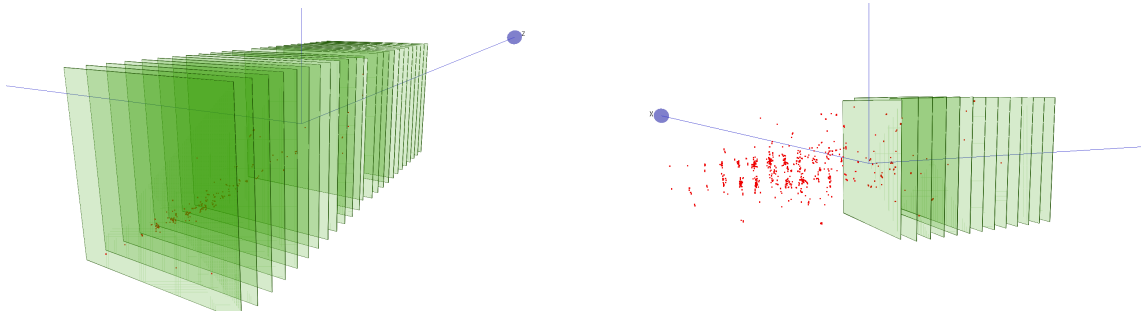


Figure 6.17: Examples of 5 GeV events visualised using the EPICAL-2 CED, taken from the February 2020 DESY II test beam data set. A single-electron event is shown on the left, and a two-electron event from the same run on the right.

required for input into CED. Since conversion to LCIO is very time-consuming and would create storage problems if performed upon all data, the conversion software was configured to select individual events or runs from a ROOT file rather than converting the entire data set at one time.

Two examples of events from the EPICAL-2 CED implementation are shown in Figure 6.17. The event display was used to examine any unusual individual events, such as those with unexpectedly low or high numbers of recorded hits.

6.4.2 Systematic Low-Event Region

During the February 2020 running, a series of hitmaps produced from the first few runs revealed a systematic region of the detector with an unexpectedly low hit density compared to the outlying region. This low-event region is depicted in Figure 6.18, where in Layer 0 (i.e. the sensors at the frontmost face of the detector) there is a clear crescent-shaped deficiency in hits to the right of the beam spot. The feature becomes less pronounced with increasing depth in the beam direction.

The chief concern with this feature in the data was that there might be some problem on the chip level, perhaps a defect with the readout, or a spurious voltage applied to some pixels rather than others. In order to eliminate this possibility, three investigations were made.

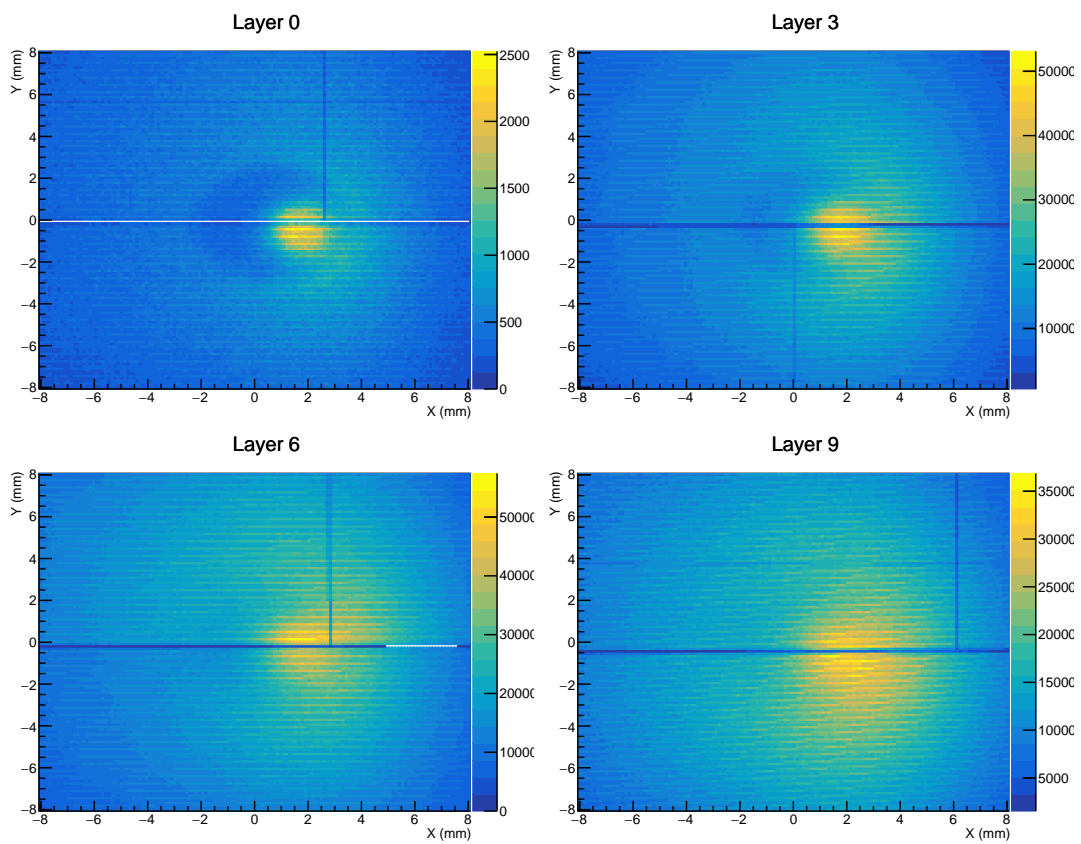


Figure 6.18: Hitmaps for a selection of layers using the 5 GeV data set with typical data-taking settings.

The first was to consult the data taken for varying positions on the detector surface, the hitmaps of which are shown in Figure 6.19. It can be seen that the crescent-shaped feature does not follow the beam position, and so does not appear to be a product of a feature in the beam.

In addition, hitmaps showing data which had been taken at 20° were produced, which are shown in Figure 6.20. Since the feature appears to travel with the concentration of hits in the chip position rather than remaining at a constant position, the conclusion was that the cause was likely to be a product of something upstream of the prototype such as the scintillator pads. A non-uniform response close to the MPPC seemed likely since the dimple in the scintillator pad used to accommodate the MPPC was of an appropriate size (≈ 3 mm radius), and the MPPC itself sits slightly off-centre inside the dimple. Furthermore, a small non-uniformity in the efficiency of CLAWS modules close to the SiPM had already been found previously [76].

Lastly, in order to confirm that the data was indeed not significantly affected by the non-uniformity in the trigger efficiency, distributions of the number of pixels over threshold per event (N_{Hits}) were compared for two regions: one inside the apparent region of the feature, and one outside it. For this study the 5 GeV data set with typical settings was used, and the Jet-Finding event selection applied (see Section 6.6.3). The feature is still present after application of the event selection, as can be seen on the left side of Figure 6.22. For each event, if the beam position determined by the event selection lay within a rectangular section subtended by $-2 \text{ mm} < x < 0 \text{ mm}$ and $-2 \text{ mm} < y < 2 \text{ mm}$, it would be included in the ‘inside feature’ distribution. If instead the beam position was within the rectangular section subtended by $3 \text{ mm} < x < 5 \text{ mm}$ and $-2 \text{ mm} < y < 2 \text{ mm}$ then it would be included in the ‘outside feature’ distribution.

Figure 6.22 shows the N_{Hits} distributions for the two regions overlaid. While there are small differences between the two distributions, the width remains highly comparable and the small difference in means is within the margins defined by the momentum spread of the beam (≈ 158 MeV). It was decided based on this anal-

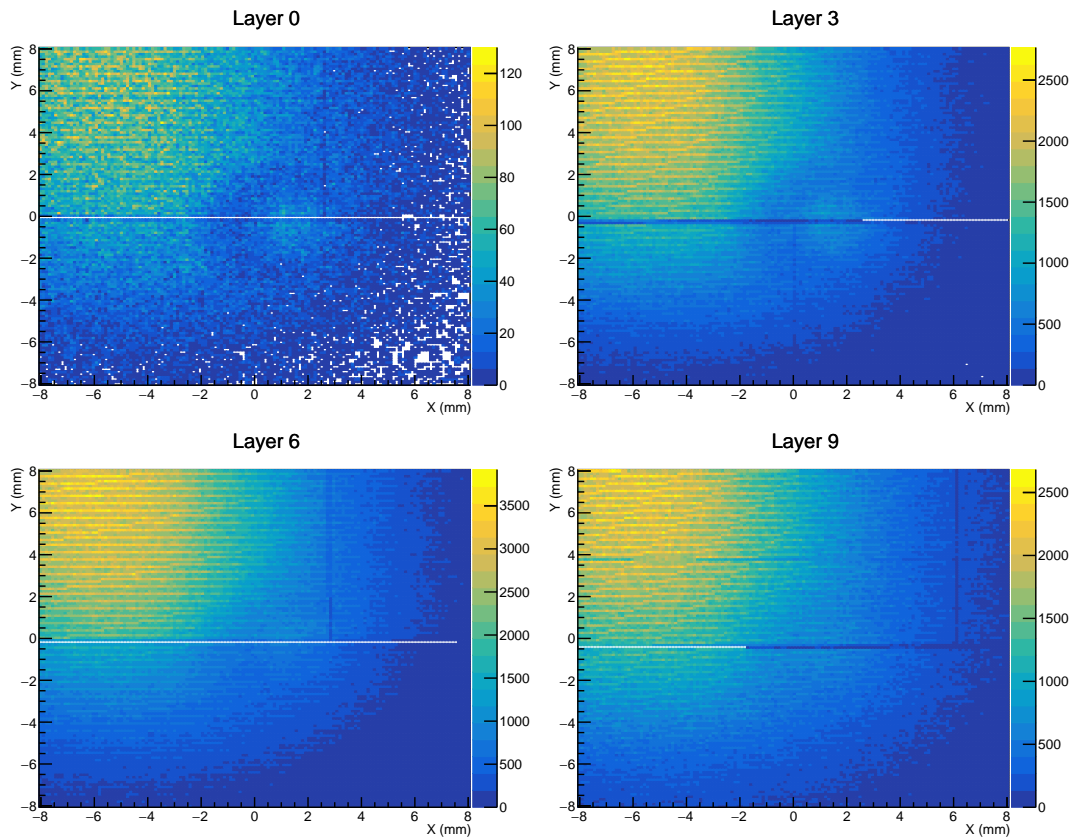


Figure 6.19: Hitmaps for a selection of layers using the 5 GeV dataset for Position 1 (see Table 6.5).

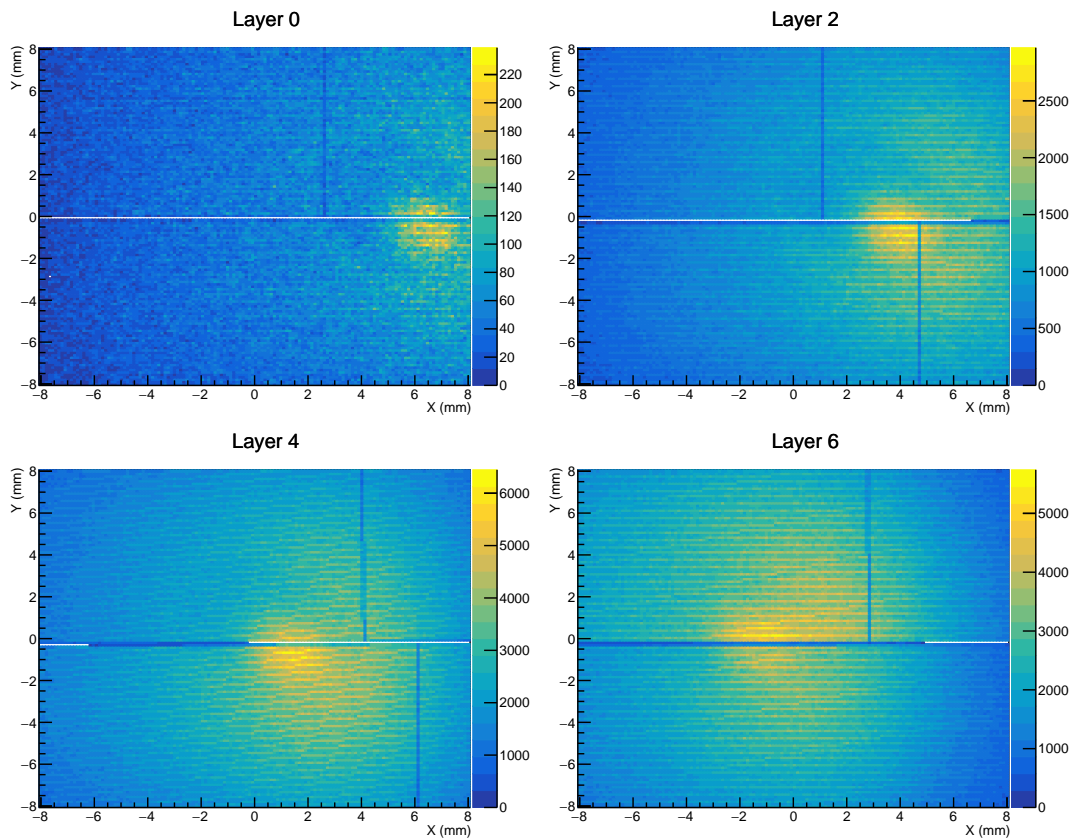


Figure 6.20: Hitmaps for a selection of layers using the 5 GeV data set for 20° inclination to the beam.

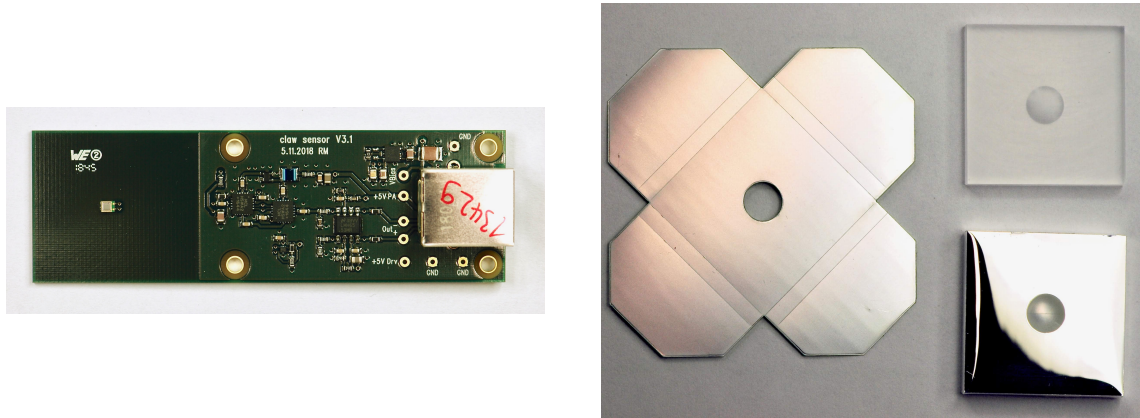


Figure 6.21: Left: A CLAWS unit used in triggering, prior to the addition of the scintillator tile, with the off-centre MPPC visible. Right: The standalone plastic scintillator tile with the dimple visible (top right), the reflective foil map (left), and the combined structure ready for bonding to the CLAWS module (bottom right).

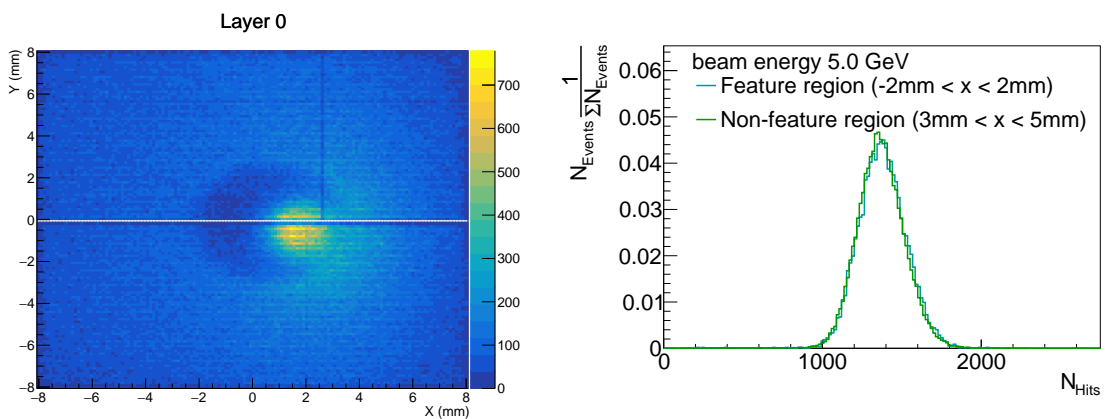


Figure 6.22: Left: Hitmap in Layer 0 of the 5 GeV data from the February 2020 test beam, using typical settings, after application of the Jet-Finding event selection. Right: N_{Hits} distributions for two region-based cuts on the beam position found using the Jet-Finding event selection (see Section 6.6.3).

ysis that there was no requirement to perform any removal of data based on the inefficiency, which was plausibly due to the combination of two inefficiencies in the upstream scintillator triggers.

6.5 Calibration

The raw data are analysed after format conversion to ROOT and may contain various sources of potential error. Improperly functioning pixels can smear the N_{Hits} distributions, and the non-uniformity of pixel thresholds on a chip-by-chip basis can significantly impact the performance. In addition, small misalignments of the chips have the potential to introduce difficulties when performing the event selections in Section 6.6. The corrections in this section are designed to counter these potential sources of error.

6.5.1 Pixel Masking

Pixels may malfunction in two ways: they may produce an uncharacteristically large number of signals ('hot' pixels) or an uncharacteristically small number of signals ('dead' pixels) compared to the majority. The production of a pixel mask is designed to mitigate the problems by excluding such pixels from the data.

Noisy and dead pixels were first identified by a functionality test, which was performed during chip commission and classification. In this test, signals were injected directly into the front-end pixel circuitry. This allowed direct evaluation of dead pixels (since no signal is returned), and some ability to identify hot pixels.

Additionally, the pedestal runs performed during the data-taking (see Section 6.4) allow for further identification of noisy pixels. Since no signal is expected during pedestal runs, any pixels firing significantly often during these runs are considered noisy, and were removed by the pixel mask.

Lastly, it was found that the pixels that border each ALPIDE chip return systematically fewer signals than other pixels. As such, these pixels are also removed by the pixel mask.

The pixel mask removes $\approx 0.95\%$ of the total pixels in the prototype from the data. Of this group the vast majority are border pixels, which comprise $\approx 0.65\%$ of all pixels. Dead pixels comprise $\approx 0.28\%$ of the EPICAL-2 pixels. Lastly, $\approx 0.015\%$ of pixels are found to be hot pixels [77].

6.5.2 Chip Corrections

Having removed any atypical pixel behaviour via the pixel mask, the next correction to be made was to apply a chip-by-chip correction to the signal response. Each ALPIDE chip propagates a single threshold to all constituent pixels. Ideally, all 48 ALPIDEs would have the same threshold. However, small differences in temperature, bias voltage etc. can cause small differences in the sensitivity between chips. Chip correction factors were therefore formulated to ensure uniformity of response across the whole EPICAL-2 prototype. Pixel efficiency variation within each chip is presumed to be negligible for the EPICAL-2 prototype.

The chip corrections were computed using cosmic muon tracks. ≈ 9000 cosmic muon events were recorded using EPICAL-2 during the months between the November 2019 and February 2020 test beams. Of these, ≈ 4900 were selected for use in chip corrections and alignment, using a cut around the centre of the N_{Hits} distribution for cosmic muon events.

For each chip, the mean number of hits in each chip $\langle N_{Hits} \rangle_{chip}$ is computed per throughgoing muon event. This is then divided by the mean value of $\langle N_{Hits} \rangle_{chip}$ across the whole sensor to find the calibration factor for each chip.

6.5.3 Alignment

The precision with which the “as built” mechanical construction of the EPICAL-2 prototype is known is much worse than the scale of a single pixel. It was therefore necessary to perform a data-driven alignment correction. The same selection of cosmic muon events used in the chip correction studies was used for this purpose.

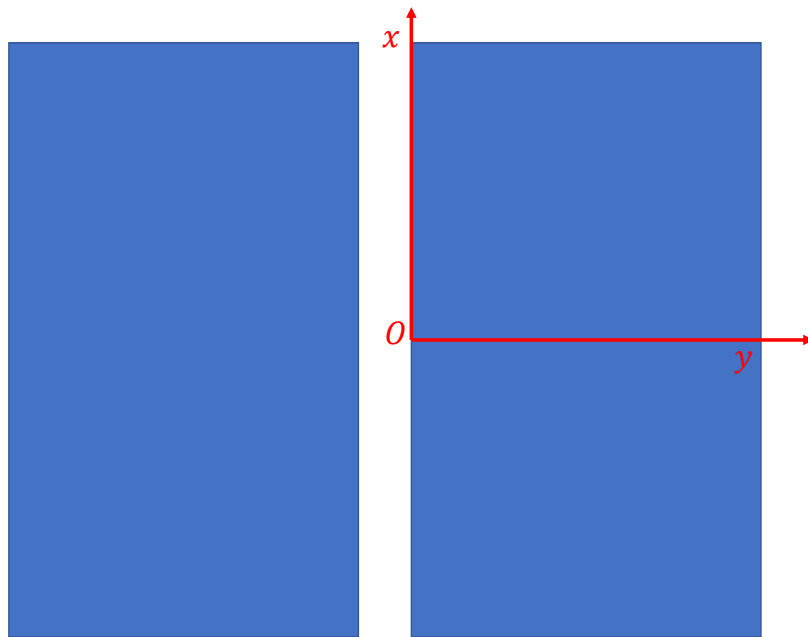


Figure 6.23: Front face of the EPICAL-2 prototype as seen by the beam, with the origin and lateral axes of the coordinate system used for the alignment overlaid.

It was first necessary to define a world coordinate framework around which to build the alignment model of EPICAL-2. A Cartesian coordinate system is used, wherein the right-most chip (as viewed from the front) in Layer 0 is used as the baseline, which we will label chip C_0 . The y direction is defined as the direction from left to right following the short sides of C_0 , the x direction is defined as the direction from bottom to top following the long sides of C_0 , while z is the direction downstream which is perpendicular to the face of C_0 . The origin is defined as the centre of the left-most long side of C_0 (such that the silicon in C_0 lies between $z = -27.5 \mu\text{m}$ and $27.5 \mu\text{m}$). The orientation of the lateral dimensions and position of the origin are shown in Figure 6.23.

In principle there are six degrees of freedom in the placement of each chip: three Cartesian coordinates and three rotational angles. For the alignment studies it was assumed that as a result of the well-defined thickness of the tungsten plates, the orientation of the transverse plane (i.e. rotations in the $x - z$ and $y - z$ planes) and the depth (translation in z) do not introduce any significant uncertainty. Therefore, only three degrees of freedom remain; translation in x and y , and rotation about the z axis θ_z .

A complication in considering the alignment is that relatively few cosmic muon tracks traverse from one half of the detector to the other (i.e. from right to left, or vice versa). The alignment procedure was developed as follows:

- Alignment of sensors on the right side of the prototype was performed using tracks which only traversed the right side. The alignment of sensors was determined relative to C_0 .
- Alignment of sensors on the left side of the prototype was performed using tracks which only traversed the left side. The alignment was determined relative to the sensor on the left in Layer 0 (i.e. directly to the left of C_0).
- The alignment of the right side of the detector is fixed, and the alignment of the left side performed relative to C_0 using only tracks which crossed from one side of the detector to the other.
- The alignment of all sensors is repeated using all tracks, all relative to C_0 .

At each of the above stages in the alignment, the χ^2 of each track event was calculated and summed into a χ^2 across all events. The three alignment parameters were then varied during a minimisation procedure until a stable solution was found.

Prior to the alignment the residuals of cosmic muon tracks reached up to $\mathcal{O}(100 \mu\text{m})$. Post alignment, these residuals were reduced to the level of $< 5 \mu\text{m}$, much smaller than the scale of a single pixel [78].

6.6 Event Selection

The data that were recorded during the February 2020 test beam run of EPICAL-2 contained a wide variety of events. In order to evaluate the performance of the detector, it was desirable to observe single-particle events. Many of the events in the 2020 data set showed clear evidence of there being more than one particle shower, such as that shown in Figure 6.17. These events are generally caused by one beam particle activating the scintillator triggers, which is then followed by another particle incident upon the prototype within the $2 \mu\text{s}$ readout cycle, and is the result of the relatively high beam rate during data-taking. Events in which the EM shower is not fully contained by the lateral size of EPICAL-2 are also undesirable, since they reduce the number of pixels over threshold in the event and thereby smear the left side of the N_{Hits} distribution.

Two algorithms were developed to remove undesirable events at analysis runtime: The Multi-Cut algorithm and an event selection derived from the kT-Algorithm. The objectives of these algorithms are:

- Remove events which contain more than one particle shower (i.e. pileup events.)
- Remove events which contain no particle shower (i.e. faulty triggering.)
- Remove events in which a portion of the shower has leaked out of one or more sides of the detector.

6.6.1 Clustering Algorithm

Both event selection algorithms detailed in the subsections below use ‘clusters’ rather than hits in their application. Additionally, cluster analysis was performed as part of the performance evaluation in Section 6.7. For both of these applications, the Density-Based Spatial Clustering of Applications with Noise (DBSCAN) clustering

algorithm was used with no restriction upon the minimum density of a cluster [79]. The algorithm proceeds as follows:

- One of the pixel hits which is not yet assigned to a cluster is selected to start a new cluster. This pixel hit p_0 with position $\bar{x}_0 = (x_0^i, x_0^j)$ is assigned to a new cluster c .
- Pixel hits p_n which are adjacent to p_0 (i.e. $[\sum_{p=1}^2 \text{mod } x_{np} - x_{0p}] < [29.24 \oplus 26.88\mu\text{m}]$) are also assigned to cluster c .
- For all pixel hits p_m currently assigned to cluster c , any adjacent pixel hits p_n (i.e. $[\sum_{p=1}^2 \text{mod } x_{np} - x_{mp}] < [29.24 \oplus 26.88\mu\text{m}]$) not currently assigned are assigned to cluster c . This continues until all unassigned pixel hits are not adjacent to any pixel hits assigned to c .
- The cluster c is assigned a cluster position equal to the unweighted centre-of-mass of the pixel hits assigned to the cluster. The cluster is assigned a cluster size equal to the number of pixel hits assigned to it.
- Repeat the above steps until there are no pixel hits which are unassigned to a cluster.

DBSCAN is not dependent upon the order in which pixels are considered, and serves only to group neighbouring pixels. The DBSCAN algorithm was applied to each chip in turn, so that no cluster spans two layers, or two chips in a single layer.

6.6.2 Multi-Cut Event Selection

The Multi-Cut event selection imposes a set of sequential criteria upon events as described below.

Clusters in the most upstream three layers (Layer 0, Layer 1, Layer 2) are used in the event selection. Clusters in at least two of these three layers with transverse cluster

positions within $300 \mu\text{m}$ of each other are grouped into particle ‘candidates’ c_{nm} , where n and m are the layer numbers of the clusters used to generate the candidate ($n < m$). A single cluster may generate several candidate objects, which is shown in Figure 6.24. A position is attached to each candidate, which is determined by the position of the most up-stream contributing cluster.

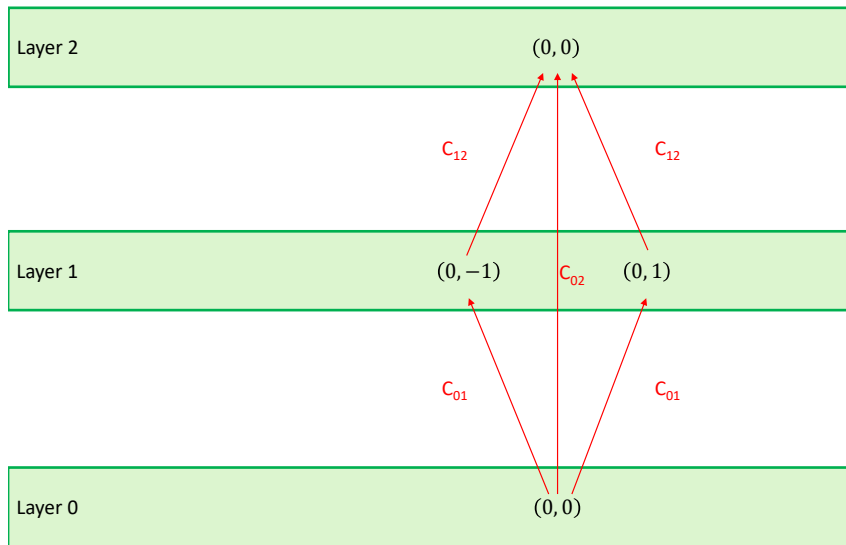


Figure 6.24: Example of how particle candidates are generated in the Multi-Cut event selection. Clusters are marked with coordinates indicating their lateral position (in arbitrary units), and generated candidate objects marked and labeled in red.

Each candidate object is produced as evidence of a throughgoing particle and the subsequent developing EM shower. Because several candidates may provide evidence of one developing shower, some additional cuts are made to avoid convolution. c_{01} candidates are the most desirable evidence, while c_{02} and c_{12} candidates are desirable only where there is no c_{01} candidate available (i.e. where there are missing clusters in Layer 1 or Layer 0 respectively).

Firstly, any c_{12} candidates which have positions within $600 \mu\text{m}$ of a c_{0m} candidate (i.e. a candidate with a contributing cluster from Layer 0) are removed from consideration, since the c_{12} candidate is just further evidence of the throughgoing particle found by the c_{0m} candidate.

Additionally if there are two c_{12} candidates with positions within $600 \mu\text{m}$ of each other (which have not been eliminated by prior cuts) the two candidates are merged, i.e. they are replaced by a single c_{12} candidate with new position equal to the centre-of-gravity of the merged candidates. Since c_{12} candidates are used as a last resort where there is no Layer 0 cluster to provide good evidence of a single incident particle, several may be produced as part of a single EM shower, and so these candidates are merged to avoid over-counting the number of particles in an event.

After the above cuts on candidates are applied, the number of remaining candidates is evaluated analogously to the number of incident particles in the event $n_{\text{particles}}$. If $n_{\text{particles}} \neq 1$, the event is rejected, since single-particle events are a requirement of the selection.

If the event has not been rejected, a further cut upon the candidate position is performed to avoid events in which part of the EM shower is likely to have leaked out of the transverse area of the detector. If the candidate transverse position (x_c, y_c) is within 8 mm of any of the edges of the sensitive region of the layer, the event is rejected.

Lastly, as a final clean-up of events where additional showers may have started unusually deep in the EPICAL-2 prototype, if any cluster in Layer 1 is outside a 3.6 mm radius of the candidate's transverse position, the event is rejected.

Any events that have not been rejected have a single candidate cluster pair remaining which is located centrally in the detector, and are accepted by the Multi-Cut selection. The position of the incident particle is determined to be the centre-of-gravity of the most upstream cluster which contributed to the accepted candidate.

6.6.3 Jet-Based Event Selection

The Jet-Based Algorithm uses a jet-finding-like approach to search for particle showers rather than the cluster-grouping used in the Multi-Cut selection [80]. The algo-

rithm proceeds for each event as follows:

First, a grid of transverse cluster positions is defined, with smaller cells of size $0.5 \times 0.5\text{mm}^2$ in the central part of the detector ($|x| < 12\text{mm}$ and $|y| < 12\text{mm}$), and larger cells of size $1 \times 1\text{mm}^2$ in the outer part ($|x| \geq 12\text{mm}$ or $|y| \geq 12\text{mm}$). The finer binning in the centre reflects the desire for centrally positioned particles to be used in analysis, and thus the algorithm is optimised to find showers in the central part. Clusters from all 24 layers of the detector are considered in their relevant cells.

Once all clusters have been allocated to cells, each cell g which contains clusters from at least three different layers of the detector is transformed to produce a pseudo-jet j via the following transforms:

$$N_{\text{clus}}^c \rightarrow k_t^j \text{ (transverse momentum)} \quad (6.3)$$

$$x^g \rightarrow y^j \text{ (rapidity)} \quad (6.4)$$

$$y^g \rightarrow \phi^j \text{ (azimuth)} \quad (6.5)$$

An anti- k_t jet-clustering algorithm [81] is applied to the pseudo-jets, using $R = 0.5$ mm. Once the pseudo-jets have been clustered into ‘jets’ i , any jets with only one contributing pseudo-jet are discarded, as they are likely to be produced by rogue hits at the edge of showers as the result of shower particles travelling at particularly large angles to the beam direction.

After jet-finding and jet-removal, the number of jets remaining is assumed to be equivalent to the number of primary incident particles in the event. The event is therefore rejected if $N_{\text{jets}} \neq 1$, satisfying the requirement for single EM showers.

A cut is made upon the jet position (i.e. the centre-of-gravity of clusters in the final jet) - the event is rejected if it does not lie in a $16 \times 16\text{mm}^2$ central fiducial region in the transverse plane, to satisfy the requirement that jets should not be too close to the EPICAL-2 edge.

Several additional criteria are imposed, which are primarily to exclude multi-particle events with closely overlapping EM showers which would otherwise pass the selection, since the anti-kT algorithm often merges overlapping showers into a single jet. If any cluster in Layer 0 or Layer 1 has a position which is outside a 1 mm radius of the jet position, the event is rejected. Additionally, if any two clusters in Layers 0 and 1 which contributed to the final jet are separated by more than 0.5 mm, the event is likewise rejected. Finally, any event without a cluster in Layer 0 contributing to the final jet is rejected.

Any events that remain have a single jet located in a central region in the prototype, and so are accepted by the Jet-Based selection. The position of the beam is determined to be the centre-of-gravity of all clusters contributing to the final jet.

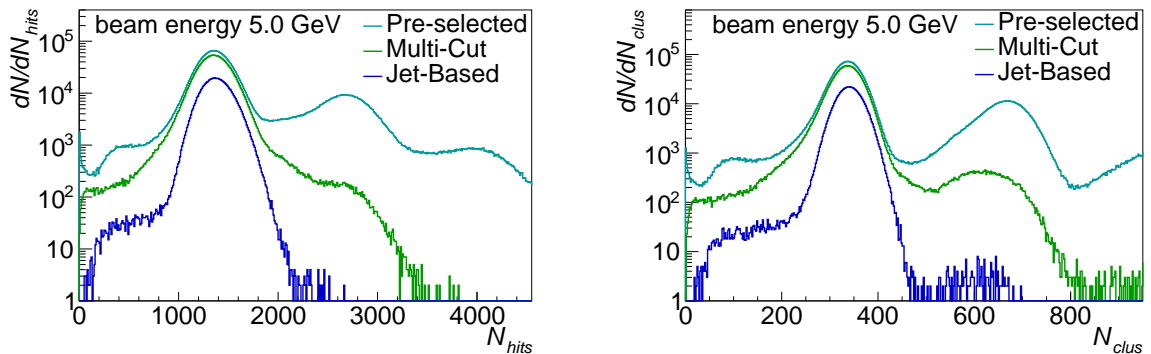


Figure 6.25: N_{Hits} (left) and N_{Clus} distributions (right) of the 5 GeV February 2020 EPICAL-2 dataset using typical settings (see Section 6.3.3.)

6.6.4 Performance of Event Selection Algorithms

The N_{Hits} and N_{Clus} distributions of the 5 GeV data before the application of any selection criteria, and the same data after each event selection algorithm is applied, are shown in Figure 6.25. The initial data contain several peaks at regular intervals, which are the result of multi-particle events.

The application of the Multi-Cut event selection results in the near complete removal of the three-particle peak (at ≈ 4000 hits). The two-particle peak is significantly reduced by a factor of ≈ 100 , such that the peak value is less than 1% that of the

peak value for the primary peak. The reduction of the primary peak is comparatively small.

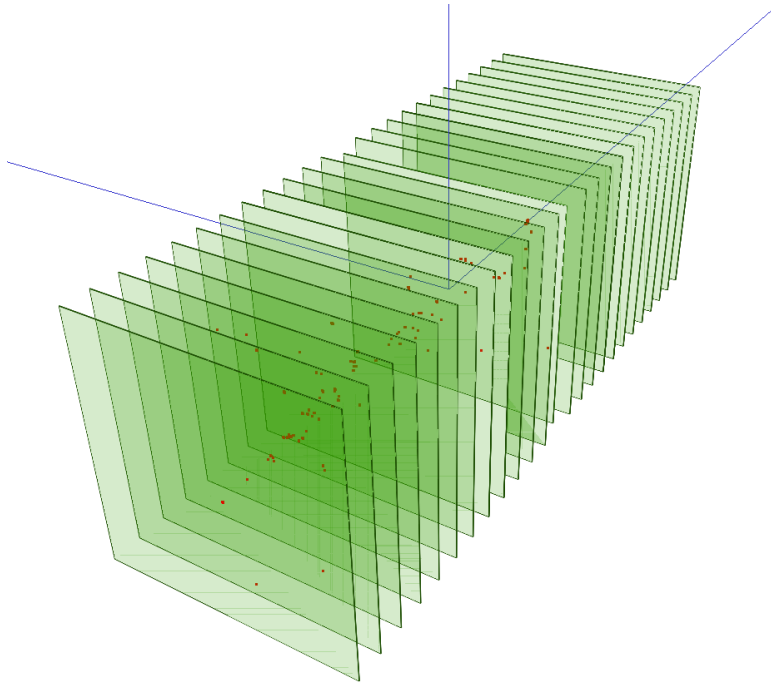


Figure 6.26: Example of a 5 GeV event with an unusually small number of pixels over threshold.

By contrast, the Jet-Based algorithm results in the complete removal of the three-particle peak, as well as the near-complete removal of the two-particle peak. However, there is a significant reduction in the primary peak as a result of the achieved high purity.

There is a prominent low- N_{hits} shoulder which remains present after both event selections are applied, at the level of $\approx 0.1\%$ of the peak value in each case. Investigations using the CED showed that these events do indeed contain a single shower, but with far fewer hits than would be expected. An example of one of these showers illustrated using the event display is shown in Figure 6.26. There is a clear, centrally located single shower. Explanations for this phenomenon include interference from the neutron beam background present at DESY II, or possible interference from the collimators leading to low-energy electrons entering the detector during data taking.

Table 6.8 shows the remaining events once each event selection is applied to the

Table 6.8: The number and percentage of events retained by each event selection across the entire N_{Hits} distribution.

Energy (GeV)	Unselected	Multi-Cut Selection		Jet-Finding Selection	
	N_{Events}	N_{Events}	Percentage	N_{Events}	Percentage
1	2,383,914	1,455,836	61.1%	321,009	13.5%
2	1,954,801	906,260	46.4%	201,850	10.3%
3	1,810,491	825,140	45.6%	220,121	12.2%
4	2,166,492	1,118,626	51.6%	317,067	14.6%
5	3,483,184	2,172,922	62.4%	649,541	18.6%
5.8	1,516,041	1,159,999	76.5%	350,496	23.1%

February 2020 EPICAL-2 datasets. However, this is only reflective of the overall number of events remaining for each selection. Table 6.9 shows the number of events remaining in a 400-wide window in the N_{Hits} distributions, centred on the bin with maximum content in each distribution.

Table 6.9: The number and percentage of events retained by each event selection, using only close to the maximum of each N_{Hits} distribution ($N_{Hits}^{maximum} - 200 \leq N_{Hits}^{event} \leq N_{Hits}^{maximum} + 200$).

Energy (GeV)	Unselected	Multi-Cut Selection		Jet-Finding Selection	
	N_{Events}	N_{Events}	Percentage	N_{Events}	Percentage
1	1,975,886	1,411,208	71.4%	318,377	16.1%
2	973,496	793,903	81.6%	193,378	19.9%
3	821,959	679,878	82.7%	200,960	24.4%
4	1,077,044	888,608	82.5%	275,464	25.6%
5	2,049,729	1,673,242	81.6%	539,882	26.3%
5.8	1,053,122	863,480	82.0%	280,487	26.6%

The Jet-Based algorithm is generally preferred for analysis due to its excellent pileup rejection. However, it has a considerably lower efficiency for the primary peak where it discards much of the core of desirable events. As such, the Multi-Cut selection is retained for use in analysis where more data are required.

6.7 EPICAL2 Overall Performance

The performance of EPICAL-2 is generically characterised by the linearity and the resolution, as is the case with any ECAL prototype. This section presents those results obtained from the February 2020 test beam data, as well as the longitudinal profile of EPICAL-2 and more general studies of the performance of the detector.

There are two variables that could be used to characterise the performance: the N_{Hits} distributions, or the N_{Clus} distributions found in Section 6.6.1. As a result of charge sharing between pixels, a single shower particle traversing perpendicularly through an ALPIDE might result in just one pixel being over threshold, or a group of four pixels being over threshold depending on the position of impact relative to the pixel matrix. In addition, non-perpendicular particles can result in the deposited charge being distributed across a large number of pixels. In the most severe cases (i.e. when a shower particle travels at close to 90° to the beam direction) this can create long track-like structures of $\mathcal{O}(100)$ pixel hits.

In principle, grouping neighbouring hits into clusters should remove some of the variation in response per particle, and so improve the resolution, since in principle each cluster should be representative of a single throughgoing shower particle. However, the clustering algorithm used does not make any attempt to resolve the overlapping clusters of two or more shower particles, and so the number of clusters in an event is likely to be more sensitive to saturation than is the number of hits.

6.7.1 Linearity

The Gaussian-like distributions of N_{Hits} and N_{Clus} are shown in Figure 6.27. One can see the generally excellent agreement between the Allpix² simulations and the EPICAL-2 data, particularly in the N_{Hits} case.

To compute the mean number of hits $\langle N_{Hits} \rangle$ (and likewise $\langle N_{Clus} \rangle$), the distributions in Figure 6.27 are fitted using Gaussian functions. The starting values of the fit are

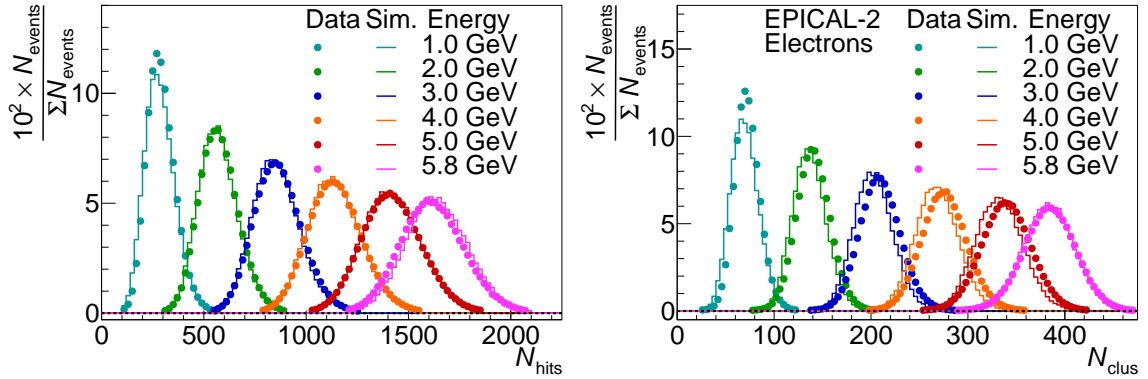


Figure 6.27: N_{Hits} (left) and N_{Clus} distributions (right) for all energies using the February 2020 EPICAL-2 data and the Allpix² simulations of EPICAL-2.

given by:

$$\mu_0 = \text{Centre value of the maximum bin} \quad (6.6)$$

$$\sigma_0 = \text{Half width at half maximum}$$

The fit is performed over a restricted range, which varies on a per-fit basis and is designed to exclude the low- N_{Hits} shoulder and any multi-particle events which were not excluded by the event selection. The range of the fit is given by:

$$r = 80 + (20 \times E(\text{GeV})) \quad (6.7)$$

$$\mu_0 - r < N_{Hits} < \mu_0 + r$$

The results of the Gaussian fits over this range are shown in Figure 6.28.

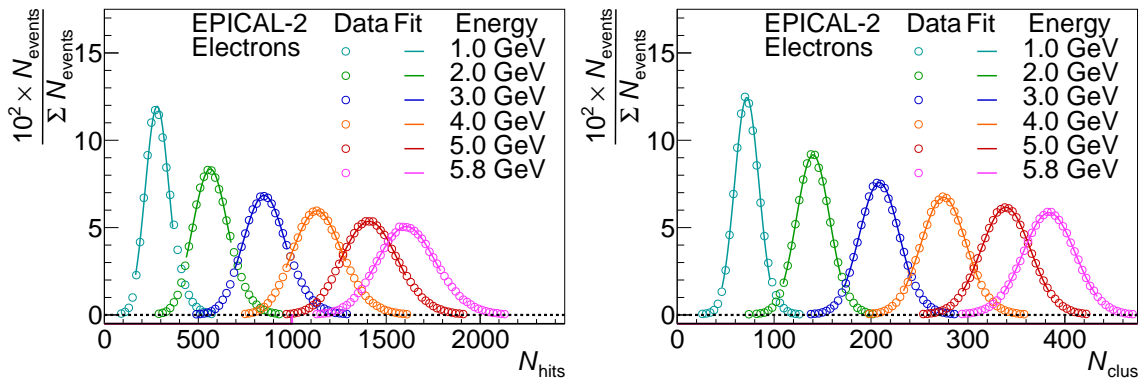


Figure 6.28: N_{Hits} (left) and N_{Clus} distributions (right) for all energies using the February 2020 EPICAL-2 data, with Gaussian fits over the ranges defined in Eq. 6.7 overlaid.

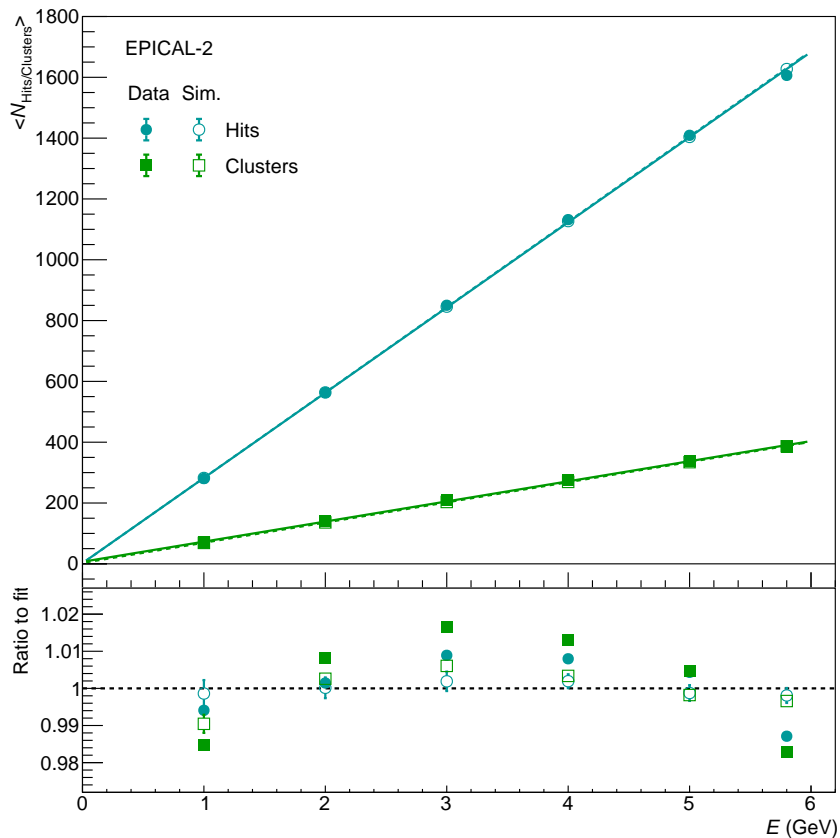


Figure 6.29: Top: Relationship between the energy of the incoming beam, and the resulting $\langle N_{Hits} \rangle$ and $\langle N_{Clus} \rangle$ values extracted from data and simulations. Bottom: Ratio between the fitted linear function for each configuration of data/sims and hits/clusters, and the values of $\langle N_{Hits} \rangle / \langle N_{Clus} \rangle$.

The mean values extracted from the Gaussian fits are shown in Figure 6.29. A linear fit was performed for each configuration and is also depicted, together with the ratio of data and the fit.

From the plot of the residuals, there appears to be a significant non-linearity in the distributions of N_{Clus} , particularly in the case of the data. This non-linearity is also reflected in the N_{Hits} distributions to a lesser extent. However, as will be seen in Section 6.8, there is little evidence to show that significant saturation occurred.

There is an uncertainty upon the momentum of the DESY II beam of $\sigma_p = 158$ MeV for comparatively narrow collimator settings, using 6.4 mm primary collimator and 8 mm secondary collimator widths, respectively [72]. The data taking in February 2020 used wider collimator settings, and so it is expected that the uncertainty upon

Table 6.10: Comparison of nominal momentum p_0 at the TB22 test beam and the corresponding mean momentum p_{eff} measured at TB21 [72, 82]. Statistical uncertainties are expected to be negligible for p_{eff} .

p_0 (GeV/c)	p_{eff} (GeV/c)
1.0	1.119
2.0	2.045
3.0	3.026
4.0	4.016
5.0	4.989
5.6	5.560

the beam momentum should be at least this large. Measurements of the deflection angle of particles traversing the DESY II TB21 dipole magnets also showed small discrepancies between the momentum set to the magnets and the mean momentum measured in the beam. The effective momenta are shown in Table 6.10.

Using these effective beam momenta to apply asymmetric systematic uncertainties to the data points substantially improves the linearity, as is shown in Figure 6.30. However, at high energies a small but significant non-linearity remains, suggesting that either some unknown source of non-linearity remains present in the data or that the values of p_{eff} are not fully representative of the ‘true’ energy of the beam particles, which might be compounded by the addition of beam momentum spread, which is discussed in Section 6.7.2 below.

6.7.2 Resolution

The Gaussian fits applied to the N_{Hits} distributions in Figure 6.27 over the limited fit ranges defined in Eq. 6.7 were also used for the extraction of the energy resolution, which is shown in Figure 6.31.

Each configuration is fitted using the general ECAL resolution parameterisation defined in Eq. 3.9, with the exception of the CALICE prototype where the parameterisation of the resolution is taken directly from [83]. The resulting parameterisations

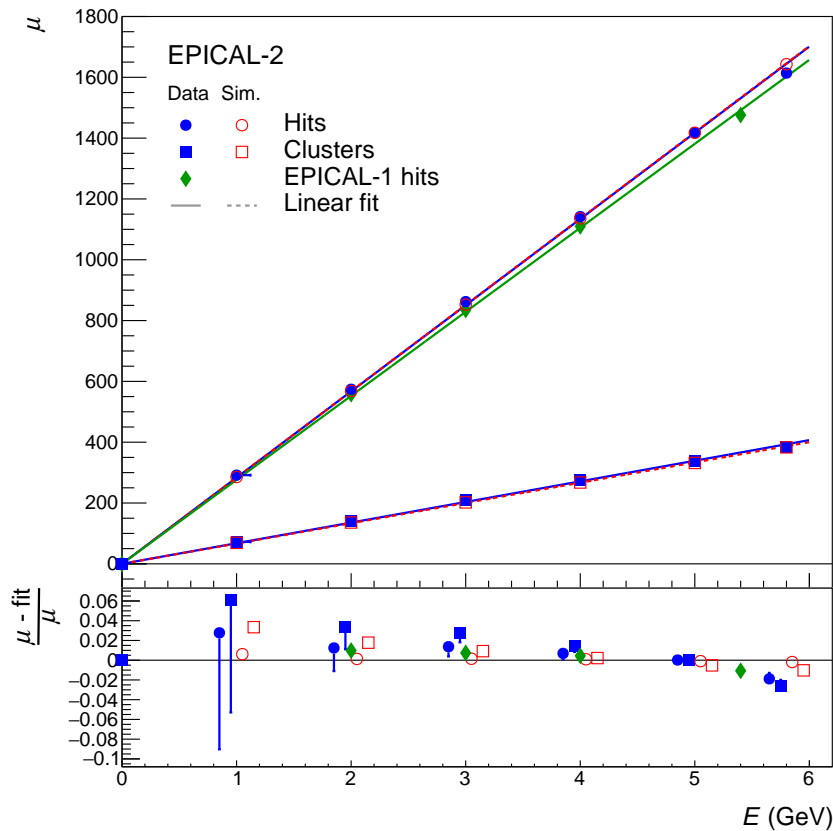


Figure 6.30: Top: Relationship between the energy of the incoming beam, and the resulting $\langle N_{Hits} \rangle$ and $\langle N_{Clus} \rangle$ values extracted from data and simulations, with one-sided asymmetric systematic uncertainties applied to data matching the difference between p_0 and p_{eff} in Table 6.10. The datapoints from the EPICAL-1 prototype are also added, with no corresponding uncertainty shown. Bottom: Relative difference between the fitted linear function for each configuration of data/sims and hits/clusters, and the values of $\langle N_{Hits} \rangle / \langle N_{Clus} \rangle$. Horizontal displacement at each energy is for clarity, p_0 was used rather than p_{eff} for all datasets. Taken from [78].

are shown in Table 6.11. The effect of applying the clustering algorithm is apparent; small variations in the number of pixel hits per particle are suppressed, and so the width of the distribution is reduced and the resolution improves significantly. It is particularly notable that the EPICAL-2 resolution using clusters is very competitive with the comparable CALICE AECAL physics prototype.

The resolutions from simulating EPICAL-2 are significantly better than the equivalent resolutions in data. While the simulations do include per-pixel electronic noise, threshold smearing and a pixel mask, they still represent a more ideal version of EPICAL-2 than in reality. Particularly, no chip-by-chip calibration is necessary in

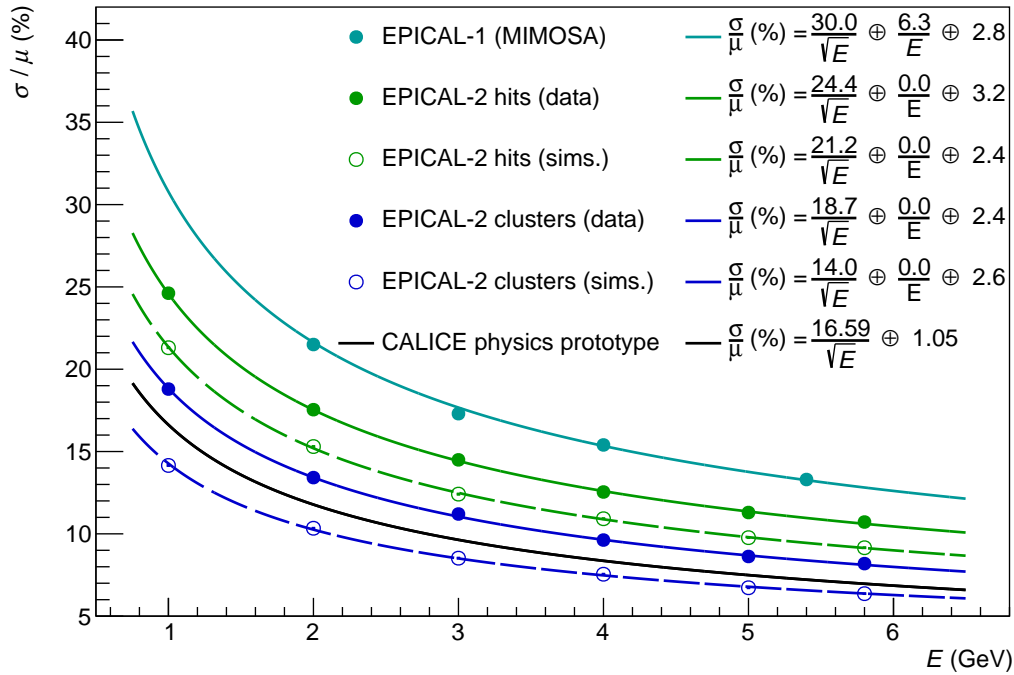


Figure 6.31: Comparison of the resolution of the EPICAL-1 prototype [67] and the CALICE AECAL physics prototype [83] with the EPICAL-2 resolution extracted from the N_{Hits} and N_{Clus} distributions, both for data and simulations.

Table 6.11: Summary of the parameterisation of energy resolutions found using hits or clusters, for DESY II data or for Allpix² simulations.

$\sigma/\mu(\%)$	N_{Hits}	N_{Clus}
Data	$24.4/\sqrt{E} \oplus 3.2$	$18.7/\sqrt{E} \oplus 2.4$
Simulations	$21.2/\sqrt{E} \oplus 2.4$	$14.0/\sqrt{E} \oplus 2.6$

simulations as each chip is configured to have the same threshold across each chip. The lack of a requirement for alignment adjustments may play a small further role in the improved resolution in simulations.

Additionally, for simulated data the beam momentum is known absolutely, and so only the intrinsic detector resolution is measured. For the results obtained from data the quoted performance represents a convolution of the intrinsic detector performance and the uncertainty upon the beam conditions, and as such the results from data underestimate the performance. The addition of a constant momentum spread to Allpix² simulations in order to achieve better alignment between simulations and data is shown in Figure 6.32. Neither the simulations in the presence or

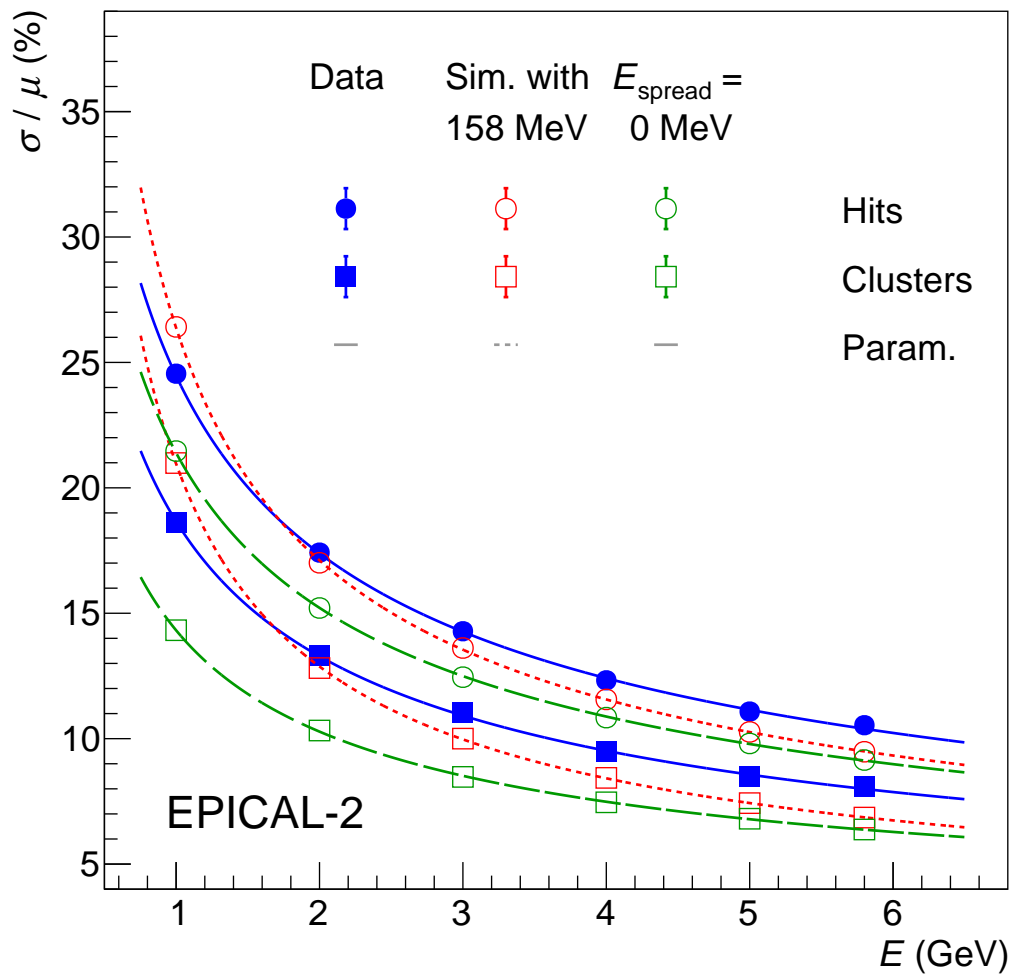


Figure 6.32: Comparison of the resolution of the EPICAL-2 prototype derived from data with that derived from two sets of simulations, one with no modeled spread in the beam momentum and one with a momentum spread of 158 MeV. Taken from [78].

absence of constant momentum spread fully describe the resolution as measured in the data, suggesting that while the momentum spread of the beam has a significant non-zero effect upon the resolution, it varies significantly with the nominal beam energy. The resolution as measured in the data should therefore be seen as an upper limit upon the intrinsic resolution of the EPICAL-2 prototype [78].

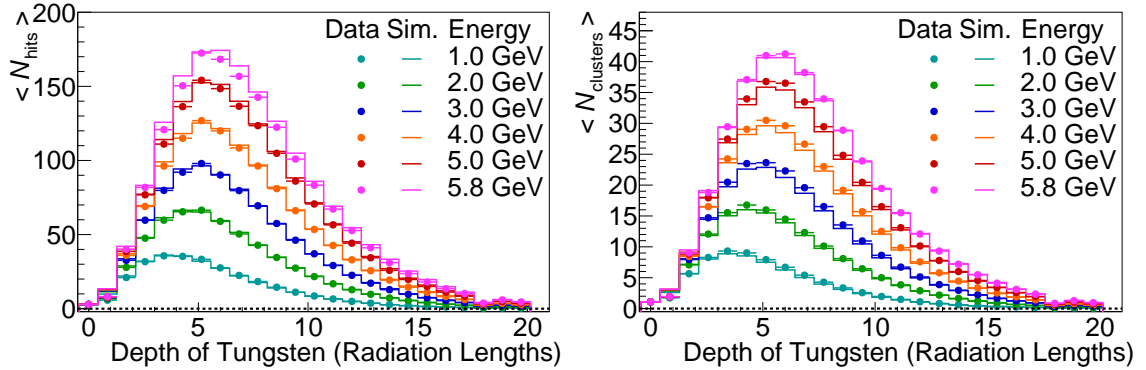


Figure 6.33: Longitudinal profiles of EPICAL-2 using hits (left) and clusters (right), both with data from the February 2020 DESY II data-taking run and Allpix² simulations overlaid.

6.7.3 Longitudinal Profile

The longitudinal profile, which is defined as the mean response (either N_{Hits} or N_{Clus}) of the prototype on a per-layer basis, is depicted in Figure 6.33. There is a clear reduction in both contributions at Layer 21, which shows that the effect of removing the chip in that layer is small in all cases. One can see that the shower maximum starts low, and increases as the beam energy increases. This is represented in Table 6.12, which shows the maxima of simplified longitudinal profile functions (see Eq. 3.4) which were fitted to the longitudinal profiles. The form of the fits applied is shown in Eq. 6.8 below, in which z is the depth of hits in each layer and $a_{0,1,2}$ are parameters of the fit.

$$\langle N_{Hits,z} \rangle = a_0 z^{a_1} e^{-a_2 z} \quad (6.8)$$

The results of the longitudinal profile fits are shown in Figure 6.34.

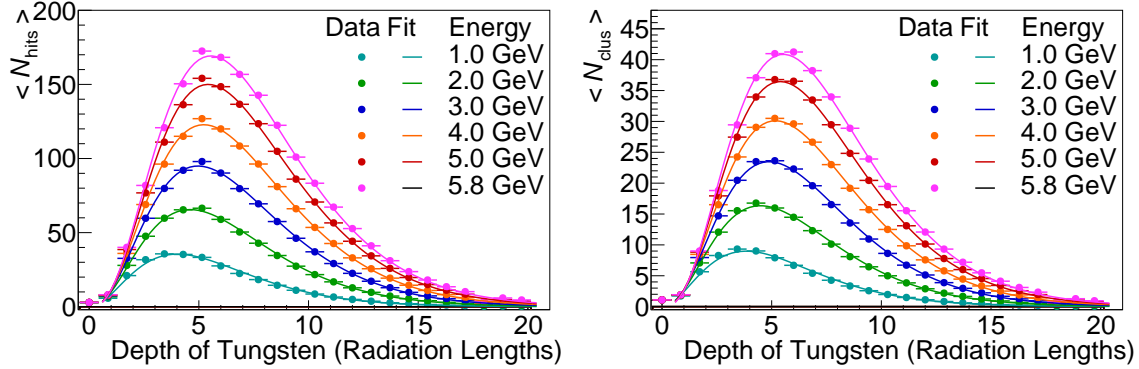


Figure 6.34: Longitudinal profiles of EPICAL-2 using hits (left) and clusters (right) using data from the February 2020 DESY II data-taking run, with fits of the form defined in Eq. 6.8 overlaid.

Table 6.12: The shower maxima of longitudinal profile functions fitted to the longitudinal profiles in Figure 6.33. The errors displayed are derived statistically.

Energy (GeV)	Shower Maximum (χ_0)			
	Data		Simulations	
	Hits	Clusters	Hits	Clusters
1	4.014 ± 0.005	3.834 ± 0.004	3.686 ± 0.002	3.527 ± 0.001
2	4.600 ± 0.005	4.489 ± 0.004	4.412 ± 0.001	4.290 ± 0.001
3	4.959 ± 0.004	4.882 ± 0.003	4.828 ± 0.001	4.730 ± 0.001
4	5.225 ± 0.003	5.174 ± 0.003	5.125 ± 0.001	5.050 ± 0.001
5	5.425 ± 0.002	5.393 ± 0.002	5.356 ± 0.001	5.299 ± 0.001
5.8	5.548 ± 0.003	5.527 ± 0.002	5.505 ± 0.001	5.458 ± 0.001

One can see significant differences in the maxima between data and simulations, both across hits and clusters, despite there being few differences between the linearity plots. While it is possible that this difference is reflective of differences in showering behaviour in the simulations compared to reality, it is also possible that the smearing caused by the beam momentum (see Section 6.7.1) has contributed to this difference. However, there is a constant drop in the shower maximum for data compared to simulations, which is not reflected in the effective momenta in Table 6.10. There are also significant differences between clusters and hits, which is not expected: the number of clusters should be approximately proportional to the number of hits, unless saturation is occurring (i.e. clusters are being merged) which is biasing the N_{Clus} distributions.

6.8 Lateral Profile

The longitudinal profiles shown in Section 6.7.3 are the most typical way of characterising shower development in an ECAL, and are particularly illustrative of the point at which the critical energy of the shower E_c (see Section 3.2.1) is reached, which by construction should be at the shower maximum. However, also particularly relevant in the DECAL case is the evolution of the shower laterally. Computing the lateral profile of EPICAL-2 allows a direct examination of potential saturation close to the shower centre, and sets the stage for parameterising the transverse shower shape, which is an important ingredient towards an improved PFA implementation for a DECAL.

6.8.1 Determination of Shower Axis

In order to compute the relationship between the radius around the shower axis and the pixel hit density, it is first necessary to determine the shower axis reliably. Although ideally the particle beam is expected to be perpendicular to the detector face, in reality there are likely to be small differences in primary particle trajectory. These could be the result of beam-beam interactions or the intrinsic spread of the particle beam. Several methods of per-event axis determination were considered, which are listed in the subsections below.

6.8.1.1 Perpendicular

The Perpendicular method is the simplest and computationally quickest. It involves taking the beam position determined by the event selection (the Jet-Finding algorithm was used), and presuming that the beam is parallel to the z axis without any further analysis of the data.

6.8.1.2 Perpendicular With Search

The Perpendicular With Search (PWS) method also presumes that the beam is parallel to the z axis. The lateral position of the beam is determined by the following steps:

- Find the centre-of-gravity of hits in layers 3 and 4 using:

$$(\langle x \rangle, \langle y \rangle)_{3,4} = \frac{\sum_i^N (x_i, y_i)}{N}. \quad (6.9)$$

- Reduce the search area and recalculate the centre-of-gravity of hits in Layers 3 and 4 iteratively. The search area for each Layer l is defined as a circle of radius r_l , which is determined for each iteration n via

$$r_l = (l - n + 3)\text{mm}, \quad (6.10)$$

which iterates until $r_l = 1$ for each layer.

- Calculate the approximate shower position as the mean of the centres-of-gravity in Layers 3 and 4, i.e.

$$(x, y)_{\text{approx.}} = 0.5 \times \sum_{i=3}^4 (\langle x \rangle, \langle y \rangle_i). \quad (6.11)$$

- Search Layer 0 for hits within a 1 mm radius of $(x, y)_{\text{approx.}}$. If none are found, this event is skipped. Likewise, if more than 12 hits are found within the radius, the event is skipped.
- The centre-of-gravity of the Layer 0 cluster which has cluster position closest to $(x, y)_{\text{approx.}}$ is used as the final shower position.

The PWS method was developed for use in the lateral profiles of EPICAL-1 [84].

6.8.1.3 2-D Fit of Means

The Two Dimensional Fit of Means (2DFM) method proceeds as follows:

- For each layer l , compute the mean and standard error of hit positions in x and y .
- Perform a 2D linear fit of mean x positions to determine the gradient of the shower m_x in the xz plane, weighted by the standard error of each x position. The fit is constrained to pass through the incident beam position in Layer 0 determined by the event selection x_0 . The fit range used was $0 \leq l \leq 7$.
- Perform a 2D linear fit of mean y positions to determine the gradient of the shower m_y in the yz plane, weighted by the standard error of each y position. This fit is constrained to pass through the incident beam position in layer 0 determined by the event selection y_0 . The fit range used was $0 \leq l \leq 7$.
- The position of the beam in each layer is determined from the gradients and layer 0 positions independently:

$$x_l = x_0 + lm_x \tag{6.12}$$

$$y_l = y_0 + lm_y \tag{6.13}$$

6.8.1.4 3-D Fit of Means

The Three Dimensional Fit of Means (3DFM) method proceeds as follows:

- For each Layer l , compute the mean and standard error of hit positions in x and y .
- Perform a 3D linear fit of mean (x, y) positions, weighted by the standard error of each position. The fit range used was $0 \leq l \leq 7$.

This method was developed as an upgrade to the 2DFM method, wrapping the two fits of x and y into a single fit. The weighting of the fit by the standard error of each mean position was designed to give additional weight to the early layers, where there would be few hits in a small region and so the standard error would be smaller.

6.8.1.5 3-D Fit of Pixels

The Three Dimensional Fit of Pixels (3DFP) method simply uses an unweighted 3D linear fit over the positions of all pixels in Layers l within the fit range, $0 \leq l \leq 7$. This method was developed as an alternative to the 3DFM method, with the fear that the weighting of fits to mean positions by the standard error would cause some fits to deviate. This could occur in events where, as a consequence of the randomness of shower development, one of the early layers contained only one cluster. By performing an unweighted fit of the pixel positions, this effect might be mitigated. However, one loses the benefit of weighting the early layers first.

6.8.1.6 Evaluation of Axis-Finding Methods

The criteria for the ideal axis-finding method are that the radial distribution of pixels in each layer should be skewed towards small radii as much as possible (i.e. more pixels are located close to the shower axis), with particular emphasis on upstream layers in the detector.

The radial distributions of hits around axes found by all methods are shown in Figure 6.35, Figure 6.36, Figure 6.37 and Figure 6.38. It is clear from these figures that for the earliest layers the Perpendicular and PWS are by far preferable, with a large peak on the left which is gradually smeared as the layer number increases, as statistical fluctuations begin to dominate within the shower. The 3DFP method performed exceptionally poorly in early layers, which is likely to be because the hits in early layers have comparatively little weight compared to the hits at and around the shower maximum. The 3DFM and 2DFM methods also perform poorly in early

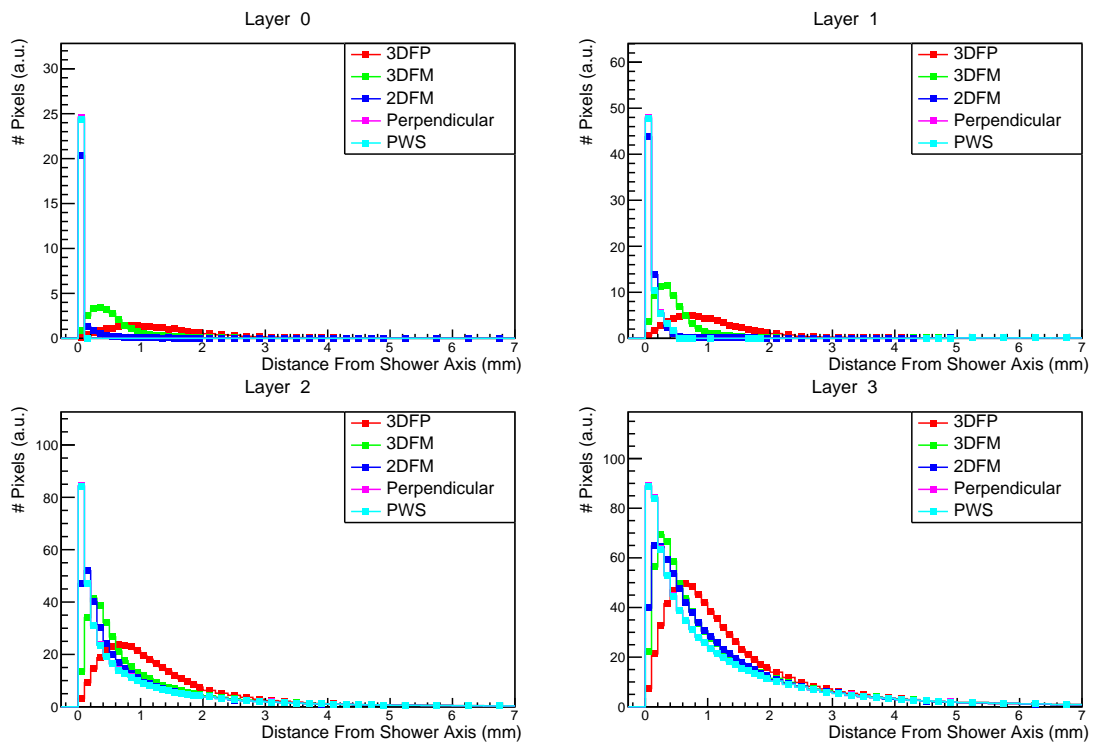


Figure 6.35: Distributions of the average number of pixel hits within annular regions around the shower axis, as determined by a variety of methods, for EPICAL-2 Layers 0–4. The 5 GeV data from February 2020 are used in these distributions. The sawtooth-like jumps as 2 mm and 5 mm are the result of wider binning in these regions to make the differences between axis-fitting methods more visible.

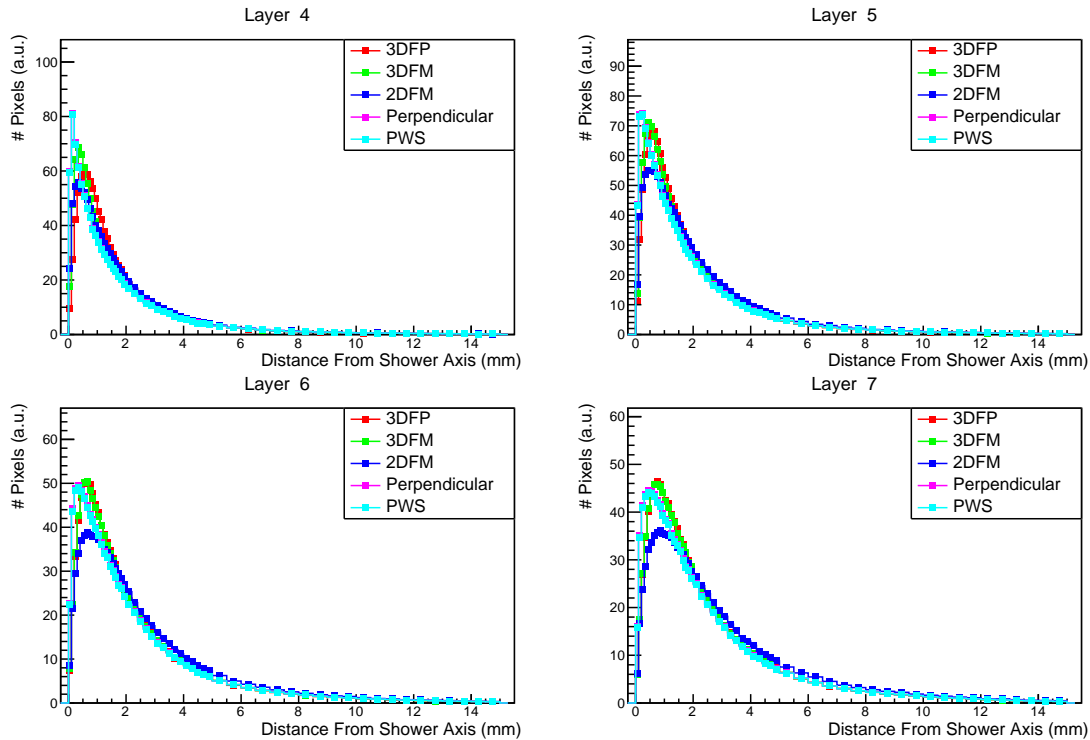


Figure 6.36: Distributions of the average number of pixel hits within annular regions around the shower axis, as determined by a variety of methods, for EPICAL-2 layers 5–8. The 5 GeV data from February 2020 are used in these distributions.

layers. By contrast, the Perpendicular and PWS methods perform well, with sharp peaks to the left of the distribution and a smaller tail toward the right side.

The trend of axis-finding methods continues even into the latest layers. The Perpendicular and PWS methods give almost indistinguishable results, which is likely to be because the PWS method essentially performs some extra event selection which ends up finding the same Layer 0 cluster as the original event selection. By comparison, the 2DFM, 3DFM and 3DFP methods all perform worse, with peaks in the Landau-like shape which form later than their non-fitted counterparts, and significantly larger tails. It is concluded therefore that fluctuations in the shower shape on an event-by-event basis, such as large clusters caused by a single shower particle, end up skewing the fits of the three fitted methods. Since there is very little difference between the results of the PWS and Perpendicular methods, the Perpendicular method is selected for use due to its computational speed and simplicity.

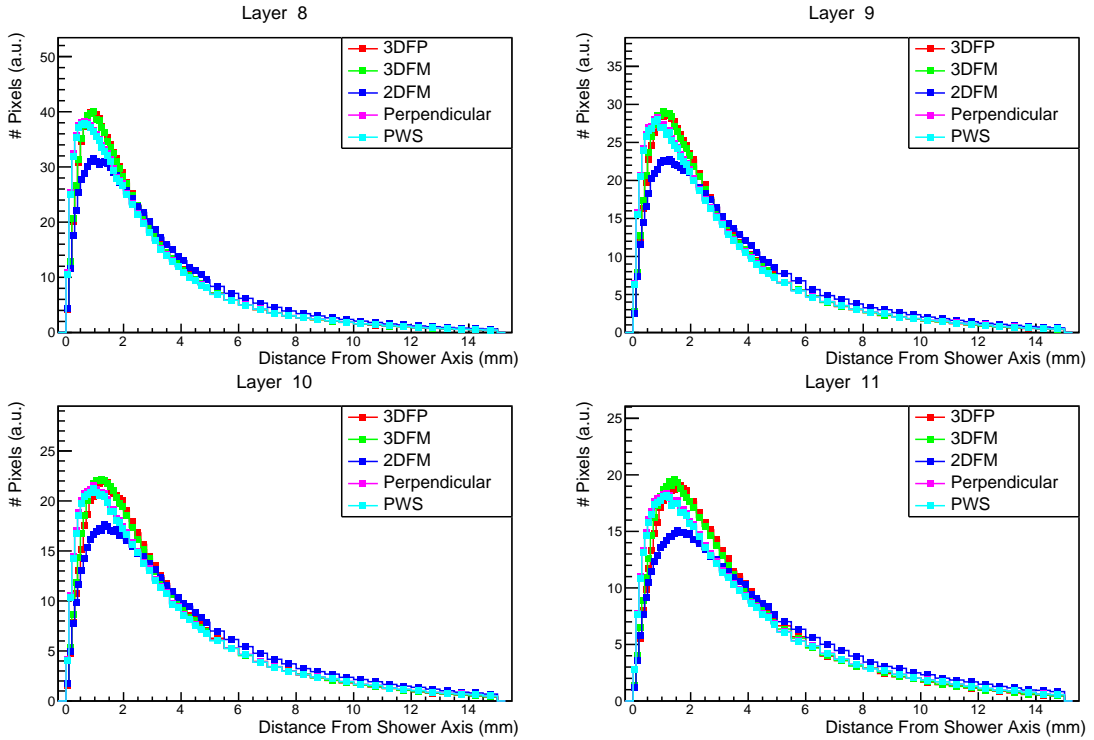


Figure 6.37: Distributions of the average number of pixel hits within annular regions around the shower axis, as determined by a variety of methods, for EPICAL-2 Layers 9–12. The 5 GeV data from February 2020 are used in these distributions.

6.8.2 Determination of Annulus Area

In order to analyse the extent of saturation, it is necessary to compute the hit density within the annuli considered in the lateral profiles, rather than simply the average number of hits within those annuli. As such, it is important to determine the area of each annulus, so that the hit density can be computed via $\rho = \frac{N_{Hits, Ring}}{A_{Ring}}$. The generic equation for the area A_{Ring} of an annulus is:

$$A_{ring}(r_1, r_2) = \pi dr(r_1 + r_2), \quad (6.14)$$

where r_1 and r_2 are the inner and outer radii of the annulus and $dr = r_2 - r_1$. Events passing the event selection are located centrally, negating the need to account for the edges of the detector by only considering events which are likely to be fully contained by the lateral extent of the prototype. However, the insensitive region subtended by the 100 μm gap between the chips in each layer must be accounted

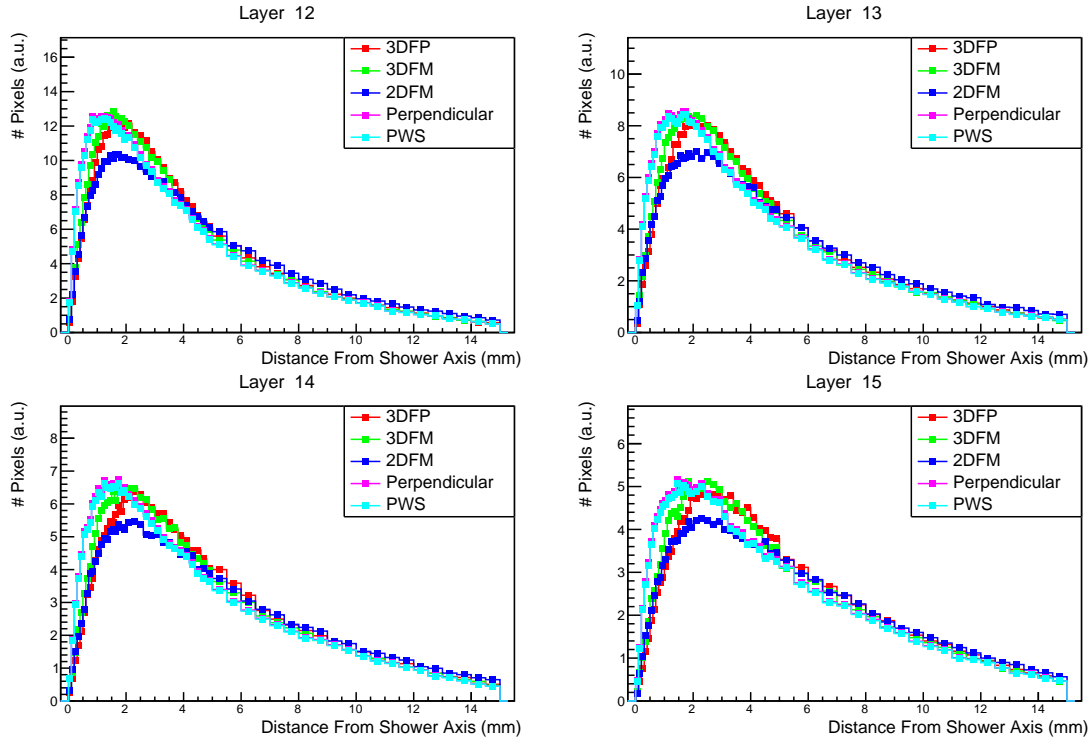


Figure 6.38: Distributions of the average number of pixel hits within annular regions around the shower axis, as determined by a variety of methods, for EPICAL-2 Layers 13–16. The 5 GeV data from February 2020 are used in these distributions.

for. A general formula for the total area of a ring centred on (\bar{x}, \bar{y}) with inner radius r_1 and outer radius r_2 , with the dead space subtended between the left side y_1 and the right side y_2 was developed, which is detailed in Eq. 6.15. The parameters used in the computation of the total area are shown diagrammatically in Figure 6.39.

$$A_{tot} = \beta A_{ring} + \sum_{n=1}^2 \sum_{m=1}^2 \alpha_{nm} A_{nm}. \quad (6.15)$$

In Eq. 6.15, β is defined by:

$$\beta(y_1, y_2) = \begin{cases} 0 & dy_1 < 0 < dy_2 \\ 1 & \text{otherwise,} \end{cases} \quad (6.16)$$

where $dy_n = y_n - \bar{y}$. β is used to define whether or not to add the ring area defined in Eq. 6.14 to the total. If the centre of the annulus lies inside the insensitive region, the ring area is not included (and the area of each half is added separately instead),

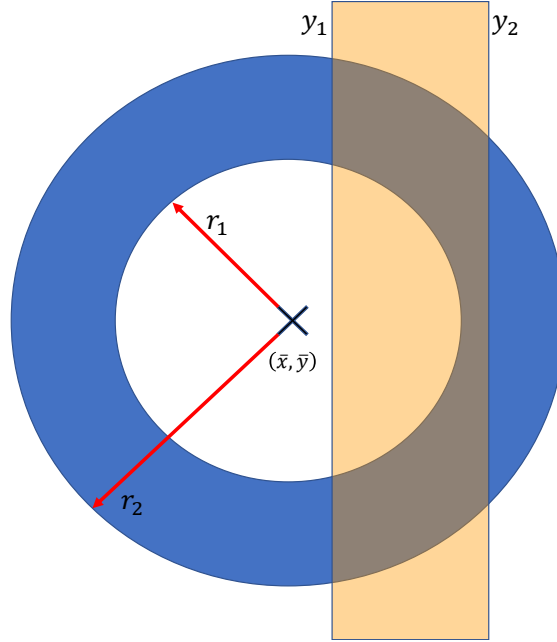


Figure 6.39: Diagram of the variables used in the computation of the total area, with the annulus of radii $r_{1,2}$ centred on (\bar{x}, \bar{y}) and the insensitive area to be removed subtended by $y_{1,2}$.

otherwise the ring area is added and the insensitive region subtracted.

A_{nm} is the area of the circle segment subtended by radius r_m and dead space edge y_n , as described by:

$$A_{nm}(y_n, r_m) = r_m^2 \frac{\theta_{nm} - \sin(\theta_{nm})}{2} \quad (6.17)$$

$$\theta_{nm}(y_n, r_m) = 2 \cos^{-1} \left(\frac{|dx_n|}{r_m} \right). \quad (6.18)$$

Here, α_{nm} is equal to 1, 0, or -1 , and determines whether or not to add, subtract, or ignore the area given by A_{nm} , as described by:

$$\alpha_{nm}(n, m, y_n, r_m) = f_n f_m g_{nm} \quad (6.19)$$

$$f_n(n) = \begin{cases} -1 & n = 1 \\ 1 & n = 2 \end{cases} \quad (6.20)$$

$$f_m(m) = \begin{cases} -1 & m = 1 \\ 1 & m = 2 \end{cases} \quad (6.21)$$

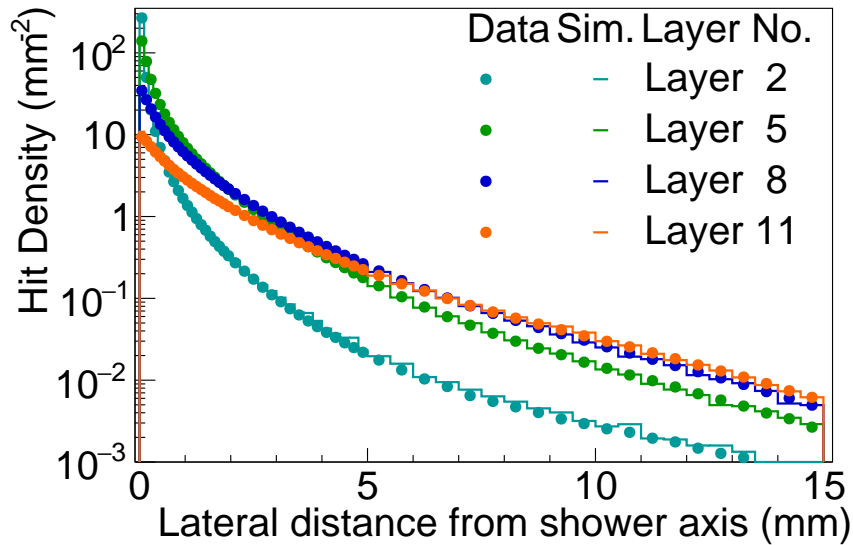


Figure 6.40: Lateral Profiles for the 5 GeV data recorded at the February 2020 test beam and simulations of 5 GeV electrons using Allpix², across a variety of shower depths representing several stages of shower development.

$$g_{nm}(x_n, r_m) = \begin{cases} 0 & |dx_n| \geq r_m \\ 1 & 0 \leq dx_n < r_m \\ -1 & -r_m < dx_n < 0 \end{cases} \quad (6.22)$$

6.8.3 Lateral Profile Results

The lateral profiles for several layers are shown in Figure 6.40. The layers depicted represent several stages in shower development. Layer 2 represents early shower development, and also represents the layer with the largest maximum hit density at ≈ 300 hits/mm². Complete saturation for EPICAL-2 occurs at 1272 hits/mm², so at the greatest density of hits in EPICAL-2 only $\frac{1}{4}$ of pixels are returning a signal, indicating that significant saturation is unlikely. Layer 5 represents the approximate shower maximum: while the maximum hit density is smaller than that in Layer 2 due to the greater dispersion of the shower, the number of hits is far greater, which is reflected in the much larger integral underneath the hit density. Layers 8 and 11 represent the early and late development of the tail of the shower, in which the

density distribution continues to flatten considerably.

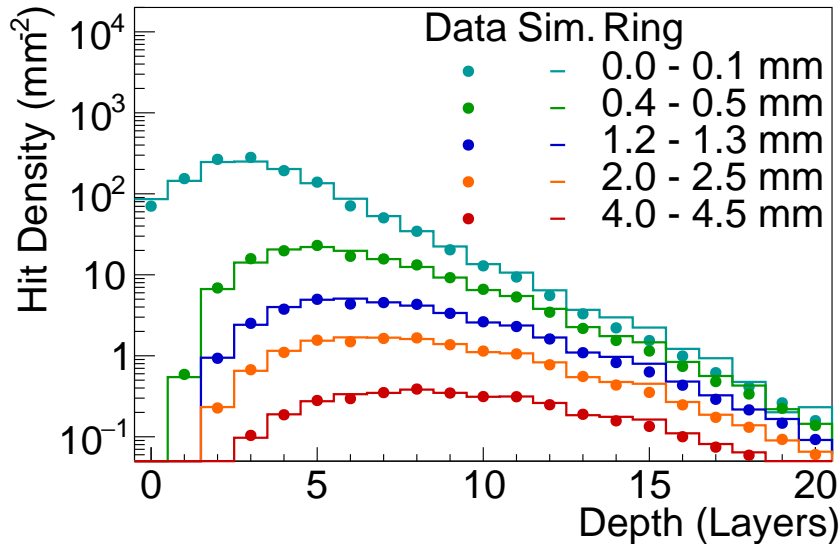


Figure 6.41: Longitudinal profiles of the hit density for a selection of annular regions about the shower axis for the 5 GeV data recorded at the February 2020 test beam and simulations of 5 GeV electrons using Allpix².

Additionally, longitudinal profiles for a variety of annular regions are shown in Figure 6.41. These results show that the maximum hit density for each annulus occurs at progressively later stages of shower development for increasing radius. Additionally, it is evident that more central annuli maintain a constant average hit density than those at larger radii, although toward the latter half of the detector the difference becomes much less significant as the shower disperses.

The per-layer lateral profiles in Figure 6.40 show generally excellent agreement between simulation and data at 5 GeV. The agreement in longitudinal hit density profiles in Figure 6.41 is generally good, although generally the simulations are slightly more left-skewed than the data. This reflects the overall trend of the longitudinal profile in Figure 6.33.

6.9 Forward-Backward Asymmetry

6.9.1 Motivation

The Forward-Backward Asymmetry (FBA) studies were originally motivated by the small apparent non-linearity of both simulations and data shown in Figure 6.29, and the apparent additional non-linearity introduced by using clusters rather than hits. The idea was that if a bias in the cluster size was introduced by differing chip thresholds which were not fully accounted for by the chip corrections in Section 6.5.2 then this should be visible in the evolution of the cluster size for data taken both in the forward and backward direction for like layers.

6.9.2 Asymmetry in Data and Simulations

In order to remove chip-by-chip variation in the threshold, which has a significant impact upon the cluster size, the relative difference in the mean cluster size s (i.e. the mean number of pixels in each cluster) between the beam-forward data F and beam-backward data B for each chip c was computed:

$$A_c^{FB}(s) = \frac{s_c^F - s_c^B}{s_c^F + s_c^B} \quad (6.23)$$

The graph of $A_c^{FB}(s)$ is shown in Figure 6.42. It is clear that there is a strong trend for the cluster size to vary with the shower activity; there is a trough at approximately Layer 5, and a peak at approximately Layer 19. It is also notable that at the midpoint of the detector, where one would expect $A_c^{FB}(s) = 0$ if there were no bias introduced by reversing the detector since there is an approximately equal depth in radiation lengths either side of the chips in Layer 12, a small but significant asymmetry is found. This indicates that there is some effect causing the average cluster size to be smaller when the beam is entering the detector forwards

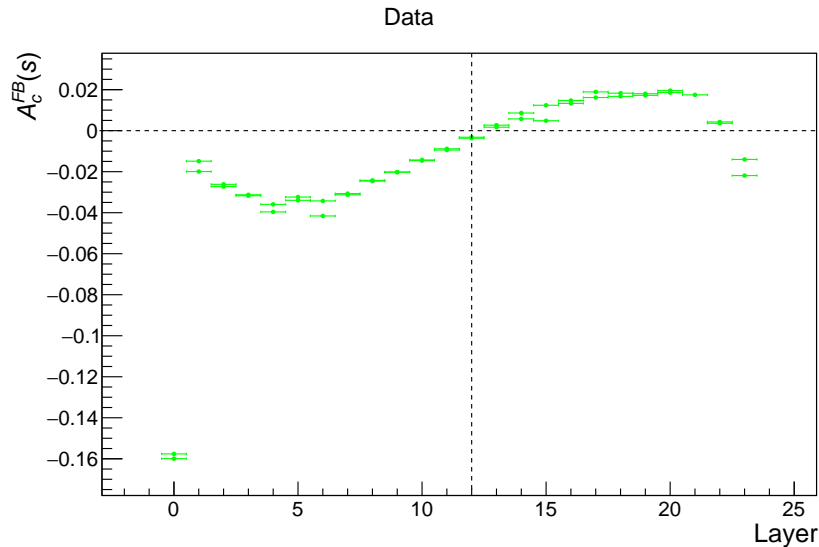


Figure 6.42: Graph of $A_c^{FB}(s)$ (the relative difference in mean cluster size between beam-forward and beam-backward runs) for every chip used in data taking at DESY II during February 2020 at 5 GeV. The horizontal dashed line shows the point at which there is no asymmetry in mean cluster size, and the vertical dashed line shows the position in the detector at which there is an equal depth of tungsten both upstream and downstream. The two data points for each layer correspond to the two chips in each layer.

compared to when the beam enters backwards.

Figure 6.43 shows the likewise distribution of $A_c^{FB}(s)$ for 5 GeV simulations using Allpix². While there are small quantitative differences in the asymmetry distributions between data and simulations, the qualitative result is the same: the asymmetry peaks at approximately the shower maximum, and there is a significant asymmetry at the midpoint of the detector. As the simulation provides a very good description of the data, its use to explore the origin of this effect is appropriate.

The confirmation of this asymmetry in simulations is particularly useful because there is no simulated variation in the threshold between chips, hence different chips can be directly compared. A new asymmetry metric $A_z^{FB}(s)$ was defined to compare chips at the same depth z in radiation lengths (using $z_{\max} = 24 \times \frac{3.0 \text{ mm}}{3.5 \text{ mm}} \approx 20.57$ is the approximate depth of the full prototype in radiation lengths):

$$A_z^{FB}(s) = \frac{s_z^F - s_{z_{\max}-z}^B}{s_z^F + s_{z_{\max}-z}^B} \quad (6.24)$$

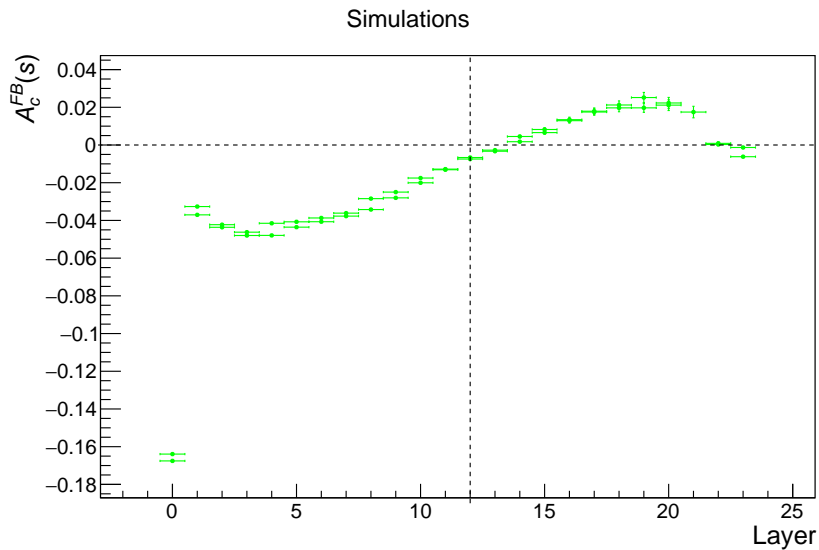


Figure 6.43: Graph of $A_c^{FB}(s)$ (the relative difference in mean cluster size between beam-forward and beam-backward runs) for every chip in Allpix² simulations of EPICAL-2 at 5 GeV. The horizontal dashed line shows the point at which there is no asymmetry in mean cluster size, and the vertical dashed line shows the position in the detector at which there is an equal depth of tungsten both upstream and downstream. The two data points for each layer correspond to the two chips in each layer.

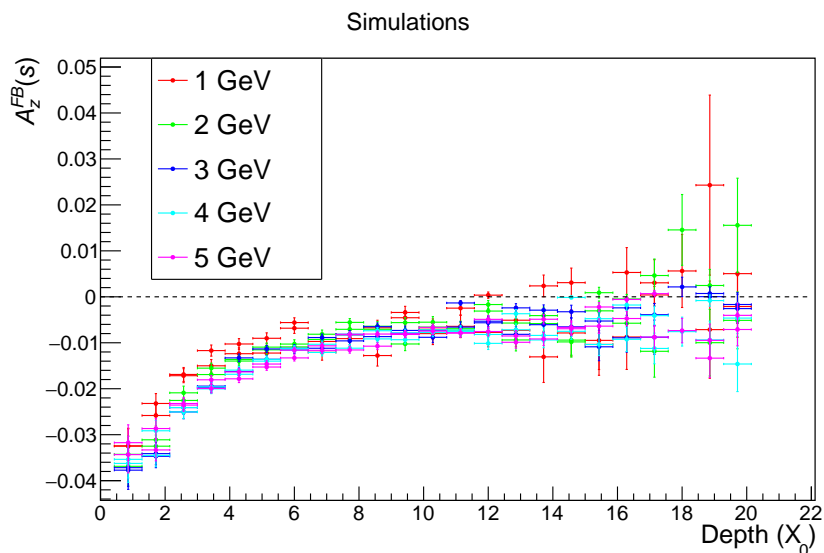


Figure 6.44: Graph of $A_z^{FB}(s)$ (the relative difference in mean cluster size between beam-forward and beam-backward runs) for chips of like depths on like sides of the prototype in Allpix² simulations of EPICAL-2 at 5 GeV. The horizontal dashed line shows the point at which there is no asymmetry in mean cluster size.

As an example, the mean cluster size in the left-side chip in Layer 1 using beam-forward simulations would be compared to the mean cluster size in the left-side chip in Layer 23, since each has 3 mm ($\frac{6}{7}X_0$) depth of tungsten upstream. Layer 0 is not considered since there is no equivalent layer at the rear of the detector with no tungsten on the rear side.

The distribution of $A_z^{FB}(s)$ for a wide range of simulated electron energies is shown in Figure 6.44. It is clear that the largest asymmetry occurs at early shower development, which plateaus at close to the shower maximum to a value slightly below zero. Since there is no variation in chip threshold in simulations, the inference drawn was that some feature of the geometry of each layer was causing the difference in cluster size, and that this effect must be influencing electrons/positrons in the EM shower in some way since it is more severe for early layers when the shower has a larger leptonic component.

To eliminate the possibility of bias by the clustering algorithm, a forward-backward asymmetry metric using N_{Hits} was also examined, defined by:

$$A_z^{FB}(N_{Hits}) = \frac{N_{Hits,z}^F - N_{Hits,z_{\max}-z}^B}{N_{Hits,z}^F + N_{Hits,z_{\max}-z}^B} \quad (6.25)$$

which is shown in Figure 6.45. The opposite trend to that found in comparing cluster sizes is found: there are more pixel hits for beam-forward simulations in early layers, which plateaus at close to the shower maximum.

6.9.3 Diagnosing Asymmetry using Simulations

In order to diagnose the cause of the asymmetry in Figure 6.44 and Figure 6.45 the 24-layer Allpix² geometry implementation of EPICAL-2 was simplified to a single layer of silicon, with chip and flex cables included, surrounded by two absorber blocks of tungsten. Three geometry configurations were considered in order to determine the cause of the asymmetry, which are shown in Figure 6.46, as detailed below:

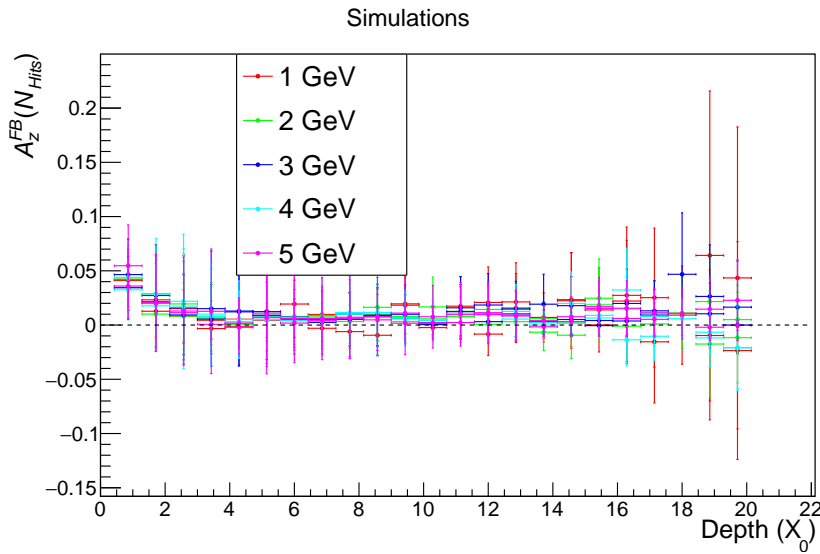


Figure 6.45: Graph of $A_z^{FB}(N_{Hits})$ (the relative difference in mean number of hits between beam-forward and beam-backward runs) for chips of like depths on like sides of the prototype in Allpix² simulations of EPICAL-2 at 5 GeV. The horizontal dashed line shows the point at which there is no asymmetry in mean cluster size.

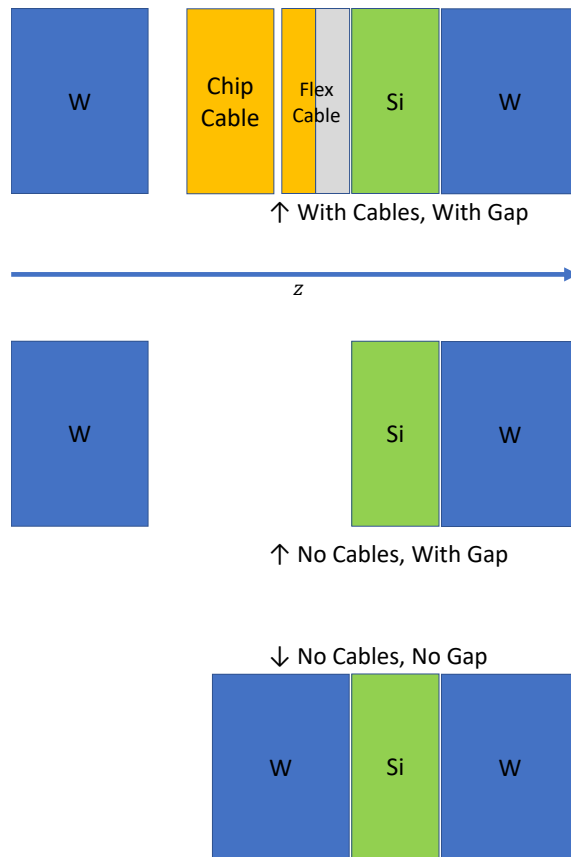


Figure 6.46: Representative diagrams of the single-layer geometry configurations used in diagnosis simulations in Allpix².

Table 6.13: The arithmetic means of the N_{Hits} distributions produced by 5 GeV electrons for all single-layer geometry configurations.

Geometry Configuration	N_{Hits}	
	Beam-forwards	Beam-backwards
WCWG	12.219 ± 0.088	11.039 ± 0.084
NCWG	12.339 ± 0.093	11.520 ± 0.088
NCNG	11.560 ± 0.091	11.496 ± 0.089

- The With Cables With Gap (WCWG) configuration uses the full geometry implementation of a single layer, with an additional 3 mm tungsten block added to the front at the same position as it would have been if another layer were placed upstream, so that the gaps between elements remain the same as in the original 24-layer configuration.
- The No Cables With Gap (NCWG) configuration removes the flex cables and chip cables from WCWG, leaving just the silicon ALPIDE between two blocks of tungsten and a ≈ 5 mm air gap between the upstream tungsten and the silicon.
- The No Cables No Gap (NCNG) configuration takes the upstream tungsten block from NCWG and shunts it forwards, so that there is an equal air gap between each tungsten block and the edges of the silicon. The only geometric asymmetry in this configuration is the location of the collection diodes and the electric field applied to the silicon.

A total of 4×10^5 5 GeV single-electron events were simulated for each single-layer geometry configuration, divided equally between beam-forward and beam-backward runs. The arithmetic means of the resulting N_{Hits} distributions are displayed in Table 6.13. Two notable inferences can be made from these results. First, from the right-most column it is clear that the removal of the air gap has a significant effect upon the number of hits. This is likely a result of the angular dispersion of leptons in the EM shower - while the shower traverses the air gap in the NCWG configuration the leptons contained therein spread out, resulting in less chance of clusters overlapping which increases the number of hits and reduces the average

cluster size by helping ensure that clusters from two particles do not get merged into one large cluster. Indeed, once the gap is removed for the NCNG configuration, the number of beam-forward hits is reduced to within a reasonable proximity of the beam-backward level.

The second significant result is the difference between mean N_{Hits} for the beam-backward WCWG and NCWG configurations: the removal of the cabling causes a significant increase in the number of hits. It is inferred from this difference that cables provide sufficient material to screen out some low-energy leptons which are back-scattered by the tungsten.

6.10 Conclusions

The performance of EPICAL-2, a 24-layer DECAL prototype utilising 48 ALPIDE sensors sandwiched between 3 mm blocks of tungsten, when tested using an electron beam of between 1 GeV and 5.8 GeV at the DESY II facility has been examined. The experimental setup of the beam tests was detailed, with particular emphasis on the data-taking with the full EPICAL-2 prototype in February 2020.

In order to ensure the good quality of the data taken during test beam runs in the absence of a live DQM system, a simple event display based on the CED package was developed in order to examine the shower shape of individual events directly. Automatic conversion of each run of data-taking was performed, and hitmaps showing the summed hits across all events in the run produced to examine any unusually behaviour, either in individual pixels or across whole chips or layers. In so doing, a crescent-shaped region with a systematically small number of hits across all events was discovered. This region was examined using hitmaps of data runs taken at significant angles to the beam, and differing positions of the beam on the detector face, and it was found that the deficiency was not a result of unusual beam shape nor any readout/threshold inefficiency in the ALPIDEs, but more likely an inefficiency in the scintillator modules used for the triggering resulting in a smaller number of events for particles incident inside the region. It was shown that the N_{Hits} distribution of events incident inside the feature region does not differ significantly from that of events outside the feature region.

The Multi-Cut and Jet-Based event selection algorithms were developed in order to select only single-particle events which are incident within a central region of the detector for use in analysis. It was shown that the Multi-Cut algorithm retains $\approx 80\%$ of events in the primary peak of the N_{Hits} distribution, but that a small number of multi-particle events are not screened by this event selection. The Jet-Based event selection performs far better at screening out multi-particle events, but retains only $\approx 20\%$ of the primary peak.

Several calibrating corrections were made to selected events. Hot and dead pixels were removed by the application of a pixel mask, which was derived by pedestal runs recorded in the absence of an incident electron beam. Non-uniformity of the threshold between chips was corrected by a chip correction factor, which was applied to N_{Hits} and N_{Clus} distributions. An alignment procedure was derived from cosmic muon events to account for errors in the mechanical construction of the EPICAL-2 prototype.

The overall performance of EPICAL-2 was characterised. Small non-linearities in the data which were not corroborated in Allpix² simulations of like events were found, which were exacerbated by the application of the DBSCAN clustering algorithm. The likely cause of these non-linearities was found to be differences between the beam momentum requested and the actual momentum of beam particles. The longitudinal profiles of events from both data and simulations was analysed, and significant differences in the depth of the shower maximum were found. Small differences were found between the maxima for hits and clusters, suggesting that some cluster-merging was occurring. The resolution using both hits and clusters was computed for both data and simulations. The resolution using clusters was found to be universally better than that using hits, indicating that the clustering algorithm performs the function of reducing the variation of response to throughgoing shower particles. The resolution using simulations was better than that derived from data. This is to be expected since many sources of uncertainty which affect the data, such as the forced removal of hot/dead pixels and corrections of variations in the chip threshold, do not apply to the simulations. The resolution parameterisations are summarised in Table 6.11.

The lateral profile of EPICAL-2 for 5 GeV events was examined. Several algorithms for determining the shower axis were compared using radial distributions of the number of hits to each shower axis, and the ‘Perpendicular’ method found to give the best performance, particularly for earlier layers which best characterised the direction of travel of the beam particle. The hit density of radial annuli centred upon the shower axis was computed using the area of each annulus, with a geometric

calculation used to remove the dead area between chips in each layer. Excellent agreement between data and simulations was found. The maximum hit density was found to be ≈ 300 hits/mm², well below the hit density expected for saturation of to have a significant effect at the hit-level.

Differences in the response when reversing the direction of the beam were characterised, and qualitative similarities between the forward-backward asymmetry of cluster sizes found in both data and simulations. The asymmetry was found to be most significant for early layers of the prototype, suggesting an impact upon the response from the leptonic component of the shower. Detailed simulations of a single EPICAL-2 layer, with progressively simpler and more symmetrical geometry implementations provided two sources of the asymmetry: The additional gap between tungsten and silicon forward-going allowed for greater dispersion of the shower and so mitigated overlapping clusters, and the chip and flex cables screened out soft leptons back-scattered from the tungsten during backward running.

CONCLUSION

With the discovery of the Higgs boson, there is a significant and increasing need to consider the successor to the LHC. Irrespective of whether this is a linear lepton collider such as ILC or CLIC, or a yet-larger circular collider such as FCC, the relative merits of detector technologies should be considered and optimised for each collider application. In this thesis we have presented the digital calorimetry option for use as the ECAL component of future collider detectors. Digital calorimetry offers several advantages over its competitors. Mitigating the Landau fluctuations in the energy deposited in each layer of a DECAL should provide a significant improvement in the energy resolution. The ultra-high granularity of pixels in a DECAL provides excellent position resolution $\mathcal{O}(30 \mu\text{m})$, which makes it extremely well-suited for use in a PFA. Additionally, the ready availability of the CMOS MAPS sensors in industry makes DECALs easy and relatively cheap to make.

The performance of both a silicon-based AECAL and a DECAL in the FCC-hh context was examined. An ILD-like octagonal geometry was implemented in FCCSW 0.9,

with both analogue and digital silicon layers so that the same events could be used for analysis of both options. Single-electron events were simulated at a range of energies between 10 GeV and 1000 GeV. Four configurations were used: passive material between tungsten and lead, and varying the sampling fraction. The optimal configuration was found to use lead absorber with 50 sampling layers, which provided an energy resolution in the AECAL of:

$$\frac{\sigma_E}{E} = \frac{16.2\%}{\sqrt{E}} \oplus 0.4\% \quad (7.1)$$

While the energy resolution of the DECAL was found to be:

$$\frac{\sigma_E}{E} = \frac{15.5\%}{\sqrt{E}} \oplus 0.9\% \quad (7.2)$$

Saturation was found to be prohibitive of the DECAL performance at energies larger than ≈ 300 GeV.

The EPICAL-2 prototype is introduced as a novel 24-layer DECAL prototype, with 48 ALPIDE digital sensors sandwiched with 3 mm blocks of tungsten. The performance of EPICAL-2 was tested using an electron beam at the DESY II test beam facility, with the beam energy varying between 1 GeV and 5.8 GeV. Simulations of EPICAL-2 were performed using Allpix².

A well-contained sample of single electron events is required to characterise the EPICAL-2 performance and two selections are investigated. A series of sequential cuts are developed, which have a high efficiency for single particles, with a small residual contamination from two-particle events. This is complemented by a selection based on a Jet-finder algorithm, which is significantly lower contamination but a correspondingly lower efficiency.

The overall performance of EPICAL-2 was analysed using several metrics: the linearity, longitudinal profile and resolution. Small non-linearities were found to be present in data, particularly when a clustering algorithm was applied to mitigate fluctuations in the number of hits per particle, which are likely to be caused by

uncertainties in the true beam momentum. Small differences between the depth of the shower maximum were found between simulations and data in the longitudinal profiles. The resolution of EPICAL-2 was parameterised using hits and clusters, and was found to be significantly better for clusters, validating the use of the clustering algorithm. For data, the resolution using clusters was found to be:

$$\frac{\sigma_E}{E} = \frac{18.7\%}{\sqrt{E}} \oplus 2.4\% \quad (7.3)$$

which is comparable to the resolution of the Calorimeter for the Linear Collider with Electrons (CALICE) AECAL prototype. For simulations, the resolution was found to be significantly better:

$$\frac{\sigma_E}{E} = \frac{14.0\%}{\sqrt{E}} \oplus 2.6\% \quad (7.4)$$

which may be due to the absence of calibration imperfections in simulated data.

The lateral profiles for 5 GeV events in both data and simulations of EPICAL-2 were examined. Generally excellent agreement between data and simulations was found, with small disagreements between data and simulations present in the longitudinal profiles of narrow annular regions around the shower axis. The maximum hit density was found to be ≈ 300 hits/mm², significantly lower than the hit density at which complete saturation would occur.

The asymmetry between the average cluster size of beam-forward and beam-backward runs was analysed. Significant differences in the mean cluster size for upstream layers of the detector was found, which suggested an effect affecting the response of the leptonic shower component. The reliable description of data by simulation allowed a detailed model of the response of a single EPICAL-2 layer to reveal the origin of this asymmetry. It was found that the gap between silicon layers and the upstream block of tungsten causes a greater angular dispersion of leptons across the silicon, which reduces the overlapping of clusters from several leptons. Additionally, for the beam-backward runs the chip and flex cables screened out soft leptons which were back-scattered from the downstream tungsten.

REFERENCES

- [1] Y. Ne'eman, *The strongest force*, CERN Courier **9** (1969) 69.
- [2] E. Fermi, *An attempt of a theory of beta radiation. 1.*, Z. Phys. **88** (1934) 161.
- [3] E. Fermi, *Quantum Theory of Radiation*, Rev. Mod. Phys. **4** (1932) 87.
- [4] P. D. Group *et al.*, *Review of Particle Physics*, Progress of Theoretical and Experimental Physics **2020** (2020) , 083C01.
- [5] K. G. Wilson, *Confinement of Quarks*, Phys. Rev. D **10** (1974) 2445.
- [6] M. Gell-Mann, *Symmetries of Baryons and Mesons*, Phys. Rev. **125** (1962) 1067.
- [7] E. Noether, *Invariant Variation Problems*, Gott. Nachr. **1918** (1918) 235.
- [8] A. Proca, *Sur la théorie ondulatoire des électrons positifs et négatifs*, J. Phys. Radium **7** (1936) 347.
- [9] P. W. Higgs, *Broken Symmetries and the Masses of Gauge Bosons*, Phys. Rev. Lett. **13** (1964) 508.
- [10] G. Aad *et al.*, *Observation of a new particle in the search for the standard model higgs boson with the atlas detector at the lhc*, Physics Letters B **716** (2012) 1.
- [11] S. Chatrchyan *et al.*, *Observation of a new boson at a mass of 125 GeV with the CMS experiment at the LHC*, Physics Letters B **716** (2012) 30.
- [12] V. Khachatryan *et al.*, *Precise determination of the mass of the Higgs boson and tests of compatibility of its couplings with the standard model predictions using proton collisions at 7 and 8 TeV*, The European Physical Journal C **75** (2015) .

-
- [13] G. Aad *et al.*, *Measurements of the Higgs boson production and decay rates and coupling strengths using pp collision data at $\sqrt{s} = 7$ and 8 TeV in the ATLAS experiment*, The European Physical Journal C **76** (2016) .
- [14] G. Aad *et al.*, *Measurements of the Higgs boson production and decay rates and constraints on its couplings from a combined ATLAS and CMS analysis of the LHC pp collision data at $\sqrt{s} = 7$ and 8 TeV*, Journal of High Energy Physics **2016** (2016) .
- [15] V. Trimble, *Existence and nature of dark matter in the universe*, Annual Review of Astronomy and Astrophysics **25** (1987) 425.
- [16] T. Gershon and V. V. Gligorov, *CP violation in the B system*, Reports on Progress in Physics **80** (2017) 046201.
- [17] A. D. Sakharov, *Violation of CP Invariance, C asymmetry, and baryon asymmetry of the universe*, Pisma Zh. Eksp. Teor. Fiz. **5** (1967) 32.
- [18] K. Fujii *et al.*, *Physics Case for the International Linear Collider*, arXiv:1506.05992.
- [19] A. Blondel *et al.*, *Report of the ICFA Beam Dynamics Workshop 'Accelerators for a Higgs Factory: Linear vs. Circular' (HF2012)* , CERN, Geneva, 2013.
- [20] A. W. Chao, K. H. Mess, M. Tigner, and F. Zimmermann, eds., *Handbook of accelerator physics and engineering*, World Scientific, Hackensack, USA, 2013.
- [21] L. Linssen (editor), A. Miyamoto, M. Stanitzki, and H. Weerts, *Physics and Detectors at CLIC: CLIC Conceptual Design Report*, arXiv:1202.5940arXiv:1202.5940.
- [22] T. Behnke (editor) *et al.*, *The International Linear Collider Technical Design Report - Volume 1: Executive Summary*, arXiv:1306.6327.
- [23] CLIC and CLICdp Collaborations, M. J. Boland (editor) *et al.*, *Updated baseline for a staged Compact Linear Collider*, arXiv:1608.07537.
- [24] P. Lebrun *et al.*, *The CLIC programme: Towards a staged e+e- linear collider exploring the terascale: CLIC conceptual design report*, , Comments: 84 pages, published as CERN Yellow Report <https://cdsweb.cern.ch/record/1475225>.
- [25] A. Robson *et al.*, *The Compact Linear e⁺e⁻ Collider (CLIC): Accelerator and Detector*, arXiv:1812.07987.
- [26] CLICdp and CLIC Collaborations, T. K. Charles *et al.*, *The Compact Linear Collider (CLIC) - 2018 Summary Report*, arXiv:1812.06018.
- [27] *The International Linear Collider Technical Design Report - Volume 3.II: Accelerator Baseline Design*, arXiv:1306.6328.

- [28] A. Abada, M. Abbrescia, S. S. AbdusSalam *et al.*, *FCC-ee: The Lepton Collider.*, Eur. Phys. J. Spec. Top. **228** (2019) 261.
- [29] A. Blondel and P. Janot, *FCC-ee overview: new opportunities create new challenges.*, Eur. Phys. J. Spec. Top. **137** (2022) 92.
- [30] A. Abada, M. Abbrescia, S. S. AbdusSalam *et al.*, *FCC-hh: The Hadron Collider.*, Eur. Phys. J. Spec. Top. **228** (2019) 755.
- [31] *The International Linear Collider Technical Design Report - Volume 2: Physics*, arXiv:1306.6352.
- [32] M. Martinez and R. Miquel, *Multi-parameter fits to the $t\bar{t}$ observables at a future ee linear collider*, The European Physical Journal C - Particles and Fields **27** (2003) 49.
- [33] D. M. Asner *et al.*, *ILC Higgs White Paper*, in *Proceedings, 2013 Community Summer Study on the Future of U.S. Particle Physics: Snowmass on the Mississippi (CSS2013): Minneapolis, MN, USA, July 29-August 6, 2013*, 2013, arXiv:1310.0763.
- [34] ILD Collaboration, J. Tian and K. Fujii, *Measurement of Higgs couplings and self-coupling at the ILC*, PoS **EPS-HEP2013** (2013) 316.
- [35] E. P. F. de LAUSANNE, *Future circular collider working group*, 2018. <https://wiki.epfl.ch/fcc-epfl-lpap>.
- [36] FCC Collaboration, A. Abada *et al.*, *FCC-hh: The Hadron Collider: Future Circular Collider Conceptual Design Report Volume 3*, Eur. Phys. J. ST **228** (2019) 755.
- [37] T. Golling *et al.*, *Physics at a 100 TeV pp collider: beyond the Standard Model phenomena*, arXiv:1606.00947arXiv:1606.00947.
- [38] ATLAS Collaboration, L. Jeanty, *Expectations for sensitivity to BSM physics at the HL-LHC*, , (2019), <https://cds.cern.ch/record/2669586>.
- [39] M. Mangano (editor), *Physics at the FCC-hh, a 100 TeV pp collider*, arXiv:1710.06353arXiv:1710.06353.
- [40] FCC Design Study Group, P. Janot, *Precision measurements of the top quark couplings at the FCC*, PoS **EPS-HEP2015** (2015) 333, arXiv:1510.09056.
- [41] R. Contino *et al.*, *Physics at a 100 TeV pp collider: Higgs and EW symmetry breaking studies*, arXiv:1606.09408arXiv:1606.09408.
- [42] E. Garutti, *The physics of particle detectors: Vertex and tracking detectors, position and momentum measurement*, 2012. www.desy.de/~garutti/LECTURES/ParticleDetectorSS12/L9_Tracking.pdf.

-
- [43] D. Barney, *Calorimetry in Particle Physics, and the CMS High-Granularity Calorimeter*, Journal of Instrumentation **15** (2020) C07018.
- [44] C. W. Fabjan and F. Gianotti, *Calorimetry for Particle Physics*, Rev. Mod. Phys. **75** (2003) 1243.
- [45] R. Wigmans, *Calorimetry : energy measurement in particle physics*, Clarendon Press, Oxford, 2017.
- [46] M. Livan and R. Wigmans, *Misconceptions about Calorimetry*, Instruments **1** (2017) 3.
- [47] N. Watson *et al.*, *A MAPS-based readout of an electromagnetic calorimeter for the ILC*, J. Phys. Conf. Ser. **110** (2008) 092035.
- [48] T. Price, *Digital calorimetry for future $e^+ e^-$ linear colliders and their impact on the precision measurement of the top Higgs Yukawa coupling*, Ph.D. Thesis, 2013.
- [49] F. Hartmann, *Evolution of Silicon Sensor Technology in Particle Physics*, vol. 275 of *Springer Tracts in Modern Physics*, Springer, 2017.
- [50] SPiDeR, R. Coath *et al.*, *Advanced pixel architectures for scientific image sensors*, in *Topical Workshop on Electronics for Particle Physics*, 2009.
- [51] J. A. Ballin *et al.*, *Monolithic Active Pixel Sensors (MAPS) in a Quadruple Well Technology for Nearly 100% Fill Factor and Full CMOS Pixels*, Sensors **8** (2008) 5336.
- [52] H. Abramowicz (editor) *et al.*, *The International Linear Collider Technical Design Report - Volume 4: Detectors*, arXiv:1306.6329.
- [53] I. Irles and R. Poeschl, *Status of the technological prototype of the CALICE highly granular silicon tungsten calorimeter*, 2021. "Presented at LCWS2021, <https://indico.cern.ch/event/995633/contributions/4261854/>".
- [54] N. Alipour Tehrani *et al.*, *CLICdet: The post-CDR CLIC detector model*, .
- [55] CLICdp, D. Arominski *et al.*, *A detector for CLIC: main parameters and performance*, arXiv:1812.07337.
- [56] E. Sicking and R. Ström, *From precision physics to the energy frontier with the Compact Linear Collider*, Nature Physics **16** (2020) 386.
- [57] M. Aleksa *et al.*, *Calorimeters for the FCC-hh*, arXiv:1912.09962.
- [58] J. Cervantes *et al.*, *A software framework for FCC studies: status and plans*, EPJ Web Conf. **245** (2020) 05018.
- [59] M. Frank, F. Gaede, C. Grefe, and P. Mato, *DD4hep: A detector description toolkit for high energy physics experiments*, Journal of Physics: Conference Series **513** (2014) 022010.

- [60] S. Agostinelli *et al.*, *Geant4—a simulation toolkit*, Nuclear Instruments and Methods in Physics Research Section A: Accelerators, Spectrometers, Detectors and Associated Equipment **506** (2003) 250.
- [61] M. Mentink *et al.*, *Design of 4 Tm Forward Dipoles for the FCC-hh Detector Magnet System*, IEEE Transactions on Applied Superconductivity **27** (2017) 1.
- [62] A. Winter, *Prospects for Higgs boson & top quark measurements and applications of digital calorimetry at future linear colliders*, Ph.D. Thesis, 2018.
- [63] G. Aglieri Rinella, *“The ALPIDE pixel sensor chip for the upgrade of the ALICE Inner Tracking System”*, Nucl. Instrum. Methods Phys. Res. , Sect. A **845** (2017) 583.
- [64] M. Šuljić, *ALPIDE: the Monolithic Active Pixel Sensor for the ALICE ITS upgrade*, Journal of Instrumentation **11** (2016) C11025.
- [65] M. Mager, *ALPIDE, the Monolithic Active Pixel Sensor for the ALICE ITS upgrade*, Nucl. Instrum. Methods Phys. Res. , Sect. A **824** (2016) 434.
- [66] T. Price, *MAPS Technology for Vertexing, Tracking, and Calorimetry*, Physics Procedia **37** (2012) 932, Proceedings of the 2nd International Conference on Technology and Instrumentation in Particle Physics (TIPP 2011).
- [67] A. P. de Haas *et al.*, *The FoCal prototype—an extremely fine-grained electromagnetic calorimeter using CMOS pixel sensors*, Journal of Instrumentation **13** (2018) P01014.
- [68] M. Gabriel *et al.*, *A time resolved study of injection backgrounds during the first commissioning phase of SuperKEKB*, Eur. Phys. J. C **81** (2021) 972.
- [69] S. Spannagel *et al.*, *Allpix2: A modular simulation framework for silicon detectors*, Nuclear Instruments and Methods in Physics Research Section A: Accelerators, Spectrometers, Detectors and Associated Equipment **901** (2018) 164.
- [70] T. Rogoschinski, *EPICAL-2 simulation utilizing Allpix2*, EPICAL-2 Analysis Meeting, 2020. <https://indico.cern.ch/event/981109/>.
- [71] R. Brun and F. Rademakers, *ROOT: An object oriented data analysis framework*, Nucl. Instrum. Meth. A **389** (1997) 81.
- [72] R. Diener *et al.*, *The DESY II test beam facility*, Nuclear Instruments and Methods in Physics Research Section A: Accelerators, Spectrometers, Detectors and Associated Equipment **922** (2019) 265.
- [73] ILCSOft, *CED*, GitHub (2022), <https://github.com/iLCSOft/CED>.
- [74] F. Gaede, *Marlin and LCCD: Software tools for the ILC*, Nucl. Instrum. Meth. A **559** (2006) 177.

-
- [75] F. Gaede, T. Behnke, N. Graf, and T. Johnson, *LCIO: A Persistency framework for linear collider simulation studies*, eConf **C0303241** (2003) TUKT001, [arXiv:physics/0306114](https://arxiv.org/abs/physics/0306114).
- [76] F. Simon, *Status of CLAWS for BEAST*, Workshop Presentation, 2015. Presented at the 19th International Workshop on DEPFET Detectors and Applications.
- [77] F. Pliquett, *Pixel Mask Comparison*, EPICAL-2 Analysis Meeting, 2020. <https://indico.cern.ch/event/970154/>.
- [78] J. Alme *et al.*, *Performance of the electromagnetic pixel calorimeter prototype epical-2*, 2022. Submitted to JINST, doi: 10.48550/ARXIV.2209.02511.
- [79] M. Ester *et al.*, *A density-based algorithm for discovering clusters in large spatial databases with noise*, in *Proceedings of the Second International Conference on Knowledge Discovery and Data Mining (KDD-96)*, 1996.
- [80] H. Yokoyama, *EPICAL-2 DESY TB pileup event identification*, EPICAL-2 Analysis Meeting, 2020. <https://indico.cern.ch/event/970155/>.
- [81] M. Cacciari, G. P. Salam, and G. Soyez, *The anti- k_t jet clustering algorithm*, *Journal of High Energy Physics* **2008** (2008) 063.
- [82] M. Stanitzki, 2022. Private communication.
- [83] C. Adloff *et al.*, *Response of the CALICE Si-W electromagnetic calorimeter physics prototype to electrons*, *Nuclear Instruments and Methods in Physics Research Section A: Accelerators, Spectrometers, Detectors and Associated Equipment* **608** (2009) 372.
- [84] C. Zhang, *Measurements with a high-granularity digital electromagnetic calorimeter*, 2017. Ph.D. Thesis.